UNIVERSITY OF SOUTHAMPTON

Linear and Nonlinear Optical Processes in GaAs Semiconductor Microcavities

by

Maria Maragkou

A thesis submitted in partial fulfillment for the
degree of Doctor of Philosophy

in the
Faculty of Engineering, Science and Mathematics
School of Physics and Astronomy

October 22, 2010

UNIVERSITY OF SOUTHAMPTON

Abstract

Faculty of Engineering, Science and Mathematics
School of Physics and Astronomy

Doctor of Philosophy

by Maria Maragkou

In this thesis, polariton dynamics in GaAs semiconductor microcavities are investigated. Insertion of layers of active material within a Fabry-Perot resonator leads to strong coupling between excitons and photons, giving rise to new eigenmodes called exciton-polaritons.

Bose-Einstein condensation, the ability for massive occupation of a quantum state is considered a fascinating property of polaritons, due to their bosonic character. A full study of polariton condensation in 2D and 0D microcavities is included in this thesis. Formation of a ground state condensation in a planar cavity is resolved by studying the spatial, angular, coherence, energy and transient dynamics of polariton photoluminescence, as well as the transition from the weak- to the strong-coupling regime in the time-domain. The role of longitudinal optical phonons in the relaxation dynamics is also investigated. Encouraging experimental results confirm the efficiency of this mechanism towards the formation of a ground state condensate.

Polariton condensation in 0D GaAs quantum well microcavities is facilitated by etching the 2D semiconductor microcavity sample into pillars, removing the wavevector conservation. The spontaneous formation of a condensate in ground and non-ground states in 0D microcavities is investigated experimentally. A complete kinematic model that satisfactorily describes the spectral and temporal behaviour of polaritons in 0D structures completes this study.

Finally, the observation of the all optical spin Hall effect, the separation of spin polarised carriers in real and momentum space, in a pure photonic cavity is included in this thesis. Experimental findings suggest that the excitonic contribution in similar observations in the strong coupling regime with polaritons acting as spin carriers, is not essential for the observation of the anisotropic polarisation flux.

Στους γονείς μου,

που μ΄ αγαπούν περισσότερο από όσο πρέπει

Στη Συμώνη

Contents

Abstract i

List of Figures vi

Declaration of Authorship xii

Publications xiii

Acknowledgements xiv

Abbreviations xv

1 Introduction 1
1.1 Outline . . . 3

2 Fundamentals of polaritons 5
2.1 Optical properties of semiconductors . . . 5
2.1.1 Band structures in semiconductors . . . 5
2.1.2 Excitons . . . 7
2.1.3 Effects of confinement . . . 9
2.2 Cavities: light confinement . . . 11
2.2.1 Dispersion of intra cavity photons . . . 13
2.3 Light matter interaction . . . 14
2.3.1 Strong coupling regime: Polaritons . . . 14
2.3.1.1 Principles . . . 15
2.3.2 Weak coupling regime . . . 17
2.4 Relaxation mechanisms in microcavities . . . 17
2.4.1 Phonons . . . 19
2.4.1.1 Optical phonons . . . 20
2.4.1.2 Acoustic phonons . . . 21
2.4.2 Exciton-exciton scattering . . . 21
2.4.3 Pair polariton scattering . . . 22
2.5 Spin properties of polaritons . . . 22
2.5.1 Pseudospin formalism . . . 23
2.6 Summary . . . 24

3 Polaritons as bosons **25**
3.1 Bose-Einstein condensation . . . 25
3.1.1 BEC of an ideal Bose gas . . . 26
3.1.2 Bogoliubov theory of BEC . . . 28
3.1.3 Condensation in 2D systems . . . 30
3.2 Polariton condensation . . . 31
3.2.1 Critical densities of 2D polaritons . . . 33
3.3 Polariton laser . . . 33
3.4 Summary . . . 36

4 Samples **38**
4.1 Sample 1 - bare photonic cavity . . . 38
4.2 Sample 2 - planar GaAs microcavity . . . 39
4.3 Sample 3 - etched to micropillars . . . 42

5 All optical spin Hall effect **44**
5.1 TE–TM splitting . . . 45
5.2 Process . . . 47
5.3 Experimental Procedure . . . 49
5.3.1 Oblique incidence illumination . . . 49
5.3.2 Normal incidence illumination . . . 51
5.4 Theoretical modeling . . . 55
5.5 Discussion . . . 56
5.6 Conclusions . . . 58

6 Polariton condensation in a planar microcavity **59**
6.1 Setup . . . 61
6.2 Experimental Results . . . 61
6.3 Transition from weak to strong coupling regime . . . 64
6.4 Coherence . . . 70
6.5 Emission from k=0 . . . 71
6.6 Role of the spotsize regarding the condensation . . . 74
6.6.1 Setup . . . 74
6.6.2 Experimental Results . . . 74
6.6.2.1 Large excitation spot . . . 74
6.6.2.2 Small excitation spot . . . 76
6.6.3 Theory . . . 77
6.6.4 A simplified explanation . . . 80
6.7 Conclusions . . . 82

7 Investigating the role of LO phonons in the generation of a ground state polariton condensate **83**
7.1 Experiment . . . 85
7.1.1 Blueshift . . . 88
7.2 Theoretical explanation . . . 91
7.3 Comparison with non-resonant excitation . . . 93
7.4 Conclusions . . . 94

8 Polariton condensation in 0D microcavities **95**
8.1 Zero dimensional polaritons . . . 96
8.1.1 Experimental setup . . . 97
8.1.2 PL measurements . . . 98
8.1.3 Polariton Condensation in Micropillars . . . 101
8.1.4 Blueshift . . . 102
8.2 Non ground state polariton condensation . . . 102
8.2.1 Overview . . . 102
8.2.2 Experimental Data . . . 103
8.2.3 A simple kinematic model . . . 105
8.3 Polarisation related findings . . . 109
8.4 Theoretical discussions . . . 112
8.4.1 Spontaneous scattering regime dynamics . . . 114
8.4.2 Stimulated scattering regime dynamics . . . 116
8.4.3 Discussion . . . 117
8.5 Conclusions . . . 119

9 Conclusions **121**
9.1 Future work . . . 122

A Time-dependent perturbation theory and Fermi's golden rule **124**

B Transfer Matrix Method **127**

C Programming codes in Igor Pro **130**
C.1 Transfer matrix method . . . 130
C.2 Rate equations . . . 133

Bibliography **137**

List of Figures

2.1 The primitive cell of GaAs. . . . 6
2.2 Energy-band structure of GaAs, where E_g is the energy bandgap. Plus-signs (+) indicate holes in the valence bands and minus signs (-) indicate electrons in the conduction bands. . . . 7
2.3 A pair excitation in the scheme of valence and conduction band (a) in the exciton picture for (b) a direct gap semiconductor. . . . 8
2.4 Discrete energy levels in a quantum well. . . . 10
2.5 Band structures for III-V semiconductors in (a) bulk and (b) QW. . . . 10
2.6 Energy density of states $g(E) = dN/dE$ in 3D, 2D, 1D and 0D structures, where dN is the number of electron quantum states within the energy interval dE. . . . 11
2.7 Reflectivity spectrum of a DBR, calculated via the transfer matrix technique. 12
2.8 Reflectivity spectrum of a cavity, calculated via the transfer matrix technique. . . . 13
2.9 Dispersion of intra-cavity photons, as a result of confinement. . . . 14
2.10 Calculated anticrossing of the lower (LP) and upper (UP) polariton energy levels while tuning the cavity energy (E_{CAV}) across the exciton resonance (E_X). . . . 16
2.11 (a-c) Polariton dispesions and corresponding Hopfield coefficients for (a) positive (b) zero and (c) negative detuning between the cavity and the exciton mode. (d-f) correspond to the corresponding LP Hopfield coefficients. 18
2.12 Measured phonon spectra in GaAs. TO and LO correspond to transverse and longitudinal optical modes, and TA and LA to transverse and longitudinal acoustic modes 20
2.13 Polarization of optical transitions in zincblende semiconductor quantum wells. Red, blue and green lines show σ^+ , σ^- and linearly polarized transitions, respectively. . . . 23
2.14 The pseudospin vector represents the polariton polarization and lies on the surface of the Poincare sphere for a pure polarized state. . . . 24

3.1 Vertical and horizontal dashed lines show the limits of the strong-coupling regime imposed by the exciton thermal broadening and screening, respectively. Solid lines show the critical concentration N_c versus temperature of the polariton KT phase transition. Dotted and dashed lines show the critical concentration N_c for quasicondensation in 100 μm and in one meter lateral size systems, respectively. The thin dashed line (upper right) symbolizes the limit between vertical-cavity surface-emitting laser (VCSEL) and light-emitting diode regimes. . . . 34

3.2 Dispersion of polariton-laser, showing pair scattering of polaritons at k_1, k_2 acting as a reservoir for the polariton trap at k=0. 35

4.1 Calculated low temperature reflectivity spectrum for Sample 1. 39
4.2 Schematic of the sample design, including the refractive index changes between the layers as well as the electric field inside the cavity. The quantum wells coincide with the centre and two side antinodes of the electromagnetic field. 40
4.3 Energy dispersions of the cavity (red), light- and heavy- hole excitons (green), and the three polariton modes (lower, middle and upper in black) versus wavevector $k_{||}$ for samples 2 and 3. 41
4.4 Energy dispersions of the three polariton modes *vs.* position on the sample for Sample 2. 41
4.5 Reflectivity spectrum of Sample 3. 42
4.6 (a) Scanning electron micrograph showing a micropillar array. (b) Photoluminescence spectrum of a 4 μm diameter micropillar. Discrete polariton modes are clearly resolved. The wide band feature is attributed to uncoupled exciton emission. 43

5.1 Propagation of TE and TM polarized light between two media of different refractive indices n_1 and n_2. 46
5.2 TE–TM splitting dependence of the bare photonic cavity with increasing angle. The range of angles that was investigated is shown. 46
5.3 The direction of the effective magnetic field (green arrows) is dependent on the direction of the in-plane wavevector k in momentum space. (a) The initially linear polarised pseudospin (black arrows) after the Rayleigh scattering act. (b) The initially linear polarised pseudospin (black arrows) rotates until it becomes σ^+ (blue arrows) or σ^- (red arrows) circularly polarised depending on the orientation of the effective magnetic field. The result is a separation of spin-up and spin-down polarized cavity photons in different quadrants of the elastic circle. 48
5.4 Calculated bare cavity mode dispersion vs angle. Filled circles correspond to experimental points. 49
5.5 Experimental setup where two separate paths allow collection of transmission in (a) momentum space and (b) real space. The incident beam is always linearly polarised and occurs at an oblique angle θ. 50
5.6 The (a) σ^+ and (b) σ^- detected component in momentum space upon oblique incidence illumination at 10°. 50
5.7 Observation of the all-optical spin Hall effect in reciprocal space under population of the elastic ring by Rayleigh scattering for angles of (a) 5° (b) 10° (c) 15° (d) 20°. 51
5.8 Experimental setup, where two separate paths allow collection of transmission in (a) momentum space and (b) real space. The incident beam is always linearly polarised and occurs at normal incidence. 52
5.9 (a) Total intensity in real space for illumination energy corresponding to 10°, where the illumination beam profile is superimposed. The σ^+ detected component is shown in (b). 52

5.10 Spin-polarised rings in momentum space (a-d) resolved with Stokes parameter, ρ_c and corresponding real-space (e-h). The colour scale is linear in intensity. The incident beam is TE polarised at energies corresponding to (a, e) 5° (b, f) 10° (c, g) 15° (d, h) 20°. 53
5.11 The measured degree of circular polarization under horizontal excitation in near (a) and far field (b). The resonant energy corresponds to an external angle of excitation of 12 degrees. The spin currents are inverted under vertical excitation in near (c) and far field (d). 53
5.12 Evolution of (a) $|\rho_C|$ and (b) the distance of the ballistic propagation of photons in real space as the wavevector increases. The solid line in (a) is a guide to the eye and in (b) corresponds to theoretical calculations. The markers correspond to experimental data. 54
5.13 Far- (a) and near- field (b) Stokes parameters calculated for TE polarised excitation at 1.48663eV equivalent to 15 degrees. Theoretical calculations for the same conditions are given in (c,d). 56

6.1 Experimental setup that allows for the collection of the Fourier plane and its imaging on a spectrometer, coupled with a streak camera. The sample is excited using pulsed excitation through a large aperture lens. 60
6.2 Time- and energy-resolved emission spectra for a -7 meV negative detuning in a planar GaAs microcavity for various indicated input powers. 62
6.3 Power dependence of (a) the intensity, (b) the energy blueshift and (c) linewidth of the ground state emission as a function of the excitation power for a -4meV negative detuning in a planar GaAs microcavity. (d) Rise (solid circles) and decay times (open squares) of the emission with increasing excitation power. 63
6.4 Time resolved emission from the k=0 state at a -4 meV detuning, (a) with and (b) without the use of the grating for spectral resolution. A direct comparison of the two profiles can be seen in (c). 65
6.5 Time and spectrally resolved photoluminescence spectrum and the corresponding linewidth for excitations powers (a, b) below threshold, (c, d) at the nonlinear strong coupling regime and (e, f) at the weak coupling regime. 66
6.6 Energy and time resolved emission from the $k = 0$ state at a detuning of -4 meV (top panel (0-240 ps after excitation)). Dispersion images at the bottom panel correspond to times indicated by the black vertical lines. The red solid lines correspond to calculated exciton, cavity and lower polariton dispersions when the cavity operates at the linear strong coupling regime, i.e. below threshold. The dashed line in (b) corresponds to the redshifted cavity mode. 67
6.7 Energy and time resolved emission from the $k = 0$ state at a detuning of -4 meV (top panel (200-760 ps after excitation)). Dispersion images at the bottom panel correspond to times indicated for the black vertical lines. The red solid lines correspond to calculated exciton, cavity and lower polariton dispersions when the cavity operates at the linear strong coupling regime, i.e. below threshold.The dashed line in (b) corresponds to the blueshifted LPB. 68
6.8 Michelson interferometer setup used for coherence measurememts. 70

6.9 Far field interferograms of the ground state photoluminescence at zero time delay (a) in the weak coupling and (b) nonlinear strong coupling regime. The dependence of interference contrast on time delay for the weak (black open triangles) and strong coupling (red solids circles) is shown in (c). . . 71
6.10 (a) Emission energy as a function of the detection angle for excitation powers (black open circles) below threshold, (black solid squares) at threshold and (red circles) at the weak coupling regime. The open red markers correspond to emission due to uncoupled excitons, observed at high angles. The black solid line correspond to the calculated lower polariton branch and the dashed black line to the heavy hole exciton and the cavity mode whereas the dashed red line to the cavity mode redshifted by 3 meV. (b) Polariton occupancy as a function of the detection angle. (Inset) Real space image at threshold and the corresponding intensity profile. 72
6.11 Experimental setup that allows for the collection of the Fourier plane and its imaging on a spectrometer. An arrangement of lenses allows for the spatial modulation of the excitation spotsize. 75
6.12 Lower polariton branch energy dispersions for -11 meV detuning conditions with a spotsize of 25 μm FWHM for pump powers (a-b) below, (c) at and (d) above threshold (P_{th}=15 mW). Doted white lines indicate the calculated dispersions for the LPB and the cavity mode. Power dependence of (e) the emission intensity and (f) the linewidth of the lower polariton ground state as a function of the excitation power. (g) Angular profile of the emission at 1.6 meV for $P = P_{th}$, corresponding to (c). (h) Near field polariton emission for $P = P_{th}$. 76
6.13 Lower polariton branch energy dispersions for -11 meV detuning conditions with a spotsize of 4 μm FWHM for pump powers (a-b) below, (c) at and (d) above threshold (P_{th}=75 mW). 77
6.14 Lower polariton branch energy dispersions for -11 meV detuning conditions with a spotsize of 0.8 μm FWHM for pump powers (a-b) below, (c) at and (d) above threshold (P_{th}=30 mW). 77
6.15 Lower polariton branch energy dispersions for -11 meV detuning conditions for various excitation spot sizes at $P = P_{th}$. 78
6.16 Energy of the polariton condensate at threshold *vs* the FWHM of the excitation spot size. The dashed line is a guide to the eye. 78
6.17 Near field polariton emission for $P = P_{th}$ for excitation spot sizes of (a) 0.8 μm, (b) 1.2 μm and (c) 4.1 μm. 79
6.18 The force $F = dE/dx$ calculated for the various spotsize intensity profiles, annoted in different colors. 81
6.19 Experimental data and theoretical calculations regarding the wavevector of the condensate with respect to the FWHM of the spotsize. 81

7.1 LO phonon assisted polariton scattering in a microcavity. When the microcavity is excited 36 meV above the $k = 0$ state of the LPB, polaritons with high wavevectors relax instantly to the lowest state of the branch, avoiding the bottleneck. 85
7.2 Energy dispersion of the cavity and exciton modes (dashed lines) and lower, middle and upper polariton (solid lines) as a function of detuning. The open markers correspond to experimental data and their size is proportional to the LO phonon scattering strength. 86

7.3 Experimental setup for the investigation of the role of LO phonons in polariton relaxation. The sample is excited non resonantly at an oblique angle and emission from $k = 0$ is collected and spectrally resolved. 86
7.4 Power dependence of (a) the emission intensity, (b) the energy blueshift and (c) linewidth of the lower polariton branch as a function of the excitation power for -4 meV detuning. 87
7.5 Power dependence of (a) the emission intensity, (b) the energy blueshift and (c) linewidth of the lower polariton branch as a function of the excitation power for -17meV detuning. 88
7.6 Energy dispersions of the cavity and heavy hole exciton (dust lines) and lower and upper polariton (solid lines) calculated theoretically. Emission spectra (red solid lines) above threshold, obtained under various different detuning conditions have been added. The black dots correspond to the emission energy below threshold while the red ones correspond to the blueshifted polariton emission just above it. (inset) Emission blueshift at threshold vs exciton fraction (red markers) and detuning (black markers). 89
7.7 Energy and time resolved emission from the $k = 0$ state at a detuning of -4 meV (top panel). Dispersion images at the bottom panel correspond to times indicated by the black vertical lines. The red solid lines correspond to calculated exciton, cavity and lower polariton dispersions when the cavity operates at the linear strong coupling regime, i.e. below threshold. . 90
7.8 Energy dispersion of the cavity and exciton modes (dust lines) and lower, middle and upper polariton (solid lines) as a function of angle. The solid ellipses indicate the energy of the middle polariton bottleneck. 91
7.9 Experimental data (markers) and theoretical fit (line) for the slope $S(\delta)$ below threshold for a range of detunings. 92
7.10 Experimental data (markers) and theoretical fit (line) for the stimulation threshold $T(\delta)$ for a range of detunings. 93

8.1 Energy spectrum of a number of photon modes confined in micropillars versus their size. 96
8.2 Experimental setup for the investigation of polariton dynamics in a 0D structure. The components within the box constitute an imaging microscope for 'navigation' over the sample. The waveplates in front of the CCD allow for the investigation of the polarisation properties of the sample. 97
8.3 Calculated reflectivity spectrum of the sample; the arrow indicates the energy of excitation. 98
8.4 Below threshold photoluminescence for a square pillar with (a) 2.4 μm side, (b) 3.2 μm side, (c) 5 μm side, (d) 6 μm side and (e) 10 μm side for zero detuning conditions. (f) Threshold power for polariton amplification vs side. 99
8.5 Below threshold photoluminescence for 3.2 μm side square pillar at (a) 2.5 meV, (b) 0 meV, (c) -6 meV and (d) -13 meV detuning. 99
8.6 At threshold photoluminescence for 3.2 μm side square pillar of various detunings 100
8.7 Power dependence of (a) the intensity, (b) the energy blueshift and (c) linewidth of the ground state emission as a function of the excitation power for a 5 μm side square pillar at zero detuning. 101

8.8 Power dependence of the energy emission of various polariton modes for (a) a 3.2 μm side square pillar negatively detuned at -13 meV and (b) a 5 μm side square pillar at zero detuning. 103
8.9 Power dependence of (a) the emission intensity and (b) the energy blueshift that occurs for a 3.2 μm square pillar at zero and -13 meV detuning. The hollow markers correspond to the higher energy mode that exhibits polariton amplification for a certain range of excitation powers.(c-h) Power dependence of photoluminescence from a 3.2 μm pillar at -13 meV detuning. 104
8.10 Below threshold photoluminescence spectrum from a 3.2 μm square pillar at δ=-13 meV detuning and schematic representation of the energy transitions between the exciton reservoir and polariton states M1, M2 and M5. Arrows indicate exciton-exciton and pair-polariton scattering between the states. 105
8.11 Comparison of the measured photoluminescence decay curves (solid lines) and the fit of the theoretical kinematic model (dotted line). Columns correspond to different polariton states (M1, M2, M5 from left to right) and rows to different excitation power (50 μW, 70 μW, 100 μW, 300 μW and 1000 μW from top to bottom). 107
8.12 Comparison of the measured polarization components and the overall polarization for a negatively detuned pillar (δ=-6 meV) of 3.2 μm side size. Columns correspond to different excitation powers (80 μW, 150 μW, 500 μW and 1000 μW from left to right) and rows to the different polarization components (ρ_L, ρ_D, ρ_C and ρ from top to bottom. 109
8.13 Time profiles of the polarization components of the emission above threshold from a negatively detuned pillar (δ=-6meV) of 3.2μm side size. Columns correspond to different excitation powers (350 μW, 500 μW, 700 μW and 1000 μW from left to right) and rows to the different polarization components (ρ_L, ρ_D, ρ_C and ρ from top to bottom). 110
8.14 Coherence times of the (a) the linear and (b) the diagonal component of the emission above threshold from a negatively detuned pillar (δ=-6 meV) of 3.2 μm side size vs. excitation powers. 111
8.15 Coherence time of the polarization p of the emission above threshold from a negatively detuned pillar (δ=-6 meV) of 3.2 μm side size vs. excitation powers. 111
8.16 Level scheme for the model proposed. Parametric exciton exciton scattering to LP and UP states is depicted by black arrows, phonon emission and exciton exciton scattering to exciton + LP state is gray. 114
8.17 Theoretical fits of the PL curves for (a) a 3.2 μm pillar, at zero detuning, (b) a 3.2 μm pillar, detuned at -6meV, (c) a 10 μm pillar, at zero detuning and (d) a 2.4 μm pillar, at zero detuning. 117
8.18 Dynamics of the visible modes of a 6 μm size pillar at zero detuning at various pump intensities. 118
8.19 Calculated PL spectra of a 6 μm size pillar at zero detuning, depending on the blueshift of exciton resonance due to exciton-exciton interactions. . 119

Declaration of Authorship

I, Maria Maragkou, declare that this thesis titled, 'Linear and Nonlinear Optical Processes in GaAs Semiconductor Microcavities' and the work presented in it are my own. I confirm that:

- This work was done wholly or mainly while in candidature for a research degree at this University.
- Where any part of this thesis has previously been submitted for a degree or any other qualification at this University or any other institution, this has been clearly stated.
- Where I have consulted the published work of others, this is always clearly attributed.
- Where I have quoted from the work of others, the source is always given. With the exception of such quotations, this thesis is entirely my own work.
- I have acknowledged all main sources of help.
- Where the thesis is based on work done by myself jointly with others, I have made clear exactly what was done by others and what I have contributed myself.

Signed: _____

Date: _____

Publications

- **The optical analogue of the spin Hall effect**
  M. Maragkou, C. E. Richards, T. Ostatnicky, A. J. D. Grundy, J. Zajak, W. Langbein and P. G. Lagoudakis, *under preparation*.

- **Stimulated emission of polaritons from a GaAs/AlAs semiconductor microcavity excited by non-resonant optical pulses**
  M. Maragkou, A. J. D. Grundy and P. G. Lagoudakis, *submitted*.

- **LO phonons polariton laser**
  M. Maragkou, A. J. D. Grundy, T. Ostatnicky and P. G. Lagoudakis, accepted in *Applied Physics Letters*.

- **Spontaneous nonground state polariton condensation in pillar microcavities**
  M. Maragkou, A. J. D. Grundy, E. Wertz, A. Lemaitre, I. Sagnes, P. Senellart, J. Bloch, and P. G. Lagoudakis, *Physical Review B* 81:081307(R), 2010

Acknowledgements

This PhD has been a very rich experience for me, with numerous people contributing to it, with ideas, guidance and support, in a professional and personal level.

First of all, I would like to thank my supervisor Prof. Pavlos Lagoudakis, for trusting me in the lab, and giving me the opportunity to learn all these new exciting physics. I appreciate his support, his endless energy and passion, and his patience with me, especially when things were not running so smoothly. I would also like to thank Prof. Richard Harley, for showing me what a true mentor is like as well as my second advisor, Prof. Peter deGroot.

Very special thanks goes to Alastair Grundy, for teaching me everything I know on treating polaritons in the lab, for putting up with my mediterranean temper and for being an excellent company in the lab for two years. I am grateful to Giorgio Baldassari for working with me during my early days in the lab and Caryl for the long hours she spent with me looking for rings. I would also like to thank our collaborators, Wolfgang Langbein, Esther Wertz and Jacqueline Bloch for provision of samples and stimulating discussions as well as Alexey Kavokin for always answering my sometimes silly questions. I am forever grateful to Tomáš Ostatnický, for always being eager to answer my questions and giving me enormous help by modeling our experiments. I also thank very much those who spared a few hours reading this thesis prior to its submission.

I would like to thank Mr. Colin, for providing the essential helium for our experiments, always with a smile. I also want to thank Tom, Justin, Gary and Gareth, for helping me out with all sorts of problems in the lab.

I am forever grateful to the hybrids that welcomed me to the group, Soontorn, Stefan and Peter, as well as the hybrids that joined the group after me, Chunyong, Dave, Peristera, Elena, Junis and Robin. Living in Southampton was much more fun thanks to them! I must also thank my brother, my housemates and all my friends around Europe; the old friends who didn't forget me and who I terribly miss, and the new ones, whom I was very lucky to meet! Above all, I thank my girls, Natalie, Sofia and Georgia for their love, support and eagerness to explore with me several corners of this world.

Finally, I would like to thank Peter for being my much better half these last years.

Abbreviations

BEC	**B**ose **E**instein **C**ondensation
CdTe	**Cd**mium **Te**lluride
$\mathbf{E}_{LH}$	**E**nergy **L**ight **H**ole Exciton
$\mathbf{E}_{LO}$	**E**nergy **L**ongitudinal **O**ptical Phonons
$\mathbf{E}_{LP}$	**E**nergy **L**ower **P**olariton
GaAs	**Ga**llium **As**enide
GaN	**Ga**llium **N**itride
LO	**L**ongitudinal **O**ptical Phonon
LA	**L**ongitudinal **A**coustical Phonon
LPB	**L**ower **P**olariton **B**ranch
UPB	**U**pper **P**olariton **B**ranch
$\mathbf{X}_{LH}$	**L**ight **H**ole E**x**citon
$\mathbf{X}_{HH}$	**H**eavy **H**ole E**x**citon

Chapter 1

Introduction

Advances in semiconductor physics and technology have evolved tremendously over the last 50 years. The first demonstration of the semiconductor laser [1] in 1962 defined the beginning of an era that changed almost every aspect of everyday life, from telecommunications to data storage.

New crystal growth technologies, such as molecular beam epitaxy (MBE) and metal-organic chemical vapour deposition (MOCVD) developed in the 70s, enabled precise and controlled stacking of thin layers of different semiconductor materials. In such ultra thin structures, carriers are quasi-confined in the growth direction, resulting in a much reduced number of electronic states and a much lower threshold current for quantum-well lasers. Indeed, in 1979 the first vertical cavity surface emitting laser (VCSEL) using Bragg reflectors to form the cavity was built [2].

Research over past decades focused either on matter confined in quantum wells, wires and dots [3, 4], or on the electromagnetic field confined in various types of cavities. Both research paths revealed interesting phenomena since confinement strongly modifies the properties of the initial system. The two fields were finally merged with the design of low-dimensional structures, consisting of a microresonator with quantum wells embedded at the antinodes of the resonant photon mode. Careful design of these structures increased the coupling of the photons and the excitons beyond their decay rate from the system and resulted in a strong coupling regime between light and matter [5]. The mixing of exciton and photon wave functions gave rise to new quasi particles called microcavity exciton-polaritons [6]. Their uniqueness lies in the combination of exciton and photon properties,

which grants them with very light effective masses, strong inter-particle interactions and an unexpected bosonic character.

Since their first observation, polaritons have been at the forefront of semiconductor research, particularly after Imamoglu *et al.* suggested the possibility for nonlinear effects such as lasing and condensation [7]. The initial skepticism of the community turned into enthusiasm when Savvidis *et al.*, in 2000, [8] demonstrated polariton parametric amplification via the stimulated scattering of polaritons using a two beam experimental setup, confirming their bosonic character. Research on microcavity polaritons has since been evolving around two major axes; the development of low threshold lasing devices and the investigation of basic exotic quantum phenomena such as Bose Einstein condensation (BEC), superfluidity and vortices. Theoretical work [7, 9, 10] in the framework of polariton laser paved the way for experimentalists. Unlike conventional lasers, spontaneous emission of coherent light is an intrinsic property of the polariton condensate. As they circumvent the need for population inversion, polariton condensates exhibit ultra low thresholds for operation, rendering the realisation of such a device the holy grail within the light-matter interaction community.

At the same time though, the realisation that polaritons behave as bosons in the low density regime, immediately established them as candidates for the observation of BEC [11, 12]. This phase transition enables a large population of particles to spontaneously occupy the same quantum state, leading to the formation of a long range phase coherence. Honoured with the Nobel prize in 2001 [13] for its observation in cold atom systems [14], BEC has yet to be achieved in the solid state. Despite various proposals [15, 16], efforts towards the observation of BEC in excitonic systems have so far been unfruitful. Polaritons however outweight excitons as they have even lighter effective mass, which should in principle allow for BEC even at room temperature.

Although the initial material of choice for the community was GaAs, failure to observe any of the above phenomena led to the development of structures from other materials or more sophisticated methods of confinement. The goal of these efforts was in overcoming the bottleneck effect that prevented the formation of the condensate at the lowest energy state [17–20]. Alternative materials with higher exciton binding energies, like CdTe [21] and GaN [22], and/or spatial localization proved quite successful. Observation of polariton condensation in nominally 2D microcavities was attributed to the spatial

localization of polaritons in the photonic disorder of the cavities [21, 23, 24] (Chapter 6). The localization required for condensation to occur was also controlled by engineering tunable potential traps [25, 26] or by etching planar microcavity samples into pillars [27–29] (Chapter 8).

Observation of BEC in microcavities allowed for the observation of other linked fascinating phenomena, such as the optical spin Hall effect [30], superfluidity [31, 32] and vortices [33, 34]. Although microcavities offer superb possibilities for investigating rich quantum physics, it is worth bearing in mind that their character is only the mixture of light and matter. Therefore, some of the effects attributed to polaritons, originate from either one of their two characters and can be realised within simpler systems (Chapter 5).

1.1 Outline

Chapter 2 contains an essential overview of the theory of the confinement of excitons and photons in semiconductor microcavities. The properties of the new quasiparticles that arise, as well as their main relaxation mechanisms are reviewed.

Chapter 3 contains the basic concepts behind Bose-Einstein condensation, focusing on the assumptions needed to describe polariton condensates within the same framework.

Chapter 4 gives the details of the three GaAs microcavity structures used for the experiments described in this thesis.

Chapter 5 investigates the generation of spin currents in real and momentum space in a bare photonic cavity. The purely photonic character of the system allows for a classical interpretation of the observed spin currents in contrast to previous observations in strongly coupled microcavities, modeled with the pseudospin model. These findings constitute the optical analogue of the spin Hall effect.

Chapter 6 investigates the temporal and spectral dynamics of a ground state polariton condensate, formed under non-resonant excitation, by studying the spatial, angular, coherence, energy and transient dynamics of polariton photoluminescence. For high excitation densities the transition from the weak- to the strong-coupling regime in the time-domain is resolved.

Chapter 7 studies the role of longitudinal optical (LO) phonons in the relaxation dynamics of polaritons towards the ground state and the formation of a condensate. Resonant excitation with the light hole exciton energy (E_{LH}) allows for the formation of a ground state condensate. Relaxation towards $k = 0$ is enhanced when the energy separation between the excitation energy and the LP is resonant with the LO phonon energy.

Chapter 8 investigates the temporal and spectral dynamics of polaritons in zero dimensional structures under non-resonant excitation, including observations such as spontaneous non-ground state polariton condensation. A universal model of relaxation mechanisms is introduced.

Chapter 9 summarises the main results of this thesis and suggests further experimental studies.

Chapter 2

Fundamentals of polaritons

Confinement effects on excitons and photons are reviewed. The combination of the two gives rise to the strong coupling regime and new mixed quasiparticles, called polaritons, the main subject of the research in this thesis.

2.1 Optical properties of semiconductors

2.1.1 Band structures in semiconductors

Crystals are defined by their well-structured periodic placement of atoms. A primitive cell with lattice constant a is the smallest assembly of atoms that, upon repetition, forms the entire crystal. Many important semiconductors, including most III-V compounds like Gallium Arsenide (GaAs), crystallize in the zincblende lattice structure, shown in Figure 2.1 [35]. Each atom is surrounded by four equidistant nearest neighbours which lie at the corners of a tetrahedron.

For any semiconductor there is a forbidden energy range in which states cannot exist, called the bandgap E_g. Energy bands are permitted above this energy gap, called the conduction bands while the ones below are named valence bands. In Figure 2.2 [36] the bottom of the conduction band is designated E_C, and the top of the valence band E_V.

The valence band in zincblende semiconductor materials, such as that for GaAs in Figure 2.2, consists of four subbands. Each band is doubled when spin is included in the Schrödinger equation. Three of the four bands are degenerate at $k = 0$, forming the

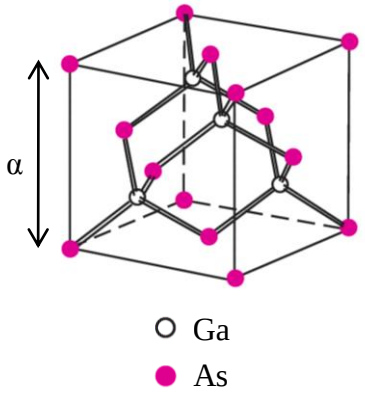

FIGURE 2.1: The primitive cell of GaAs [35].

upper edge of the band, and the fourth band forms the bottom. Near the band edges, i.e., bottom of E_C, and top of E_V, the $E-k$ relationship can be approximated by a quadratic equation

$$E(\boldsymbol{k}) = \frac{\hbar^2 k^2}{2m^*}, \tag{2.1}$$

where m^* is the associated effective mass. The two top valence bands are usually approximated by two parabolic bands with different curvatures: the heavy-hole band (the wider band in k-axis with smaller $\partial^2 E/\partial k^2$) and the light-hole band (the narrower band with larger $\partial^2 E/\partial k^2$). Carriers in motion are also characterized by a group velocity

$$v_g = \frac{1}{\hbar}\frac{dE}{dk} \tag{2.2}$$

with momentum

$$\boldsymbol{p} = \hbar \boldsymbol{k}. \tag{2.3}$$

When the minima of the conduction and maxima of the valence band occur for the same value of k one speaks of direct gap, otherwise the semiconductor is an indirect bandgap semiconductor. This bears significant consequences when carriers transfer between this minimum gap in that momentum (or k) is conserved for direct bandgap but changed for indirect bandgap.

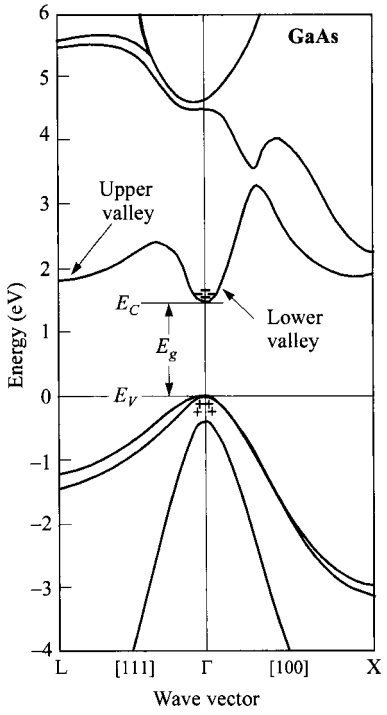

FIGURE 2.2: Energy-band structures of GaAs, where Eg is the energy bandgap. Plus-signs (+) indicate holes in the valence bands and minus signs (-) indicate electrons in the conduction bands [36].

2.1.2 Excitons

Apart from the transitions that occur for photon energies $E > E_g$, absorption peaks can be observed for energies lower than the gap, corresponding to the creation of an electron-hole pair bound by Coulomb interaction, called the exciton [37]. Using the effective mass approximation, excitons can be treated within the framework of a hydrogen like problem with a Coulomb potential term due to the Coulomb interaction between electron and hole (Figure 2.3). Separation between the relative motion of electron and hole and the motion of the center of mass, which is valid for direct gap semiconductors, leads to the dispersion relation of excitons (shown in Figure 2.3b), given by

$$E_X(n_B, \boldsymbol{K}) = E_g - R_y^* \frac{1}{n_B^2} + \frac{\hbar^2 \boldsymbol{K}^2}{2M}, \tag{2.4}$$

with $n_B = 1, 2, 3, ..$ the principal quantum number and $M = m_e + m_h$ and $\boldsymbol{K} = \boldsymbol{k}_e + \boldsymbol{k}_h$ are the translational mass and wave vector of the exciton. The exciton binding energy

is given by

$$R_y^* = 13.6\mu\text{eV}\frac{m'}{m_0}\frac{1}{\epsilon^2}, \tag{2.5}$$

where the effective Rydberg energy is modified by the reduced mass $m' = \frac{m_e m_h}{m_e+m_h}$ of the electron and hole and the dielectric constant of the medium ϵ. m_0 is the free electron mass. The exciton radius $\alpha_B^{ex} = \alpha_B^H \epsilon \frac{m'}{m_0}$ [38]. The excitonic Rydberg energy is usually much smaller than the bandgap and the Bohr radius is larger than the lattice constant. The latter implies that the 'orbits' of electron and hole around their common center of mass average over many unit cells which in turn justifies the effective mass approximation. These excitons are called Wannier excitons [39], in comparison to the much smaller Frenkel excitons [40], usually found in molecular structures.

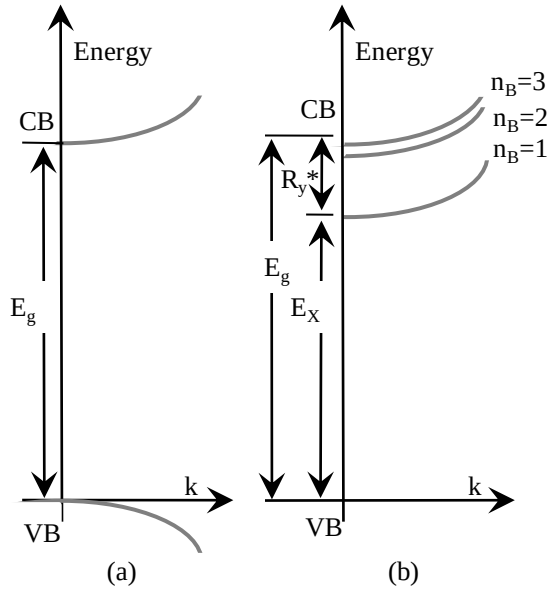

FIGURE 2.3: A pair excitation in the scheme of valence and conduction band (a) in the exciton picture for (b) a direct gap semiconductor.

Due to their small binding energy, excitons have difficulty surviving at room temperature. In GaAs for example, which is used extensively in the experiments of this thesis, the exciton radius $\alpha_B^{ex} \simeq 150\mathring{A}$ and the exciton energy is about 4.1 meV [41], which makes the formation of excitons at room temperatures quite challenging ($k_B T \simeq 25$ meV). The above dictates conduction of experiment on GaAs structures at liquid helium temperatures.

For low densities and low temperatures, the excitons in thermodynamic equilibrium can be well described by Boltzmann statistics with a chemical potential ruled by their density and temperature. At higher densities, excitons deviate more and more from ideal bosons until they eventually form an electron-hole plasma made up entirely of fermions. This makes the creation of a Bose-condensed state of excitons a very complicated problem and indeed no clearcut observation of a spontaneous Bose condensation of excitons has been reported so far.

2.1.3 Effects of confinement

By stacking layers of different semiconductor materials, confinement of excitons is possible along one, two or three dimensions, creating quantum wells, quantum wires or dots respectively. For a free particle with effective mass m^* confined in a crystal by impenetrable barriers (i. e., infinite potential energy) in the z direction, the allowed wavevectors k_z of the Bloch waves are given by

$$k_{zn} = \frac{2\pi}{\lambda_n} = \frac{n\pi}{L}, \tag{2.6}$$

where $n = 1, 2, 3..$and its ground state energy is increased by the amount ΔE compared to the unconfined case:

$$\Delta E = \frac{\hbar^2 k_z^2}{2m^*} = \frac{\hbar^2}{2m^*}\frac{\pi^2}{L^2}. \tag{2.7}$$

This increase in energy is a consequence of the uncertainty principle in quantum mechanics and is referred to as the confinement energy of the particle. Confinement within a distance L in space (along the z direction in this case) increases the uncertainty in the z component of its momentum by an amount of the order of $\hbar/L$. Hence this effect is known also as quantum confinement. Apart from increasing the minimum energy of the particle, confinement also causes quantization of its excited state energies. For an infinite one dimensional square well potential the excited state energies are given by $n^2\Delta E$, where $n = 1, 2, 3...$ (Figure 2.4).

Quantum confinement has a further effect on the valence band structure (Figure 2.5). The translational symmetry is broken lifting the degeneracy between the two light hole

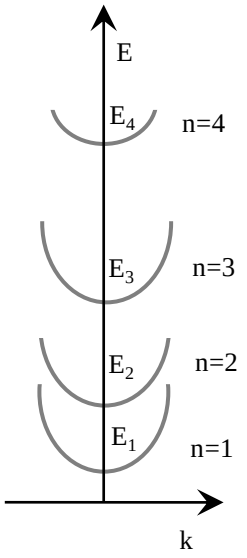

FIGURE 2.4: Discrete energy levels in a quantum well.

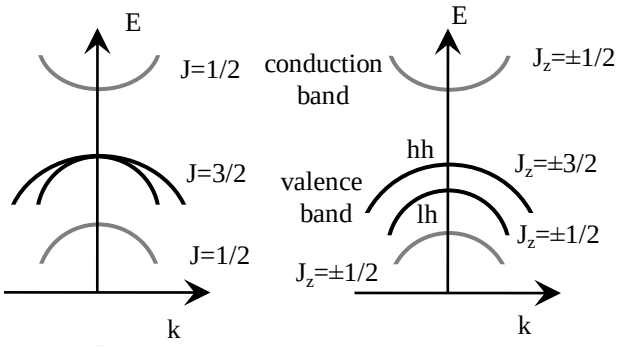

FIGURE 2.5: Band structures for III-V semiconductors in (a) bulk and (b) QW.

and two heavy hole bands found in 3D structures, bringing the heavy hole band closer to the conduction band than the light hole.

Confinement affects also the density of states (DOS) of the system. Calculated DOS in various confinement configurations can be found in Figure 2.6 [42]. The transition probabilities between the states, which are usually calculated using Fermi's Golden Rule (Appendix A) involve the density of final states, and are therefore affected as well by confinement.

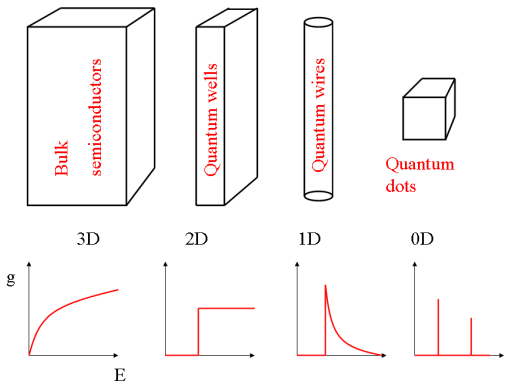

FIGURE 2.6: Energy density of states $g(E) = dN/dE$ in 3D, 2D, 1D and 0D structures, where dN is the number of electron quantum states within the energy interval dE. [42]

2.2 Cavities: light confinement

Microcavities are nanostructures that consist of a planar Fabry-Perot cavity sandwiched between two distributed Bragg reflectors (DBRs). The latter consist of alternate $\lambda/4$ layers of semiconductor materials of high and low refractive index, where λ (λ_{air}/n) is the design wavelength in the layer material. Their periodic structure gives rise to interesting properties and mirror-like behaviour. Their reflectance is influenced by the number, refractive indices and thickness of the layers. The transfer matrix method (Appendix B) is usually used to calculate the above properties (Figure 2.7). DBRs exhibit some advantageous properties such as extremely high reflectivity spectrum, negligible absorption losses and the possibility of non-resonant excitation coupling with the intracavity field.

The thicknesses of the layers are chosen so that the reflected light in the cavity interferes positively within a spectral range, called the *stop band*, a broad band high reflectivity region centred on λ_{air}, with oscillating side lobes (Figure 2.7). The reflectivity is given by [43]

$$R = 1 - 4\frac{n_{ext}}{n_c}\left(\frac{n_L}{n_H}\right)^{2N}, \tag{2.8}$$

where n_L, n_H, n_c and n_{ext} are the refractive indices of the low - and high - index layer, the cavity and the external medium. N is the number of pairs of mirror layers. High reflectivity values, of up to 99% can be achieved.

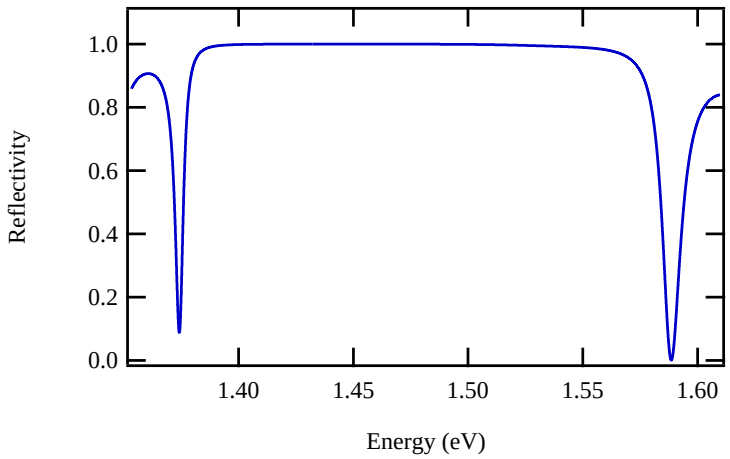

FIGURE 2.7: Reflectivity spectrum of a DBR, calculated via the transfer matrix technique.

A cavity is formed when two Bragg mirrors are stacked around a layer of thickness L_c, called the cavity spacer. As the spacer index is lower than the index of the first mirror layer, the cavity modes show an antinode at the interference of the two layers. The thickness of the cavity is usually

$$L_c = N\frac{\lambda}{2}, \tag{2.9}$$

where N is just an integer. The microcavity structure is very similar to a simple Fabry - Perot structure with planar mirrors. However, due to the penetration of the cavity field in the DBRs, the cavity length is [44, 45]

$$L_{eff} = L_c + L_{DBR} \tag{2.10}$$

with the penetration length into the DBRs being

$$L_{DBR} = \frac{\lambda}{2n_c}\frac{n_L n_H}{n_L - n_H}. \tag{2.11}$$

Figure 2.8 gives an example of the reflectivity spectrum of such a structure.

The resonant optical modes of the microcavity are defined by

$$\omega_m = \frac{N\pi c}{L_{eff} n_c}, \tag{2.12}$$

where n_c is the refractive index of the cavity and N is just an integer. The first mode is given for $N = 1$.

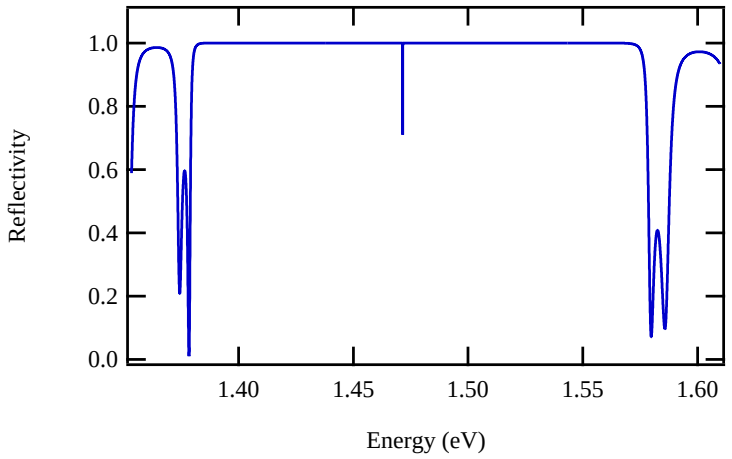

FIGURE 2.8: Reflectivity spectrum of a cavity, calculated via the transfer matrix technique.

As an optical resonator, the cavity is characterized by its quality factor, which measures the energy storage time compared to the loss rate, and is defined as [46]

$$Q = \frac{\omega_m}{\delta\omega}, \tag{2.13}$$

where ω_m is the optical mode resonance and $\delta\omega$ its spectral linewidth.

2.2.1 Dispersion of intra cavity photons

A planar cavity provides no confinement perpendicular to the growth axis, so the photons' in-plane dispersion is not altered. It does, however, impose a quantization of the wavevector in the growth direction (z). The mirrors force the axial wavevector in the medium to be

$$k_z = \frac{2\pi}{L_c}. \tag{2.14}$$

Therefore, the cavity photon energy becomes

$$E_c(k) = \frac{\hbar c}{n_c} k_z \left(1 + \frac{k_\parallel^2}{k_z^2}\right)^{1/2} = \frac{\hbar c}{n_c}\frac{2\pi}{L_c} + \frac{\hbar c}{2n_c}\frac{k_\parallel^2}{\frac{2\pi}{L_c}} = E_0 + \frac{\hbar^2 k_\parallel^2}{2m_{ph}}, \tag{2.15}$$

which is parabolic-like around $k = 0$ (Figure 2.9). An effective mass can be attributed to the intra cavity photon, deduced from the curvature of the above equation

$$m_{ph} = \frac{hn_c}{cL_c}. \tag{2.16}$$

This mass is extremely light [47] compared to the exciton mass and usually amounts to $10^{-5}m_e$, where m_e the free electron mass or $10^{-4}m_{exc}$, where m_{exc} the exciton mass.

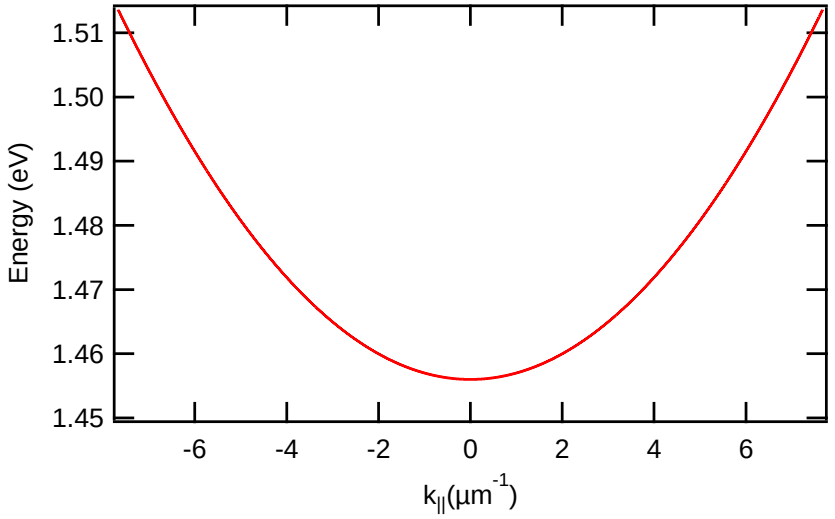

FIGURE 2.9: Dispersion of intra-cavity photons, as a result of confinement.

Finally, $k_{\|}$ is directly proportional to the external angle of incidence θ since

$$k_{\|} = \frac{E_c(k)}{\hbar c}\sin(\theta). \tag{2.17}$$

2.3 Light matter interaction

2.3.1 Strong coupling regime: Polaritons

In order to obtain a significant interaction between the two modes, the cavity mode is chosen to be at resonance with the exciton transition in the quantum structure embedded in the cavity. Coupling between the two may lead to either crossing or anticrossing of the real parts of the eigenfrequencies of the structure modes, called exciton - polariton modes.

Exciton-polaritons are half light, half matter quasiparticles, combining the properties of excitons and photons. Predicted theoretically by Hopfield and Agranovich in the late 1950 [6, 48], exciton-polaritons have been studied extensively in the past decade. They can be interpreted as virtual exciton-photon pairs, whose propagation in the crystal is a result of multiple virtual absorption and emission processes of photons by the excitons. They also behave as bosons in the low density regime [49] (Chapter 3).

2.3.1.1 Principles

The pioneering work of Purcell [50] proved that the emission probability of a two level atom, placed at the antinode of an electromagnetic wave under confinement in a Fabry-Perot cavity is enhanced. In the strong coupling regime between the two modes, where the energy exchange between the two is faster than the individual decay rates, the eigenmodes of the system are a superposition of the atomic excited state and the cavity mode. Similar situations occur in the strong coupling regime of a cavity photon and an exciton. The new eigenmodes of the system are called polaritons and they are the true eigenmodes of the system.

The Hamiltonian of the coupled exciton photon system reads as follows [51]:

$$H_0 = \sum_{k_{||}} E_C(k_{||}) \alpha^\dagger_{k_{||}} \alpha_{k_{||}} + \sum_{k_{||}} E_X(k_{||}) b^\dagger_{k_{||}} b_{k_{||}} + \sum_{k_{||}} \hbar\Omega_R (\alpha^\dagger_{k_{||}} b_{k_{||}} + b^\dagger_{k_{||}} \alpha_{k_{||}}), \tag{2.18}$$

where $\alpha^\dagger_{k_{||}}, \alpha_{k_{||}}$ and $b^\dagger_{k_{||}}, b_{k_{||}}$ are respectively the creation and annihilation operators for photons and excitons with the corresponding in-plane wavevector $k_{||}$. $\hbar\Omega_R$ describes the coupling energy between the modes, which depends on the overlap of the exciton's and cavity photon's wavefunctions. For QWs placed close to the electric field antinodes, the vacuum Rabi splitting is [52]

$$\hbar\Omega_R \approx 2\hbar \left(\frac{2\Gamma_0 c N_{qw}}{n_c L_{eff}} \right)^{1/2} \tag{2.19}$$

,

where N_{qw} is the number of wells in the cavity and Γ_0 is the radiation rate of a free exciton. It is usually maximized by increasing the number of quantum wells at the cavity mode antinode, and hence the total oscillator strength.

The eigenenergies of the above Hamiltonian are therefore

$$E_{LP,UP}(k_{||}) = \frac{E_X(k_{||}) + E_C(k_{||})}{2} \pm \frac{1}{2}\sqrt{\left(\delta(k_{||})\right)^2 + 4\hbar^2\Omega_R^2}, \tag{2.20}$$

where $\delta(k_{||}) = E_X(k_{||}) - E_C(k_{||})$ is the detuning between the cavity and the exciton resonance. The anticrossing of the two polariton energies as the cavity energy gets tuned across the exciton resonance is considered one of the main signatures of strong coupling (Figure 2.10). The minimun separation between the two polariton modes occurs when $E_X = E_C$ and is equal to $2\hbar\Omega$, which is called the 'vacuum Rabi splitting'.

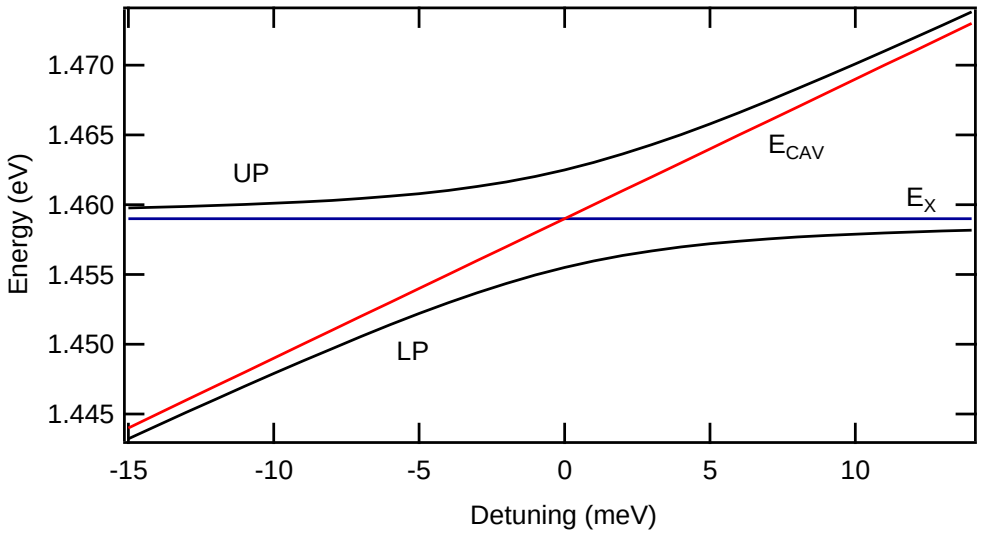

FIGURE 2.10: Calculated anticrossing of the lower (LP) and upper (UP) polariton energy levels while tuning the cavity energy (E_{CAV}) across the exciton resonance (E_X).

By using the original photon exciton basis one can write:

$$\begin{pmatrix} p_{k_{||}} \\ q_{k_{||}} \end{pmatrix} = \begin{pmatrix} X_{k_{||}} & C_{k_{||}} \\ -C_{k_{||}} & X_{k_{||}} \end{pmatrix} \begin{pmatrix} b_{k_{||}} \\ \alpha_{k_{||}} \end{pmatrix} \tag{2.21}$$

where $p^\dagger_{k_{||}}$, $p_{k_{||}}$ and $q^\dagger_{k_{||}}$, $q_{k_{||}}$ are respectively the creation and annihilation operators for the lower and upper polariton. $X_{k_{||}}$ and $C_{k_{||}}$ are called the Hopfield coefficients, introduced by Hopfield *et al.* in 1958 [6]. They are equal to (Figure 2.11)

$$|X_{k_{||}}|^2 = \frac{1}{2}\left(1 + \frac{\delta(k_{||})}{\sqrt{\delta(k_{||})^2 + 4\hbar^2\Omega^2}}\right) \tag{2.22}$$

$$|C_{k_{||}}|^2 = \frac{1}{2}\left(1 - \frac{\delta(k_{||})}{\sqrt{\delta(k_{||})^2 + 4\hbar^2\Omega^2}}\right). \tag{2.23}$$

Finally the diagonalised Hamiltonian is written in the polariton basis as:

$$H_0 = \sum_{k_{||}} E_{LP}(k_{||}) p^\dagger_{k_{||}} p_{k_{||}} + \sum_{k_{||}} E_{UP}(k_{||}) q^\dagger_{k_{||}} q_{k_{||}}. \tag{2.24}$$

2.3.2 Weak coupling regime

The system remains in the strong coupling regime as long as the energy exchange is faster than the decay rates. When lost, the system operates in the weak coupling regime. Reasons for this transition are the increase of the exciton's linewidth and the decrease of the coupling strength between the photon and exciton modes of the system. Both conditions usually occur at high excitation densities, due to the loss of the bosonic character of excitons as the free carriers can no longer form excitons and become an electron-hole plasma.

2.4 Relaxation mechanisms in microcavities

The most striking physics behind microcavities are due to their peculiar dispersion properties. Upon laser excitation of the semiconductor microcavity, coherent electron-hole pairs are generated, interacting with one another. As a result, they lose their coherence and are redistributed in reciprocal space. These 'hot' carriers exchange their kinetic energy with the lattice, mostly with optical phonons (Chapter 2.4.1). During this process, depending on their density and the lattice temperature, carriers may form excitons and populate the exciton dispersion. Then, they relax along the dispersion curve by interacting with acoustic phonons. It can be seen that the lower polariton branch is strongly non-parabolic. Its central part is characterized by an extremely light photon-like effective mass, while its outer parts have a relatively heavy exciton effective mass. In the central zone excitons are coupled to the light while in the rest of reciprocal space excitons are dark due to the wavevector mismatch with light. As the depth of this trap is usually larger than the thermal energy at low temperature, polaritons cannot be scattered back

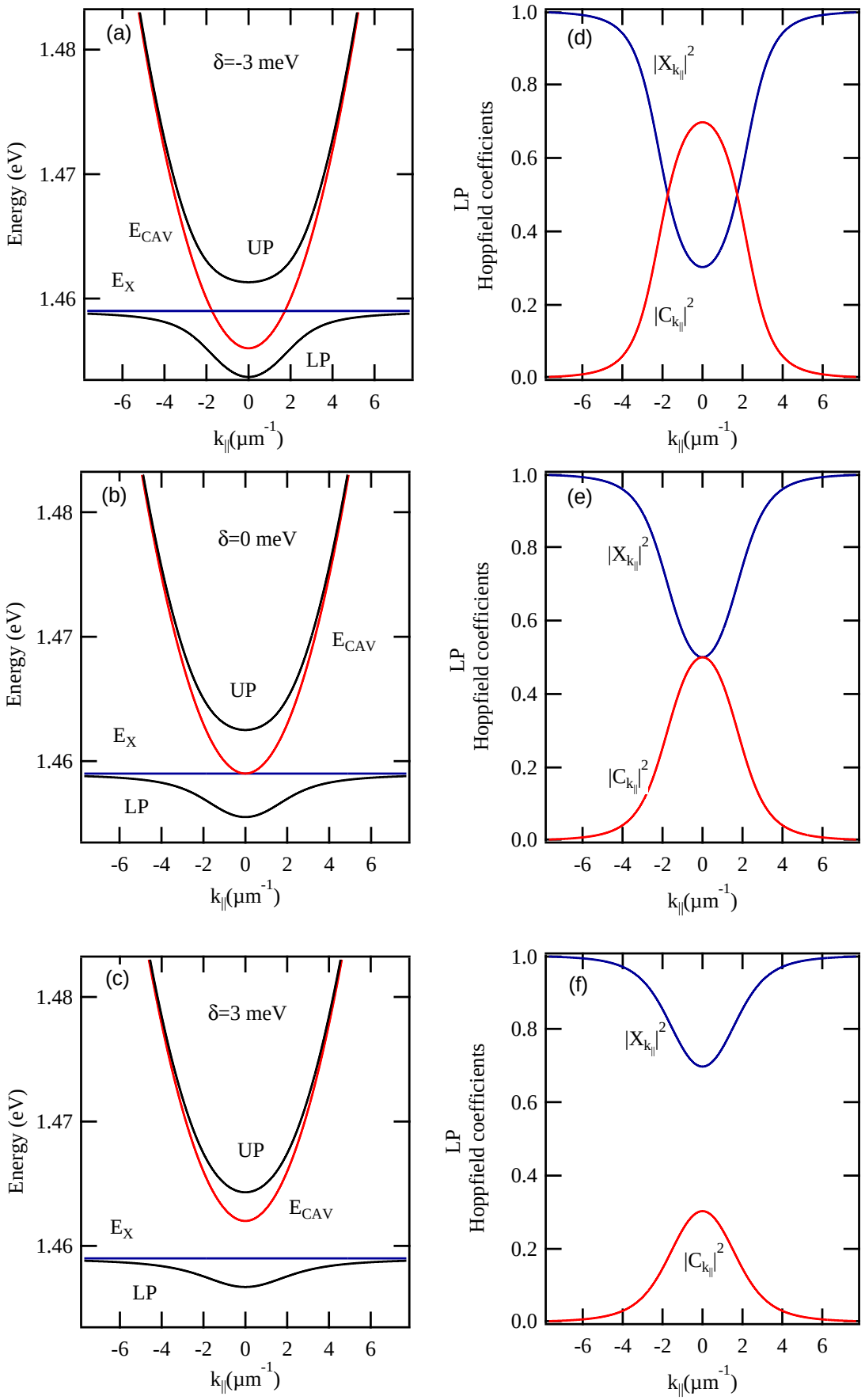

FIGURE 2.11: Polariton dispesions and corresponding Hopfield coefficients for (a) positive (b) zero and (c) negative detuning between the cavity and the exciton mode. (d-f) correspond to the corresponding LP Hopfield coefficients.

to exciton states, hence the assigned name 'polariton trap'. Polaritons as the superposition of excitons and photons can be considered as composite bosons. Following bosonic statistics, accumulation in the same energy state is allowed for a large population of particles. For polaritons, the driving force behind ground state condensation is final state stimulated pair polariton scattering, occurring in the nonlinear regime.

However, their relaxation towards the bottom of the trap is hindered by the energy and momentum conservation rules, leading to their accumulation in higher wavevector states along the dispersion from where the light is mostly emitted [53, 54]. This strong 'bottleneck' remained until recently the main restraint to ground state condensation, which equals emission of coherent monochromatic light. Attempts to increase occupancy of the polariton states usually have the opposite results as the increase in the exciton density above the screening density causes the complete loss of the strong coupling. Here lies the key advantage of CdTe against GaAs, as the higher exciton binding energy leads to increased screening density. Bleaching is prevented in resonant pumping experiments [8]. However, condensation can't strictly occur under those circumstances as stimulation and coherence properties are strongly driven by the excitation laser itself. Other mechanisms overcoming the bottleneck include electron-polariton scattering [55], which does indeed enhance polariton relaxation through scattering with free carriers. This mechanism though is much weaker than pair polariton scattering [56].

Lately, growth efforts have targeted the production of samples with much higher lifetimes. The onset of polaritons scattering is governed by the ratio between polariton lifetime and polariton relaxation times. Therefore increase of the lifetime in the range of 100 ps should facilitate polariton condensation in GaAs. The main physical processes involved in the relaxation of polaritons follow in the next sections.

2.4.1 Phonons

Phonons are quanta of lattice vibrations, mainly resulting from the lattice thermal energy [35]. Assuming interactions in a one-dimensional lattice, with coupling only to the nearest-neighbour and two different masses m_1 and m_2 placed alternately, the frequencies

of oscillation are given by

$$v_{\pm} = \sqrt{a_f}\left[\left(\frac{1}{m_1}+\frac{1}{m_2}\right) \pm \sqrt{\left(\frac{1}{m_1}+\frac{1}{m_2}\right)^2 - \frac{4sin^2(k_{ph}a/2)}{m_1 m_2}}\right]^{1/2} \tag{2.25}$$

where a_f is the force constant of the Hooke's law, k_{ph} the phonon wave number, and a the lattice spacing. The frequency v_- is proportional to k_{ph} near $k_{ph} = 0$ and corresponds to the so called 'acoustic branch', as the velocity ω/k nears that of sound in such a medium. The frequency v_+ tends to be a constant $\simeq [2a_f(1/m_1 + 1/m_2)]^{1/2}$ as k_{ph} approaches zero. As the frequency v_+ is generally in the optical range, this branch is named 'optical branch'. For the acoustic mode the two sublattices of the atoms with different masses move in the same direction, whereas for the optical mode they move in opposite directions. Modes with atoms displaced along the direction of the wavevector are called longitudinally polarized modes while modes with atoms moving in the planes normal to the wavevector are called transversely polarized modes.

Figure 2.12 shows the measured results for GaAs in one of the crystal directions [57].

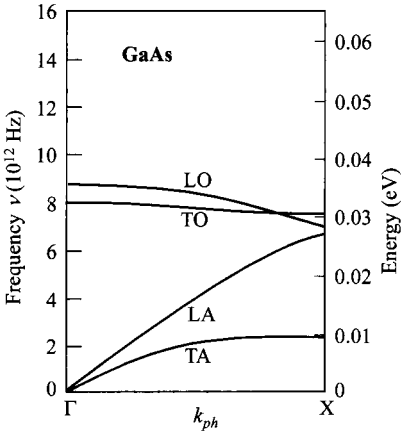

FIGURE 2.12: Measured phonon spectra in GaAs. TO and LO correspond to transverse and longitudinal optical modes, and TA and LA to transverse and longitudinal acoustic modes [57].

2.4.1.1 Optical phonons

Relaxation via optical phonons becomes prevalent for high carrier temperatures [58] and is independent of the lattice temperature [59]. The electron hole gas created upon optical

non-resonant excitation exchanges its excess energy with the lattice mainly via optical phonons and cools down to a temperature less than ω_{LO}/k_BT in few picoseconds. Exciton formation via this mechanism may be neglected when the excess energies in excitation are smaller than the optical phonons energy, which is typically 36 meV in GaAs. Chapter 5 is devoted to the enhancement of polariton relaxation towards the ground state via the optical phonon' s resonance.

2.4.1.2 Acoustic phonons

Interactions with acoustic phonons are less efficient as each step needs about 10 ps and no more than 1 meV of energy can be exchanged. Overall more than 100 ps are needed for the polaritons to reach the bottleneck even, which is far longer than their lifetime. The energy and wavevector conservation makes it impossible for polaritons to jump to the bottom of the trap in one single step via acoustic phonons and achieve thermal equilibrium [58].

The terms in the rate equations for relaxation from the exciton reservoir via acoustic phonons to an energy level i are:

$$\frac{\partial n_x}{\partial t} = \sum_i A_{i\to x} n_i (n_x + 1) - \sum_i A_{x\to i} n_x (n_i + 1) \tag{2.26}$$

with

$$A_{j\to j} = 1 + \frac{1}{e^{\frac{E_j - E_i}{k_B T}}} = \frac{1}{1 - e^{\frac{E_i - E_j}{k_B T}}} \approx 1 + e^{\frac{E_i - E_j}{k_B T}}. \tag{2.27}$$

2.4.2 Exciton-exciton scattering

Through the interaction between excitons, the fermionic nature of the electron and the hole that constitute the exciton is taken into account. Scattering of two excitons from the reservoir can result in one exciton and a polariton (upper or lower) or in two polaritons, one upper and one lower. Further scattering involving the lower polariton as final state will be stimulated upon existence of a macroscopic population in that state [54].

The term in the rate equations for the interaction between an excitonic reservoir x and a state i with an excitonic Hopfield coeeficient X_i is:

$$\frac{\partial n_x}{\partial t} = \sum_i B_{x\to i} n_x^2 (X_i n_i + 1). \tag{2.28}$$

2.4.3 Pair polariton scattering

This is an elastic scattering mechanism, a dipole-dipole interaction with a typical timescale of a few picoseconds and energy exchange of few meV. As two polaritons scatter from state M2, one arrives at the bottom of the trap (M1) where it rapidly decays whereas the other one gains energy and gets scattered at higher k-states (M3). Although this interaction doesn't dissipate energy or reduce the polariton gas temperature, it is the main process for overcoming the bottleneck effect [42].

The terms in the rate equations for pair scattering between three states M1, M2 and M3 are:

$$\frac{\partial n_{M1}}{\partial t} = -n_{M1} n_{M3} (n_{M2} + 1)^2 + (n_{M2})^2 (n_{M1} + 1)(n_{M3} + 1) \tag{2.29}$$

$$\frac{\partial n_{M2}}{\partial t} = 2 n_{M1} n_{M3} (n_{M2} + 1)^2 - (n_{M2})^2 (n_{M1} + 1)(n_{M3} + 1) \tag{2.30}$$

$$\frac{\partial n_{M3}}{\partial t} = -n_{M1} n_{M3} (n_{M2} + 1)^2 + (n_{M2})^2 (n_{M1} + 1)(n_{M3} + 1). \tag{2.31}$$

2.5 Spin properties of polaritons

As all bosons, polaritons have an integer spin, the same as the exciton spin. As excitons are the combination of two fermions, spin conservation is required for their interactions. Electrons in the conduction band with s-symmetry have projections of the angular momenta on a given axis equal to $m_j = \pm\frac{1}{2}$ while holes in the valence band with p-symmetry have $m_j = \pm\frac{1}{2}, \pm\frac{3}{2}$, which corresponds to light hole and heavy hole excitons respectively (Figure 2.13). The total angular momentum J of an exciton spin can have projections ±1 and ±2 on the structure axis. Only excitons with spin projections ±1 can be optically excited, as photon spin is 0 or ±1, and are therefore called 'bright states'. As stated in Chapter 2.1.3, the quantum confinement lifts the degeneracy of light- and heavy-hole

states, resulting in the heavy holes lying closer to the conduction band, than the light holes.

The spin of polaritons defines the polarisation properties of the emitted photons, rendering the investigation of spin dynamics extremely intriguing [60].

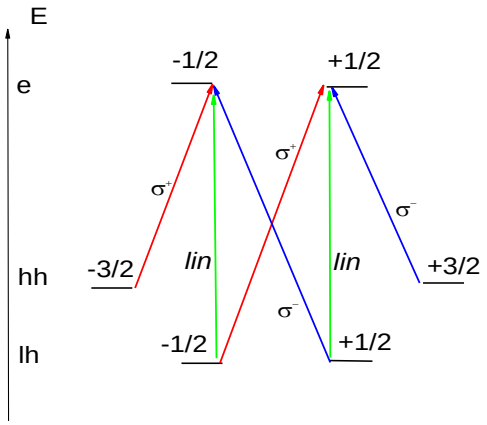

FIGURE 2.13: Polarization of optical transitions in zincblende semiconductor quantum wells. Red, blue and green lines show σ^+ , σ^- and linearly polarized transitions, respectively.

2.5.1 Pseudospin formalism

The polarization of light can be fully characterised through the Stokes parameters, which are given by

$$\rho_L = \frac{I_{HOR} - I_{VER}}{I_{HOR} + I_{VER}}, \quad \rho_D = \frac{I_{DIAG1} - I_{DIAG2}}{I_{DIAG1} + I_{DIAG2}}, \quad \rho_C = \frac{I_{\sigma^+} - I_{\sigma^-}}{I_{\sigma^+} + I_{\sigma^-}} \tag{2.32}$$

where L and D denote the linear and diagonal degree respectively, measured in the xy plane while C represents the circular degree of polarization. The various intensities, I, can be collected through half-wave plates oriented at 0°, 90° and ±45°; I_{σ^+} and I_{σ^-} represent the intensities that correspond to the degree of right- and left- hand circular polarised light collected through quarter-wave plates oriented at 0° and 45°. The most convenient way to treat polariton spin in microcavities is by means of the pseudospin formalism. Introduced by Richard Feynman to facilitate the description of the behaviour of any two level systems [61], the formalism was adapted by Kavokin *et al.* [62, 63] in order to describe polariton relaxation mechanisms in microcavities. It consists of

a pseudospin vector **S**, defined by the two quantum states of the radiative polariton doublet, to simultaneously describe of the exciton spin state and its dipole moment orientation. The pseudospin componentscorrespond directly to the Stokes parameters of emitted light and $|\boldsymbol{S}| \leq 1/2$. States around the equator of the sphere correspond to eigenstates of S_x and S_y, yielding linear polarization. When the pseudospin is (anti-) parallel to the x-axis, it corresponds to (y-) x-polarized light, while orientation across the y-axis describes diagonal polarization (Figure 2.14). States across the z-axis correspond to circular polarization. Other points on the pseudospin sphere correspond to the general case of elliptical polarization.

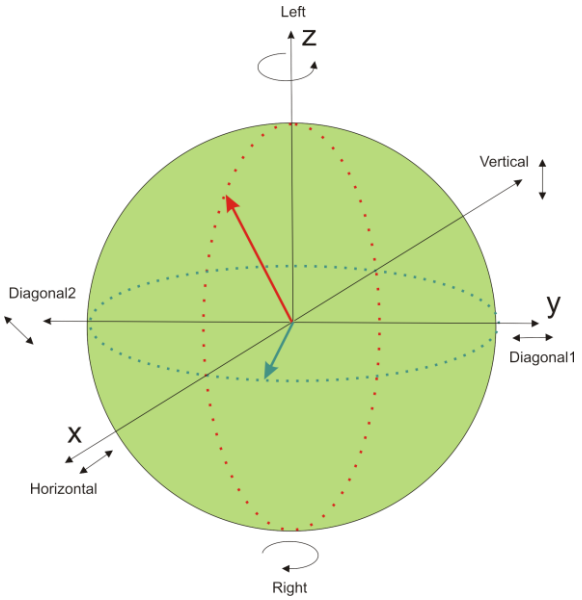

FIGURE 2.14: The pseudospin vector represents the polariton polarization and lies on the surface of the Poincare sphere for a pure polarized state.

2.6 Summary

In this chapter the basic concepts of confined excitons and photons that lead to the rise of polaritons in semiconductor microcavities are reviewed. Fascinating phenomena that spring from their bosonic nature, such as polariton condensation, a type of non-equilibrium Bose-Einstein condensation are explained in detail in the following chapter.

Chapter 3

Polaritons as bosons

Surprisingly, a large number of modern physics ideas have sprung from Einstein's work. One of the most intriguing is Bose-Einstein condensation (BEC), a phase transition where a large number of particles accumulate in the lowest energy state of the system. Although BEC has been recently demonstrated in atomic systems at ultra low temperatures, the possibility of room temperature observation of BEC in excitonic systems has triggered intense research the last years.

In this chapter, an overview of the basic properties of BEC is provided, including Bogoliubov's breakthrough approach that provided the basis for a complete theoretical approach unifying BEC, superfluidity and lasing on the basis of long range coherence. The reasons that render microcavity polaritons appropriate for the study of BEC in solids are explained, including recent related experimental observations.

3.1 Bose-Einstein condensation

In the microscopic world, where the length scales are comparable to the size of the wave functions of the particles, the governing principle is that of indistinguishability: particles under study can be identical. The above idea leads to the fundamental division of particles in two categories: *bosons*, described by symmetric wave functions and possessing integer spin and *fermions*, described by antisymmetric wave functions and possessing half-integer spin. The latter category is governed by the Pauli exclusion principle, that forbids sharing of the same quantum state. Bosons on the other hand, can share the

same quantum state (constructive quantum interference). This character is exactly the origin of bosonic attraction and finally of Bose-Einstein condensation.

The bosonic symmetry leads to the bosonic commutation rules:

$$[b_j, b_k^\dagger] = \delta_{jk} \tag{3.1}$$

$$[b_j, b_k] = 0. \tag{3.2}$$

These equations show at a glance that the scattering rate towards a bosonic state is enhanced by the presence of other bosons in that state. Namely, if N particles are found in that state the scattering rate is proportional to (N+1) [64]. This triggers an avalanche like process: the higher the occupancy of the state, the faster its occupancy increases. This phenomenon, known as the bosonic final state stimulation, can be considered as the origin and basis of the BEC.

3.1.1 BEC of an ideal Bose gas

A gas of N free non-interacting Bose particles in thermal equilibrium at temperature T is distributed in momentum space according to the Bose statistics [65]

$$f_{BE}(\boldsymbol{k}, T, \mu) = \frac{1}{\exp\left(\frac{E(\boldsymbol{k})-\mu}{k_B T}\right) - 1} \tag{3.3}$$

where $E(\boldsymbol{k})$ is the dispersion function of bosons, $\boldsymbol{k}$ is the particle wavevector and μ is the chemical potential, which is fixed by the total number of particles in the system. In the limit $\mu << k_B T$ and $e^{\frac{-\mu}{k_B T}} >> 1$, the statistics are approximated by the Maxwell-Boltzmann distribution

$$f_{MB}(\boldsymbol{k}, T, \mu) = \exp\left(-\frac{E(\boldsymbol{k}) - \mu}{k_B T}\right). \tag{3.4}$$

The total particle number N is given by

$$N(T,\mu) = \sum_k f_{BE}(\boldsymbol{k},T,\mu) \tag{3.5}$$

$$= \frac{1}{\exp\left(\frac{-\mu}{k_B T}\right) - 1} + \sum_{k\neq 0} f_{BE}(\boldsymbol{k},T,\mu) \tag{3.6}$$

$$= N_{E=0}(T,\mu) + N_{E\neq 0}(T,\mu). \tag{3.7}$$

Assuming a ground state energy of $E_0 = 0$, μ has negative values and is increasing with the density. As $\mu \to 0$ the Bose-Einstein distribution starts diverging and the ground state occupancy $n_0 \simeq \frac{k_B T}{E_0 - \mu}$ becomes large without limit. However, (in the three dimensional case) the number $N_{E\neq 0}$ of particles found in excited states is limited even if $\mu = 0$ (thermodynamic limit) and is proportional to the system volume V. For a fixed temperature, two possible outcomes may occur. If the total number of particles can be distributed in the excited levels, the ground state occupancy is of the same order as the excited states. On the other hand, if N is larger than the critical density $N_{cr} = N_{E\neq 0}(T, \mu = 0)$ then a large number of particles must occupy the ground state in order to fulfil Equation 3.5. Inspired by the work of Bose [11], Einstein proposed this fascinating solution in [12]. Taking into account saturation of the excited states, additional particles start to massively occupy the lowest accessible quantum state and the population in the ground state becomes comparable with the total number of particles in the system. This saturation of the excited states and macroscopic occupation of the ground state is the phase transition called the Bose-Einstein condensation.

In the thermodynamic limit therefore, where $N, V \to +\infty$ with $N/V =$ constant and $\mu = 0$ the number density vanishes for any excited state:

$$n_{E\neq 0} = \frac{N_{E\neq 0}}{V} \to 0 \tag{3.8}$$

while the ground state

$$n_{E=0} = \frac{N(T) - N_{cr}(T)}{V} \tag{3.9}$$

becomes finite when the total number of particles exceeds $N_{cr}(T)$ and a macroscopic number of particles condenses into the single microscopic ground state.

For an ideal, non interacting Bose gas, the critical particle density is given by [66]

$$n_c(T_c) = \frac{N_{E\neq 0}(T,\mu)}{V} = \left(\frac{2.612}{\lambda_{dB}^3}\right). \tag{3.10}$$

For temperatures below T_c, the condensate fraction $n_{E=0}/n = 1 - (T/T_c)^{3/2}$, while it goes to zero as the temperatures rise.

The above equation shows that quantum correlations survive only in the scale of the thermal de Broglie wavelength [67, 68]. As $n_c \propto \lambda_{dB} T_c^d$, where d is the dimension, it follows that the critical temperature is inversely proportional to the mass:

$$T_c \propto 2\pi\hbar^2 n_c^{-2/d}. \tag{3.11}$$

3.1.2 Bogoliubov theory of BEC

Bogoliubov presented in 1947 a microscopic description of a condensed weakly interacting Bose gas [69]. Through his innovative approach, he laid down the framework for the modern definition of BEC. In the Bogoliubov approximation the condensate is treated classically [68, 70] and is characterized by a single macroscopic wave function

$$\Psi(r) = \sqrt{N_0}|\psi(r)|exp(i\phi(r)) \tag{3.12}$$

where n_o is the number of condensed particles, $\psi(r)$ is the single particle wave function of the ground state and $\phi(r)$ is the phase characterizing coherence and superfluid phenomena [65]. This macroscopic wave function of the condensate $\Psi(r)$ can be considered as an order parameter for the BEC: a macroscopic quantity that emerges at the transition point. Making an explicit choice of the phase of the order parameter formally corresponds to the symmetry breaking in the system: in fact, any physical properties stay unchanged when varying the phase.

The Hamiltonian of an interacting Bose gas can be written as:

$$H = \sum_{\boldsymbol{k}} E(\boldsymbol{k}) a_{\boldsymbol{k}}^\dagger a_{\boldsymbol{k}} + \frac{1}{2}\sum_{\boldsymbol{k},\boldsymbol{k'},\boldsymbol{q}} V_{\boldsymbol{q}} a_{\boldsymbol{k}+\boldsymbol{q}}^\dagger a_{\boldsymbol{k'}-\boldsymbol{q}}^\dagger a_{\boldsymbol{k}} a_{\boldsymbol{k'}} \tag{3.13}$$

where $a_{\boldsymbol{k}}$ and $a^{\dagger}_{\boldsymbol{k}}$ are annihilation and creation operators and V_q the Fourier transform of the interacting potential for the boson-boson scattering. Assuming complete condensation of the Bose gas, $a^{\dagger}_0$ and a_0 can be replaced by $\sqrt{N_0}$.

By keeping only the largest contributing parts of the Hamiltonian

$$H = N_0 V_0^2 + \sum_{\boldsymbol{k},k\neq 0} (E(\boldsymbol{k}) + N_0(V_{\boldsymbol{k}} + V_0)) a^{\dagger}_{\boldsymbol{k}} a_{\boldsymbol{k}} + N_0 \sum_{\boldsymbol{k}} V_q (a^{\dagger}_{\boldsymbol{k}} a^{\dagger}_{-\boldsymbol{k}} a_{\boldsymbol{k}} a_{-\boldsymbol{k}}). \tag{3.14}$$

The initial Hamiltonian can be diagonalized by the 'Bogoliubov' transformation:

$$a_{\boldsymbol{k}} = A_{\boldsymbol{k}} \alpha_{\boldsymbol{k}} - A^{*}_{-\boldsymbol{k}} \alpha^{\dagger}_{-\boldsymbol{k}} \tag{3.15}$$

$$a^{\dagger}_{\boldsymbol{k}} = A^{*}_{\boldsymbol{k}} \alpha^{\dagger}_{\boldsymbol{k}} - A_{-\boldsymbol{k}} \alpha_{-\boldsymbol{k}} \tag{3.16}$$

into

$$H = N_0 V_0^2 + \sum_{\boldsymbol{k}\neq 0} E_{Bog}(\boldsymbol{k}) \alpha^{\dagger}_{\boldsymbol{k}} \alpha_{\boldsymbol{k}} \tag{3.17}$$

as a function of the new, but still bosonic, operators α_k, $\alpha^{\dagger}_k$ with

$$E_{Bog}(\boldsymbol{k}) = \sqrt{E(\boldsymbol{k})^2 + 2E(\boldsymbol{k}) N_0 V_{\boldsymbol{k}}]} \tag{3.18}$$

where

$$E(\boldsymbol{k}) = \frac{\hbar^2 k^2}{2m} \tag{3.19}$$

is the unperturbed quadratic dispersion, recovered when $N_0 = 0$. Near $k = 0$ we obtain the infamous linear dispersion relation, approximated by

$$E_{Bog}(\boldsymbol{k}) \simeq \hbar k \sqrt{\frac{N_0 V_0}{m}}. \tag{3.20}$$

The above equation describes phonon-like waves in a continuous compressible medium. For BEC, they essentially represent many-body collective excitations and together with the long range correlation characterize a Bose gas undergoing condensation.

The Bogoliubov spectrum has been accurately measured for a diluted Bose gas, in the presence of interactions [68].

3.1.3 Condensation in 2D systems

In two dimensions, true BEC is not strictly possible, but a related phase transition known as the Kosterlitz-Thouless transition (KT) [71, 72]. In this case, spontaneous phase coherence of the particles occurs but doesn't persist to infinite range. Long wavelength thermal phase fluctuation destroys a long range order, so BEC exists only for $T = 0$, where there are quantum phase fluctuations. However, for $T > 0$, superfluidity is not necessarily destroyed by these phase fluctuations, hence the Kosterlitz-Thouless transition. The physical meaning between the two phenomena is the same: the particles accumulate as bosons in the same quantum state, which leads to spontaneous phase coherence.

The critical temperature for this to occur is [73]

$$k_B T_{KT} = n_s \frac{\pi \hbar^2}{2m^2} \tag{3.21}$$

where n_s is the superfluid density. Above this critical density, friction is produced by thermally excited vortices. Below T_{KT}, single vortices bind to form pairs allowing percolation of condensate droplets in which a phase coherent path exists between two points. Therefore n_s jumps to a non-zero value.

Any experimental system is though of finite size $S = L^2$, has a finite number of particles N and has discrete energy levels E_i, with $i = 1, 2, 3...$ The critical condition can be defined as

$$\mu = E_1 \tag{3.22}$$

$$n_c = \frac{1}{S} \sum_{i \geq 2} \frac{1}{\exp(\frac{E_i}{k_B T}) - 1} \tag{3.23}$$

and can now be fulfilled for $T_c > 0$. The critical density becomes

$$n_c = \frac{2}{\lambda_{dB}^2} ln \left(\frac{L}{\lambda_{dB}} \right). \tag{3.24}$$

If the particle number N is sufficiently large, the transition shows similar features as a BEC transition in the thermodynamic limit [74].

3.2 Polariton condensation

The first unambiguous proof for a BEC in weakly interacting systems came from atomic physics in the 90's, when massive occupation of the ground state and long-range coherence [14] of cold, trapped alkali atoms were demonstrated. Research focused on excitonic systems the light effective mass should enable excitonic BEC at temperatures available by standard cryogenic means [15, 16]. Nevertheless, no unambiguous proof of excitonic BEC has been presented.

The growth of advanced heterostructures comprised of quantum wells sandwiched in a Fabry Perot cavity gave rise to polaritons. Their even lighter mass, due to their photonic component immediately set them on the frontline of BEC related research, as it sets the critical temperature for condensation above 300K. From an experimental viewpoint, polariton structures are incredibly accessible systems. Internal polaritons with specific momentum are coupled to external photons of the same energy and wavevector, propagating at an angle θ from the growth direction. As a result polaritons can be conveniently excited and their properties can be measured using standard optical techniques, that provide access to their energy-momentum dispersion, populations, distribution functions etc. The main drawback is their very short lifetime that hinders thermalization. However, strong pair polariton interaction, result of their excitonic component, occurs at even shorter timescales, allowing for thermalizaton.

Following Imamoglu's proposal of a polariton laser [7] (Chapter 3.3), a device operating without population inversion, the scientific community focused on the investigation of polariton BEC. Many of the early claims of BEC in GaAs structures had to be retracted, as the nonlinearities observed could not be attributed to bosonic stimulation behaviour, as the strong bottleneck prevented polariton relaxation towards $k = 0$ states. Attempts to increase occupancy usually led to increase of the exciton screening density above the screening density, disassociating excitons and resulting in electron hole plasma. The strong coupling was lost along with the possibility of polariton stimulation.

BEC was finally observed in CdTe microcavities [21]. Compared to GaAs, it exhibits a much higher saturation density, thanks to the higher exciton binding energy. Starting from experimental evidence of polariton stimulation, first claim of polariton condensation was only remotely connected to BEC as it occured in a ring of finite k values and not at

the ground state as expected [24]. This unusual observation is connected with the size of the excitation spot. The small spotsize prevented relaxation towards the lower energy state. Use of a larger spot led to observation of the first clear cut evidence of BEC in a polariton system [75].

Following this remarkable achievement, polariton condensates have been thoroughly investigated. Most experimental observations [21, 25, 76] include spectral and momentum narrowing, and long-range order. However they bare similarities with evidence from a pure photonic laser [77]. The theory also predicts the occurrence of a spontaneous symmetry breaking in a condensate formed non-resonantly. In the case of polaritons, it should be manifested via the build-up of a well defined linear polarization of the emission of the condensate [78–80], spontaneously chosen by the system direction [81]. Such linear polarization has been reported [21, 25, 76, 82], pinned however to some predefined crystallographic direction. Nevertheless, spontaneously selected polarization has been reported in a room temperature polariton condensation, realized in a bulk GaN microcavity [83].

An additional landmark that distinguishes a Bose-Einstein condensate of interacting polaritons and a condensate of non-interacting photons (a laser), is the observation of superfluid properties in the polariton condensate [84, 85]. Superfluidity is manifested via the creation of an irrotational fluid $\nabla \times v = 0$, where v is the fluid velocity and the linear spectrum of excitations around zero momentum (Bogoliubov dispersion). Polariton dispersions resembling the Bogoliubov spectrum, have already been reported [26]. Superfuidity in polariton condensates in the framework of "flow without friction" has been achieved, focused on the scattering properties of a moving polariton fluid encountering a localized potential barrier [31, 32]. The slope of the linear spectrum at the small momentum regime corresponds to a critical fluid velocity, which is the lower limit of perturbations in the fluid caused by static external potentials, and allows for frictionless movement. A 'Cerenkov' like pattern is observed as the flow velocity exceed the speed of sound [86].

The formation of vortices with quantized angular momentum or persistent currents comes as a result. Direct evidence of polariton superfluidity include observations of a quantized vortex pinned to a potential defect [33] and a vortex-antivortex bound pair in a finite size polariton condensate [87]. Persistent currents consist of an indefinite rotation of the

superfluid with a fixed angular frequency, after the removal of the initial stirring force. Observations of this behaviour have been reported in He-II [88], atomic condensates [89] and, recently, in polariton systems [34].

Polaritons though don't cease to be two dimensional quasiparticles, and as such they cannot really exhibit a strict BEC phase transition. Spatial localization of polaritons in the photonic disorder in the cavities allows for local condensation or so called Kosterlitz-Thoules phase transition towards superfluidity (Chapter 3.1.3). The size of the polariton cloud is finite and complete coherence and macroscopic population of a single quantum state can be achieved. It needs to be stressed that polariton condensation differs in many ways from Einstein's proposal: the polariton gas is far from the ideal Bose gas and interactions play an important role. In this open system, polaritons leak out of the microcavity within their very short radiative lifetime ($\simeq 10-12$ ps), rendering continuous pumping necessary in order to compensate for the radiative losses. Further complications arise from the reduced dimensionality, the finite size and the intrinsic structural disorder. However, as the experimental findings suggest, accumulation of a large population in the ground state is possible.

3.2.1 Critical densities of 2D polaritons

Polaritons, as a 2D system do not undergo BEC at finite temperatures in the thermodynamic limit. BEC exists though if the system is of finite size (Chapter 3.1.3), as it occurs for the experiments presented in this thesis. Figure 3.1 presents the polariton phase diagram of polaritons in GaAs systems, following [42]. The solid line corresponds to the critical concentration for a KT phase transition. The broken lines show the approximate limit of the strong coupling regime, result of exciton screening by a photo-induced electron hole plasma (horizontal) or from broadening of the exciton resonance due to temperature increase (vertical). Below the critical density a microcavity operates as a light-emitting diode, while for values above it, the microcavity acts as a VCSEL.

3.3 Polariton laser

Emission of coherent light from the k=0 state of the polariton dispersion, comes as a natural consequence of the formation of the condensate. The similarities with BEC have

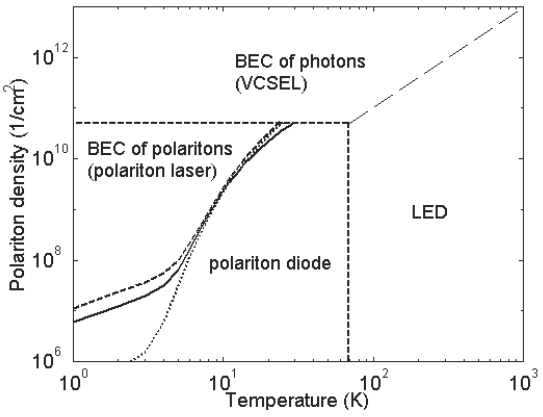

FIGURE 3.1: Vertical and horizontal dashed lines show the limits of the strong-coupling regime imposed by the exciton thermal broadening and screening, respectively. Solid lines show the critical concentration N_c versus temperature of the polariton KT phase transition. Dotted and dashed lines show the critical concentration N_c for quasicondensation in 100 μm and in one meter lateral size systems, respectively. The thin dashed line (upper right) symbolizes the limit between vertical-cavity surface-emitting laser (VCSEL) and light-emitting diode regimes. [42]

been highlighted in the previous chapter, but the term 'polariton condensate' will be used in the following chapters. Observation of the above characteristics has of course triggered research towards the development of a real life device, based on a semiconductor microcavity structure electrically pumped with carriers. Progress towards this goal has resulted in LEDs operating in the strong coupling regime [90–92]. However non-linearities of the strong coupling regime under the above conditions are yet to be achieved.

Here, the simple model of the polariton laser, based on [42], is discussed. A number of assumptions are included, however a comparison with conventional lasing from VCSELs already reveals the vast possibilites of polaritons in applications.

N_0 polaritons are coupled with an exciton reservoir of density N_X. The trap created in energy-momentum space has a depth of E_{TR}. Pair scattering events between polaritons across the polariton dispersion populate the $k = 0$ state. Energy and momentum must be conserved during these scattering events, therefore polaritons of high k must be involved. At those states though, their excitonic component is so high that one can talk of excitons.

Owing to the bosonic character of the particles, the scattering rate between states k_0, k_1, k_2 and k_3 for which the wavevector and energy conservation rules apply, as shown in

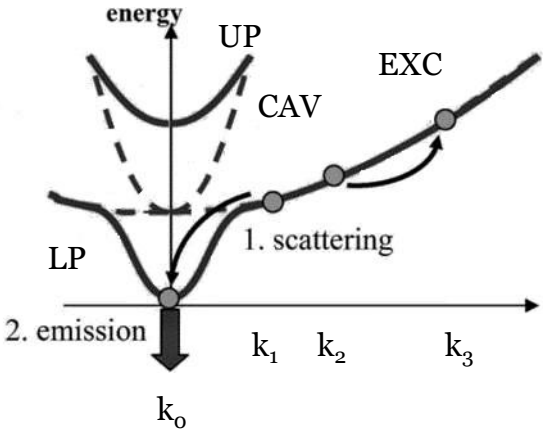

FIGURE 3.2: Dispersion of polariton-laser, showing pair scattering of polaritons at k_1, k_2 acting as a reservoir for the polariton trap at k=0.

Figure 3.2

$$\Gamma_{PS} = C[(1+N_0)f_1 f_2(1+f_3) - N_0 f_3(1-f_1)(1-f_2)] \tag{3.25}$$

depends on the occupation of the states involved. The first term describes the scattering rate towards the N_0 polariton condensate while the second one the re-ionization out of the trap. C stands for the Coulomb coupling rate and is proportional to $\epsilon^2/4\pi\epsilon_0\epsilon_B\alpha_B$, where α_b is the exciton Bohr radius. Assuming the states follow the Fermi distribution $f_i = 1/(1+\exp^{(E_i-E_f)/k_BT})$, it can be rewritten as:

$$N_0 R(N_X) + S(N_X) = \int dk_1 \int dk_2 \Gamma_{PS}(k_1, k_2) \tag{3.26}$$

where R and S are the stimulated and the spontaneous scattering rate respectively. Pair scattering occurs only if the Fermi level $E_f > E_{TR}$, as a sufficient number of excitons is needed to ensure population of high k energy states, for which energy-momentum conservation becomes possible. For low temperatures, $f_3 = 0$ and so $R = S$. Ground state occupation stimulates pair scattering towards the k=0 state only. Further increase of the population at k_1 and k_2 via temperature increases the pair scattering, but at the same time allows for ionization of polaritons out of the trap from very high-k excitons, reducing R compared to S. At low densities

$$S = cN_X^2 \tag{3.27}$$

$$R = c\left(N_X^2 - d\frac{\Gamma_0}{\Gamma_{nr}}N_X\right) \tag{3.28}$$

where d allows for polariton ionization, Γ_{nr} and Γ_0 are the non-radiative and radiative emission rates respectively. Below the threshold

$$P_{th} = \hbar\omega V\Gamma_{nr}\sqrt{\frac{\Gamma_0}{c}} \tag{3.29}$$

the output power is the result of spontaneous pair scattering

$$P_{out} = \hbar\omega V c\left(\frac{P}{\Gamma_{nr}}\right)^2 \tag{3.30}$$

Above threshold $P_{out} = P - P_{th}$. An intermediate regime with a second threshold rises when ionization of polaritons become significant and the strong coupling is lost.

The main advantage of a polariton laser against conventional lasing devices is the lifting of the carrier population inversion condition. Gain in VCSELs is connected to the stimulation of photons across the electron-hole transition, while the polariton-laser operates by stimulation of polaritons across the in-plane dispersion, which rapidly leads to photon emission. Gain is provided due to the exciton reservoir, existing at states much higher than the polariton emission. Pair scattering separates the processes of absorption and emission through control of the exciton k-distribution, in contrast to conventional lasers for which absorption and emission are intimately linked. 'Inversion' is defined through the integrated exciton density N_X. Spontaneous emission occurs as soon as more than one polariton builds up in the trap, and the pair scattering rate becomes stimulated by this final state occupation. This in turn depends on the pair scattering strength, the exciton density, the cavity finesse and the polariton dispersion, all of which can be tuned by device design.

3.4 Summary

In this chapter the basic concepts of BEC have been reviewed. In 2D structures, BEC is absent in the thermodynamic limit but can occur in a finite system. Although polariton condensates are not strictly speaking BECs, it has been established that polaritons can undergo similar phase transitions, that give rise to phenomena associated with BEC, like

superfluidity and vortices. The most significant application of polaritons, the polariton laser has been reviewed and compared to conventional lasing devices. The next chapter presents the samples utilised for the experiments described in this thesis.

Chapter 4

Samples

The last few years have seen GaAs increasingly used in the fabrication of semiconductor microcavities. Thanks to a wealth of knowledge regarding not only its physical properties but also its technological manipulation GaAs is often cited as the ideal material for the study of microcavity polaritons. Nevertheless, major drawbacks include the need for operation in cryogenic temperatures and the quick loss of strong coupling required for polariton condensation. The very short polariton lifetime (few picoseconds) also limits thermalisation with the lattice host which is only possible in the high density regime where pair polariton scattering mechanisms become active. Unfortunately strong coupling in materials like GaAs is quickly lost due to exciton screening (Chapter 3.2). This explains why polariton condensation has been observed in CdTe [21] and GaN [22] but only very recently reported in GaAs [25, 76, 93].

All of the samples discussed in this research are GaAs based microcavities. One is a bare microcavity with no active material, used to investigate the photonic properties of the optical spin Hall effect (Chapter 5). The remaining two exhibit polariton lasing in the nonlinear strong coupling regime and were used to explore the nonlinear optical properties of polariton condensates (Chapter 6-8).

4.1 Sample 1 - bare photonic cavity

The sample used in this study was provided by Prof. Wolfgang Langbein (Cardiff University). Grown by molecular beam epitaxy, it consists of a 2λ GaAs cavity with two

AlAs/GaAs distributed Bragg reflectors in 27 (top) and 24 (bottom) pairs respectively. The cavity does not include any active material and thus does not exhibit any strong coupling phenomena. However, the confined cavity mode has a very narrow linewidth of ∼10 μeV yielding a lifetime of ∼30 ps. The calculated Q factor is of the order of 10ˆ6. The cavity resonance at normal incidence is centered around 1.46 eV, however it appears only at temperatures below 100 K, as it needs to be tuned into the transparent region of GaAs, approximately 30meV below the 1s excitonic resonance. The reflectivity spectrum, calculated via the transfer matrix technique is shown in Figure 4.1.

A slight, unintentional detuning variation across the sample, between the cavity mode and the centre of the stopband, is created due to the fabrication technique that was followed. However, for this experiment, excitation under different detuning conditions was not necessary.

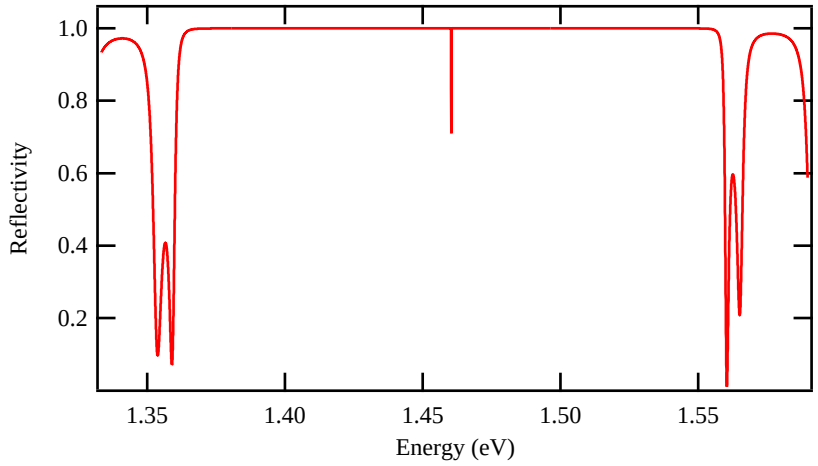

FIGURE 4.1: Calculated low temperature reflectivity calculations for Sample 1.

4.2 Sample 2 - planar GaAs microcavity

The sample used in this study was provided by Jacqueline Bloch (LPN-CNRS, Paris). It was grown by molecular beam epitaxy and consists of a λ/2 AlAs cavity of 2 $Al_{0.2}Ga_{0.8}As$/AlAs distributed Bragg reflectors with 16 (top) and 20 (bottom) pairs respectively. Strong coupling is maintained by embedding a large number of QWs for a large Rabi splitting. It has been proven that insertion of QWs in the centre of the cavity as well as the Bragg

mirrors successfully ensures as large a contribution as possible from the electromagnetic field to the coupling [94]. For this sample, three sets of four quantum wells of 7 nm width have been inserted in the centre and at the first antinodes of the electromagnetic field in each Bragg mirror [Figure 4.2]. In this sample, coupling occurs between the

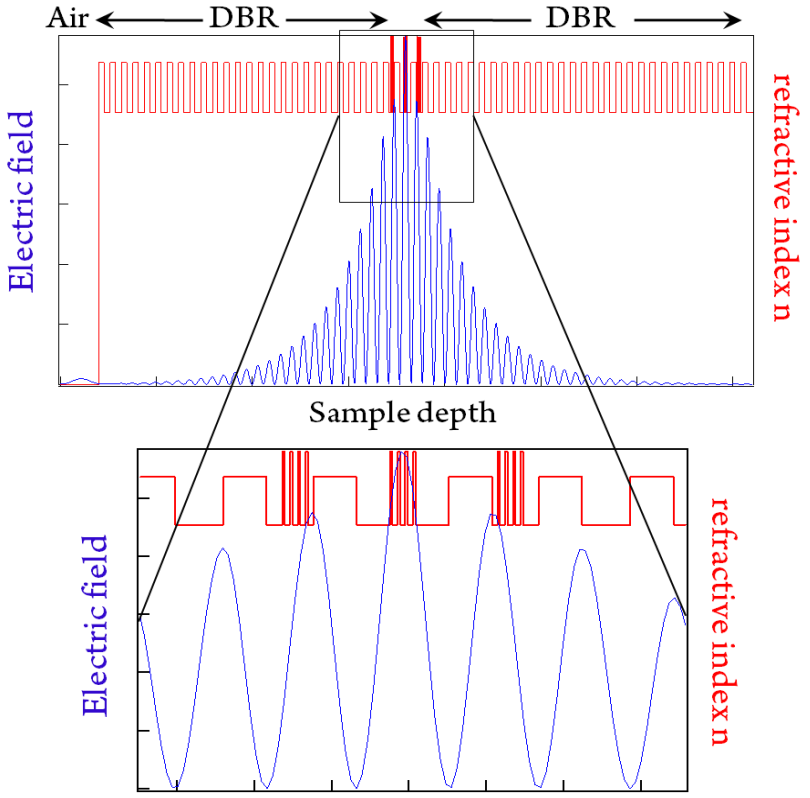

FIGURE 4.2: Schematic of the sample design, including the refractive index changes between the layers as well as the electric field inside the cavity. The quantum wells coincide with the centre and two side antinodes of the electromagnetic field.

cavity mode and both the light- and heavy-hole excitons. This leads to the formation of three polariton branches; lower (LP), middle (MP) and upper (UP). Calculated energy dispersions of the three branches as well as the cavity and two exciton resonances are shown in Figure 4.3. A wedge in the structure allows fine tuning of the energy difference between the cavity and the excitons' energy, for probing different detuning conditions (δ). Energy dispersions of the three polaritons branches as a function of the position of the excitation spot on the sample are plotted in Figure 4.4, along with the cavity and exciton resonances (Data provided by Esther Wertz from LPN-CNRS). The quality factor in this cavity is of the order of a few thousand. The structure only achieves photon lasing under non-resonant continuous wave excitation [77].

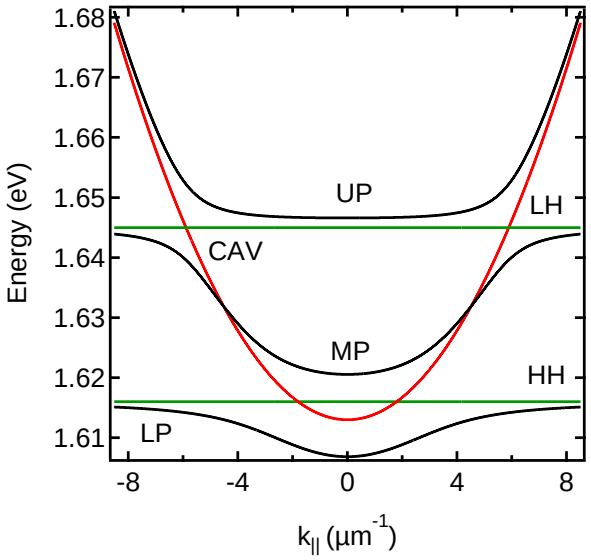

FIGURE 4.3: Energy dispersions of the cavity (red), light- and heavy- hole excitons (green), and the three polariton modes (lower, middle and upper in black) versus wavevector $k_{||}$ for samples 2 and 3.

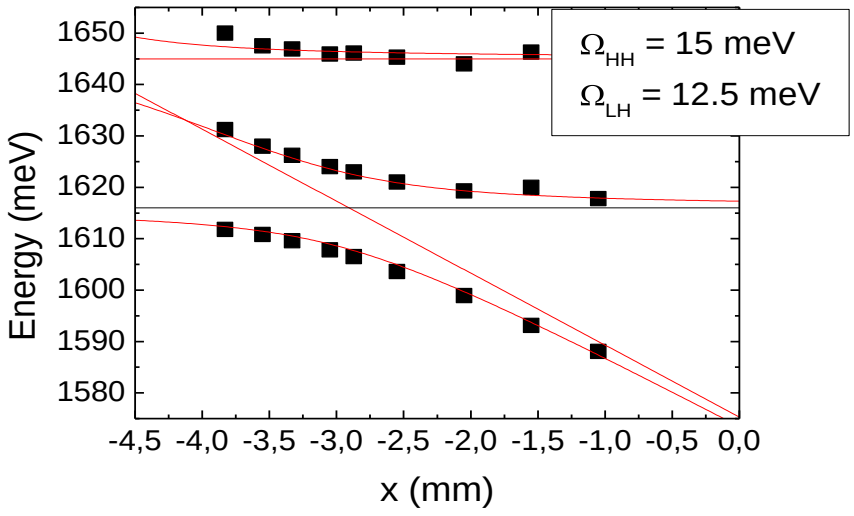

FIGURE 4.4: Energy dispersions of the three polariton modes *vs.* position on the sample for Sample 2.

4.3 Sample 3 - etched to micropillars

Sample 3, provided again by Jacqueline Bloch (LPN-CNRS, Paris) was grown by molecular beam epitaxy, consists of a $\lambda/2$ $Ga_{0.05}Al_{0.95}As$ cavity sandwiched by two $Ga_{0.05}Al_{0.95}As$ / $Ga_{0.8}Al_{0.2}As$ Bragg mirrors with 26 and 30 pairs in the top and bottom mirrors, respectively [27]. The reflectivity spectrum of the cavity is shown in Figure 4.5. Three sets of four 7 nm GaAs QWs are inserted at the antinodes of the electromagnetic field; one set at the centre of the cavity and the others at the first antinode in each mirror, similarly to sample 2. A wedge in the layer thickness allows continuous tuning of the cavity mode energy with respect to the QW exciton energy, thus changing the detuning. The quality factor of the planar sample, prior to etching, exceeds 12000. Square and circular micropillars of 2-20 μm side sizes and diameters respectively, were designed along the wafer using electron beam lithography and etched by reactive ion etching [Figure 4.6a [95]].

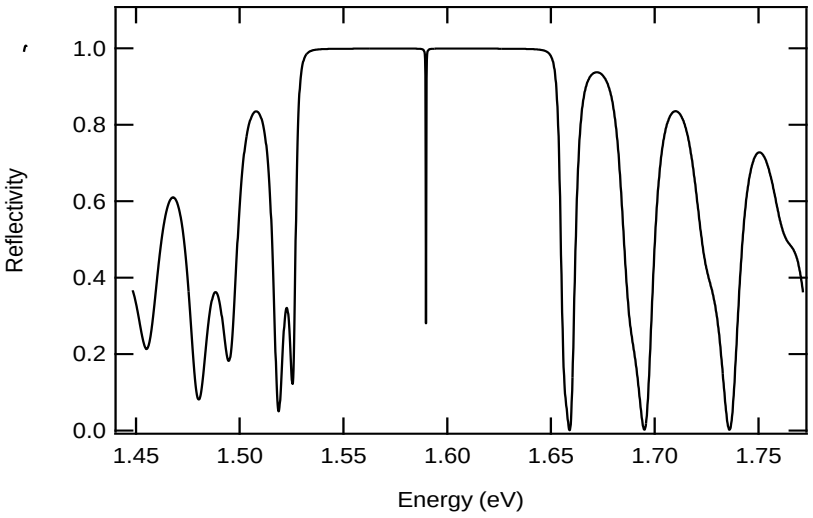

FIGURE 4.5: Reflectivity spectrum of Sample 3.

Previous work suggests that spatial confinement of polaritons would have an effect on thermalisation and subsequently polariton condensation. Confinement allows design and shaping of their optical properties. Zero-dimensional cavities confine polaritons along all spatial directions. This can occur by laterally patterning a planar microcavity in the shape of micropillars [96, 97]. Apart from the vertical confinement due by the Bragg mirrors, photons are also laterally confined by the refractive index contrast between the

air and the semiconductor material. The lateral confinement forms a sequence of discrete energy states determined predominantly by the size and shape of the pillars [98]. In the strong coupling regime, polaritons arise from the mixing between each of these 0D photon modes and the QW excitons [99] [Figure 4.6b [95]]

The broken translational symmetry of photon modes removes the restriction of momentum conservation from polariton-polariton scattering. The latter allows for efficient polariton relaxation, removing the relaxation bottleneck that impedes thermalisation and polariton condensation [19, 20, 77, 100], usually encountered in planar microcavities. As a result, polariton condensation in micropillars is much more efficient than in 2D planar structures. Under nonresonant optical excitation, relaxation from the exciton reservoir to the polariton states in the linear regime is predominantly driven by exciton-exciton scattering, while pair polariton scattering contributes to relaxation between the discrete polariton states. The interplay of exciton-exciton and pair polariton scattering defines which of the polariton states will first reach an occupancy of one and thus drive the system in the nonlinear regime where polariton condensation dominates the dynamics. Other processes including polariton parametric scattering have also been observed [28, 101].

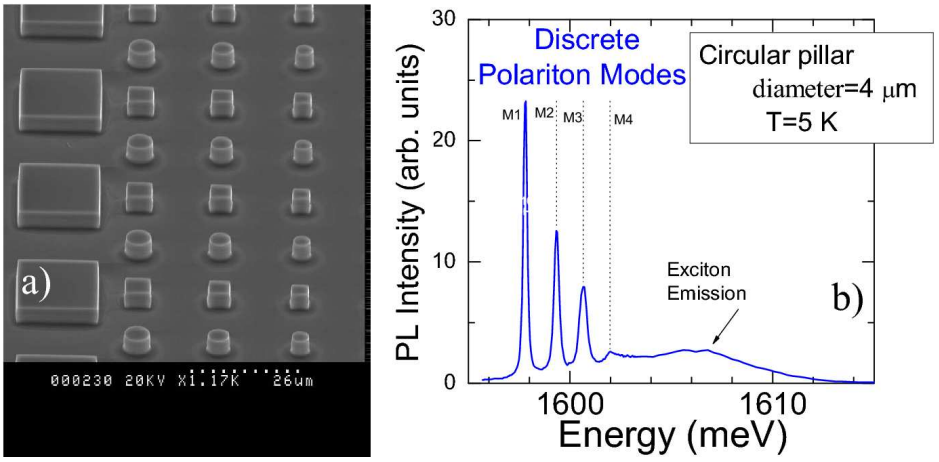

FIGURE 4.6: (a) Scanning electron micrograph showing a micropillar array. (b) Photoluminescence spectrum of a 4 μm diameter micropillar. Discrete polariton modes are clearly resolved. The wide band feature is attributed to uncoupled exciton emission [95].

Chapter 5

All optical spin Hall effect

The realisation of technologies that utilise the spin of particles requires electrically controllable spin dependent transport processes. For this emerging field of spin-electronics, or spintronics, the generation and manipulation of spin currents is perceived as one of the most remarkable and desired effects. Dyakonov and Perel [102] were the first to predict the possibility of the generation of a spin current perpendicular to the charge current flow. Originating from the spin orbit interaction, coupling between charge and spin currents leads to the accumulation of currents with opposite spin on opposite sides of the charge carrying semiconductor. Similarities with the classical Hall effect [103], where a Lorentzian force on the moving charges results in a charge imbalance, led Hirsch [104] to coin the term 'spin Hall effect' to describe the phenomenon. The spin imbalance observed in the spin Hall effect and the resulting spin current is due to either spin dependent elastic scattering (extrinsic spin Hall effect) [104] or the band structure (intrinsic spin Hall effect) [105]. Experimentally, it has been demonstrated with electrons acting as spin carriers in GaAs systems [106–108].

The optical analogue however has been easier to observe in semiconductor microcavities [30, 109, 110] since polaritons do not undergo the same rapid dephasing that suppresses the spin Hall effect in pure electronic systems. The optical spin Hall effect (OSHE) was demonstrated by the generation of spin polarised currents of polaritons in real- and momentum- space upon optical excitation. The effect has been attributed to the polaritons' mixed photonic and excitonic character, i.e. the polarization splitting of the cavity modes [111] and the spin orbit interaction [112] respectively.

Initially predicted by Kavokin *et al.* [113], the optical spin Hall effect (OSHE) in a polariton microcavity was described in terms of the pseudospin formalism, by the precession of the pseudospin vector $\boldsymbol{S}$ around an effective magnetic field $\boldsymbol{\Omega}$ induced by the longitudinal-transverse (LT) splitting of polaritons. In this scheme, the LT splitting consists of the combined effect of the polarisation splitting of transverse electric and transverse magnetic optical modes (TE–TM splitting) of the cavity and the spin orbit interaction. The resulting spin separation arises from the combined effect of the effective magnetic field $\boldsymbol{\Omega}$ and the Rayleigh scattering of the polaritons with disorder in the system. States whose pseudospin is parallel to the effective magnetic field vector do not experience any pseudospin precession. Upon linear excitation, carriers scattered along the four quadrants of the circle will experience a pseudospin precession, in opposite directons for two oppposite scattering angles.

This chapter focuses on the experimental generation of anisotropic polarisation flux in a bare cavity and a classical interpretation of the observed dynamics. By measuring the circular polarisation degree of scattered cavity photons versus the scattering angle the same anisotropy in polarisation in real- and momentum-space occurs. In contrast to the strongly coupled microcavities, the physical mechanism behind the OSHE is explained with classical physics where cavity photons act as spin carriers. The pseudospin formalism is valid only as a mathematical tool, but it proves very useful in providing quantitative results. It follows that the TE–TM splitting between the transverse electric and transverse magnetic cavity modes is sufficient to generate the effect, rendering the excitonic contribution unnecessary. The observed effect is therefore a complete optical analogue of the spin Hall effect, the *all-optical spin Hall effect*.

5.1 TE–TM splitting

The TE–TM splitting for an incidence angle $\phi > 0$ arises from the difference in phase shifts and penetrations of the optical modes into the Bragg mirrors for the two polarisations (Figure 5.1). Its magnitude is determined by the energy difference δ, between the cavity mode frequency ω_c and that of the centre of the stop band ω, i.e. the detuning $\delta = \omega_c - \omega$. For a cavity with refractive index n_c and width L_c, the angle dependent

TE–TM splitting of the cavity mode is given from the relation [42]

$$\omega^{TE}(\phi) - \omega^{TM}(\phi) = \frac{L_c L_{DBR}}{(L_c + L_{DBR})^2} \frac{2\cos\phi_{eff}\sin\phi_{eff}}{1 - 2\sin^2\phi_{eff}} \delta = \Delta_{TE-TM} \tag{5.1}$$

where L_{DBR} is the penetration length into the DBRs, given by Equation 2.12 and $\phi_{eff} \approx arcsin\frac{n_0}{n_c}sin\phi_0$. Its quadratic dependence on the incidence angle (equivalent to the in-plane k-vector) is shown in Figure 5.2, derived using the properties of the empty GaAs cavity under investigation[1].

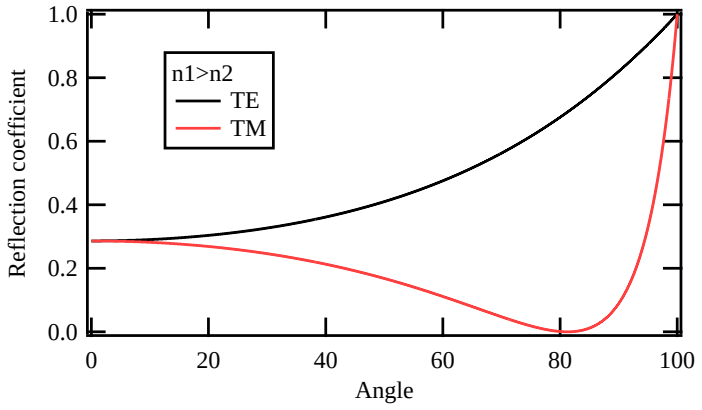

FIGURE 5.1: Propagation of TE and TM polarized light between two media of different refractive indices n_1 and n_2.

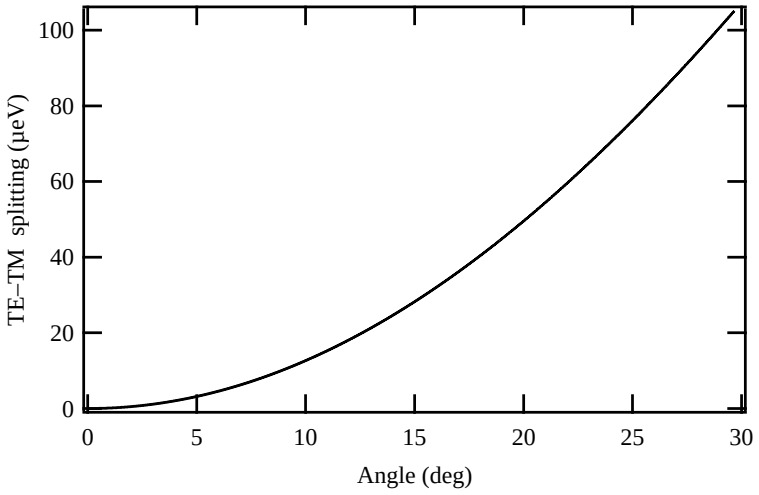

FIGURE 5.2: TE–TM splitting dependence of the bare photonic cavity with increasing angle. The range of angles that was investigated is shown.

[1]The values used in the formula are L_{DBR}=585 nm, L_C=470 nm and δ = 2 meV (experimentally measured).

5.2 Process

Following the pseudospin formalism (Chapter 2.5.1), polariton propagation in microcavities can be described by the following Hamiltonian:

$$\boldsymbol{H} = \frac{\hbar^2 k^2}{2m^*} + \hbar\boldsymbol{\sigma} \cdot \boldsymbol{\Omega} \tag{5.2}$$

where m^* is the polariton effective mass and $\boldsymbol{\sigma}$ is the Pauli matrix vector. The effective magnetic field, $\boldsymbol{\Omega}$, lies in the plane of the cavity. Its magnitude is proportional to the TE–TM splitting with $\Omega = \frac{\Delta_{TE-TM}}{\hbar}$ and its direction along the x- and y- axis depends on the polar angle θ of the photon in-plane wavevector, $\boldsymbol{k} = (k_x, k_y)$ in momentum-space:

$$\Omega_x = \Omega\cos 2\theta \tag{5.3}$$

$$\Omega_y = \Omega\sin 2\theta \tag{5.4}$$

The evolution of the pseudospin wavevector depends on the orientation of $\boldsymbol{\Omega}$ (Figure 5.3). When an initial cavity photon is created with a given k and linear polarisation state (TE or TM) its pseudospin (black arrows) is unaffected by $\boldsymbol{\Omega}$ (green arrows) when they both are parallel to each other. Rayleigh scattering with disorder redistributes the cavity photons around an elastic circle in reciprocal space. As the modulus of the in-plane wavevector is conserved during the scattering act, several different momentum directions are created that retain their initial pseudospin directions (Figure 5.3a). The pseudospin vector is no longer parallel to $\boldsymbol{\Omega}$ leading to its precession. Consequently, precession takes place in opposite directions for two opposite scattering angles allowing for different spin currents to develop in different quadrants of the elastic circle (Figure 5.3b). The evolution of the pseudospin in reciprocal space is described by the following equation,

$$\frac{\partial \boldsymbol{S}}{\partial t} = \boldsymbol{S} \wedge \boldsymbol{\Omega}(\boldsymbol{k}) + \frac{\boldsymbol{S_c}}{\tau_1} - \frac{\boldsymbol{S}}{\tau} \tag{5.5}$$

where the first term is related to the effective magnetic field induced precession. The second term describes the photon flux due to the Rayleigh scattering with time-constant τ_1. The final term accounts for the finite photon lifetime τ.

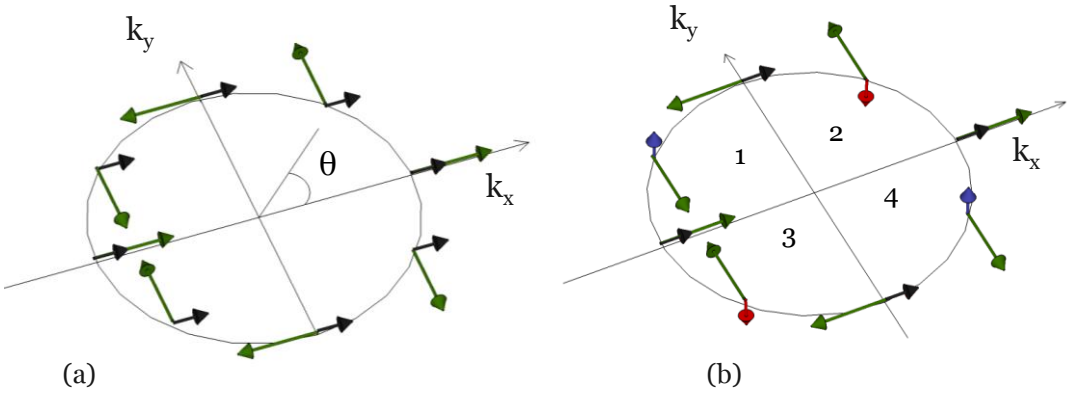

FIGURE 5.3: The direction of the effective magnetic field (green arrows) is dependent on the direction of the in-plane wavevector k in momentum space. (a) The initially linear polarised pseudospin (black arrows) after the Rayleigh scattering act. (b) The initially linear polarised pseudospin (black arrows) rotates until it becomes σ^+ (blue arrows) or σ^- (red arrows) circularly polarised depending on the orientation of the effective magnetic field. The result is a separation of spin-up and spin-down polarized cavity photons in different quadrants of the elastic circle

In the limit of weak scattering (each photon is scattered at most once during its lifetime), the circular degree of polarization on the elastic circle may be expressed as:

$$\rho_c(\theta) = \frac{\mid \Omega(k) \mid \tau \sin 2\theta}{1 + \mid \Omega(k) \mid^2 \tau^2} \tag{5.6}$$

Owing to ballistic propagation of the cavity photons, the spin separation on the elastic circle leads to spin separation in real space. In the frame moving with a photon, the equation of motion of the pseudospin may be written in the form:

$$\frac{d\boldsymbol{S}}{dt} = \boldsymbol{S} \wedge \boldsymbol{\Omega}(\boldsymbol{k}) - \frac{\boldsymbol{S}}{\tau} \tag{5.7}$$

Here, the time is connected with the spatial coordinate in the polar system (r, θ) through the transformation $t = r/v_g$ where v_g is the group velocity of photons and the initial condition is $S(t = 0) = S_0$. Solving the equation of motion, the circular polarization degree is derived as a function of space coordinate:

$$\rho_c(r, \theta) = \sin 2\theta \sin \frac{\Omega \cdot r}{v_g} \tag{5.8}$$

and thus photon spin currents are formed.

5.3 Experimental Procedure

5.3.1 Oblique incidence illumination

A detailed description of the sample used can be found in Chapter 4.1. Due to a high Q factor, the cavity mode dispersion (Figure 5.4) has a very narrow linewidth of 10 μeV and a corresponding cavity photon lifetime of 30 ps. The sample is illuminated at an angle of incidence using a continuous wave Ti:Sapphire laser ($\leq$ 2.5 meV linewidth). The linear polarisation of the incident beam is adjusted to either transverse magnetic or transverse electric by means of a half-wave plate, whose plate axis is rotated by 90 degrees.

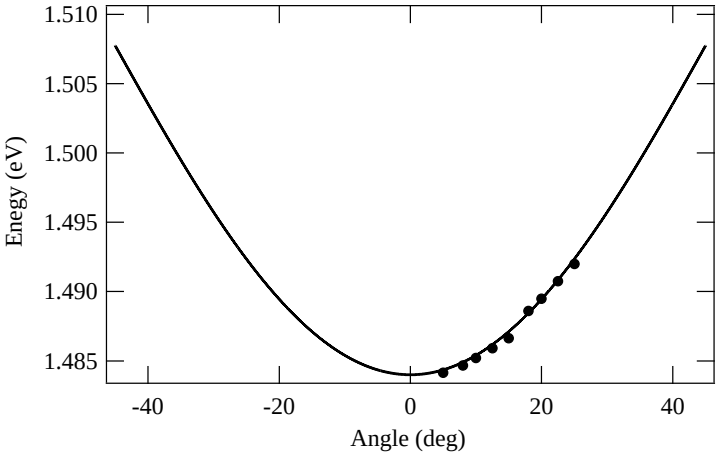

FIGURE 5.4: Calculated bare cavity mode dispersion vs angle. Filled circles correspond to experimental points.

The circular polarisation degree of scattered light from the elastic rings in momentum space populated incoherently by Rayleigh scattering is measured. This is achieved by tuning the angle of incidence ϕ of the beam to be resonant with $k \neq 0$ states of the cavity mode. The two setups shown in Figure 5.5 allow collection of the circular degrees of polarisation (σ^+ and σ^-) of the transmitted light in momentum- (a) and real-space (b). The detection paths were checked without the sample, but including all involved optics and the cryostat windows. No polarization changes were found in the transmitted signal and the error of the measurements was less than 5%. Images corresponding to the two degrees of collected circular polarization for an incident angle of 10° are shown in Figure 5.6. The calculated degree of circular polarization ρ_C (Equation 2.32) for various angles of incidence reveals a separation of spin-polarized photons in the empty

GaAs cavity in momentum-space (Figure 5.6). Rotation of the polarization plane of the exciting light results in inversion of the polarisation of the observed spin currents.

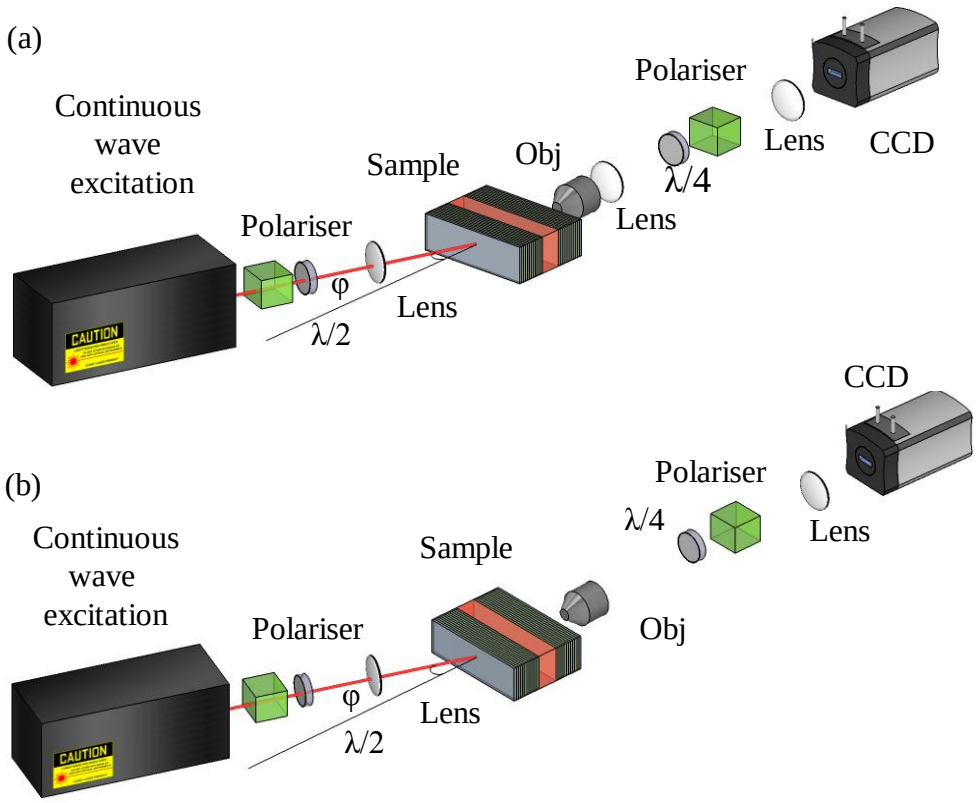

FIGURE 5.5: Experimental setup where two separate paths allow collection of transmission in (a) momentum space and (b) real space. The incident beam is always linearly polarised and occurs at an oblique angle θ.

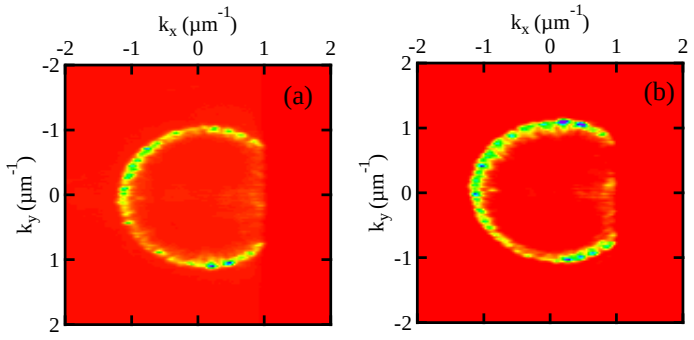

FIGURE 5.6: The (a) σ^+ and (b) σ^- detected component in momentum space upon oblique incidence illumination at 10°.

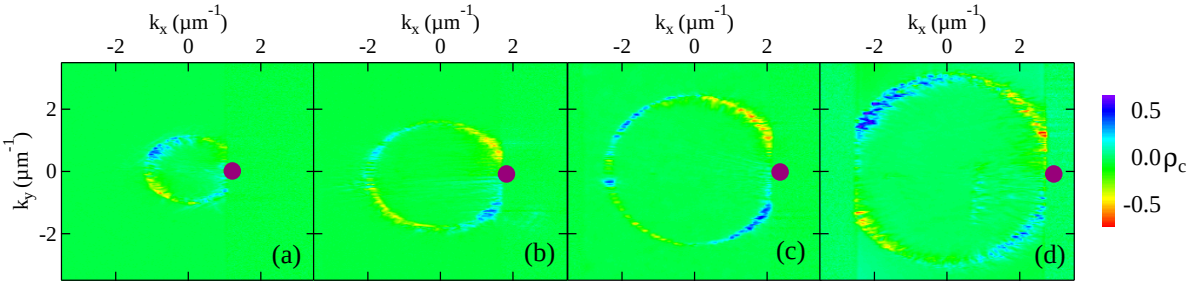

FIGURE 5.7: Observation of the all-optical spin Hall effect in reciprocal space under population of the elastic ring by Rayleigh scattering for angles of (a) 5° (b) 10° (c) 15° (d) 20°.

5.3.2 Normal incidence illumination

An alternative approach is implemented that allows direct population of states with the same k-vector magnitude and formation of a ring in momentum-space, by using a lens with a large numerical aperture (NA=0.4) [114]. The setup is shown in Figure 5.8. The incident beam energy determines the in-plane wavevector k on the ring and the polarization of the incoming photons is linear. The Rayleigh scattering process is still present but is not the primary mechanism behind the population of the ring in momentum space. The polarisation of photons across the elastic ring acquires different phase shifts as they propagate in various directions. Images of the total intensity as well as one of the two collected circular components in real space for illumination energy corresponding to 10° are shown in Figure 5.9. Figure 5.10 illustrates the generation of polarization flux in both momentum- (Figure 5.10a) and real (Figure 5.10b) space, upon llumination of the sample with energies resonant to the cavity mode with a large numerical aperture at four different TE- polarised pump energies. A four-fold symmetry is again apparent in each case. It can be seen in from the real space patterns of Figure 5.9 that the strong outer ring emission exists even in the raw data and is not a result of the data analysis. The discussion that follows in this section attrubutes this observation to interference between light propagating in the substrate and the cavity field. Rotating the incident beam to TM linear polarisation results in inversion of the generated polarisation flux (Figure 5.11).

Elastic rings imaged in momentum space have radii corresponding to the modulus of the wavevector that is resonant with the energy of the incident beam. The linewidth of the

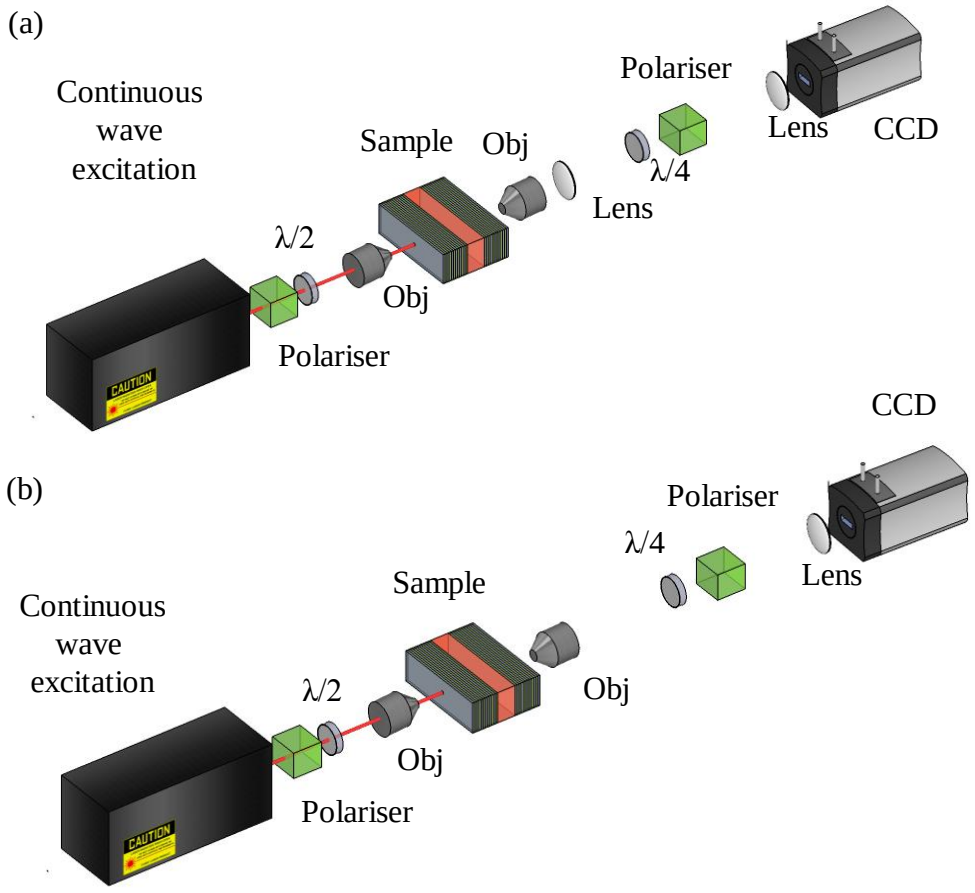

FIGURE 5.8: Experimental setup, where two separate paths allow collection of transmission in (a) momentum space and (b) real space. The incident beam is always linearly polarised and occurs at normal incidence.

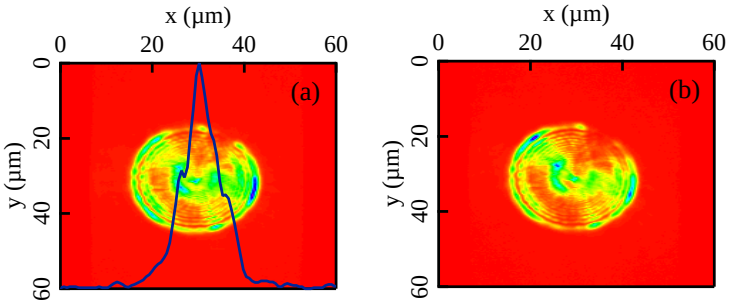

FIGURE 5.9: (a) Total intensity in real space for illumination energy corresponding to 10°, where the illumination beam profile is superimposed. The σ^+ detected component is shown in (b).

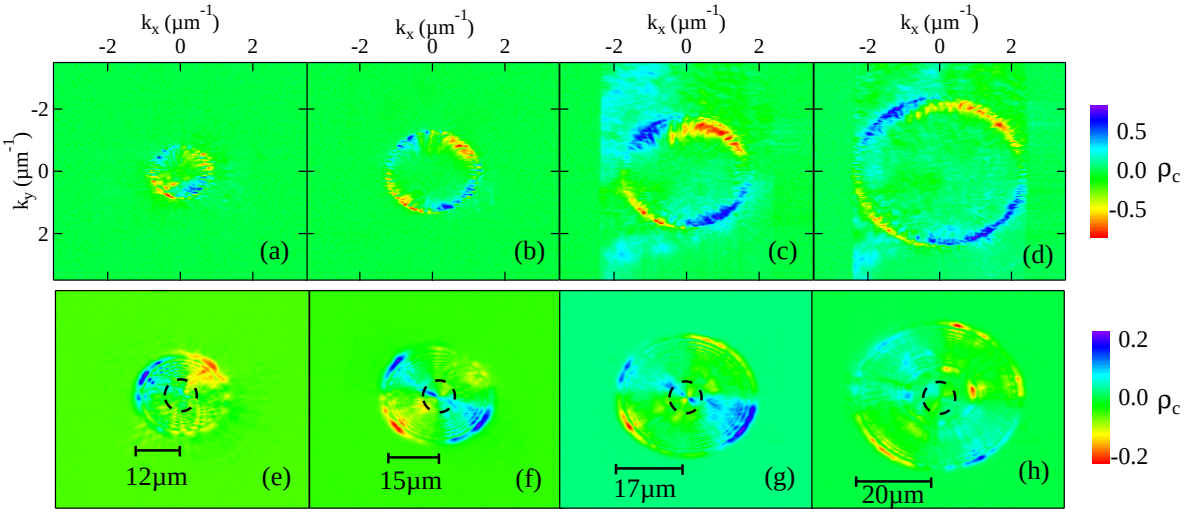

FIGURE 5.10: Spin-polarised rings in momentum space (a-d) resolved with Stokes parameter, ρ_c and corresponding real-space (e-h). The colour scale is linear in intensity. The incident beam is TE polarised at energies corresponding to (a, e) 5° (b, f) 10° (c, g) 15° (d, h) 20°

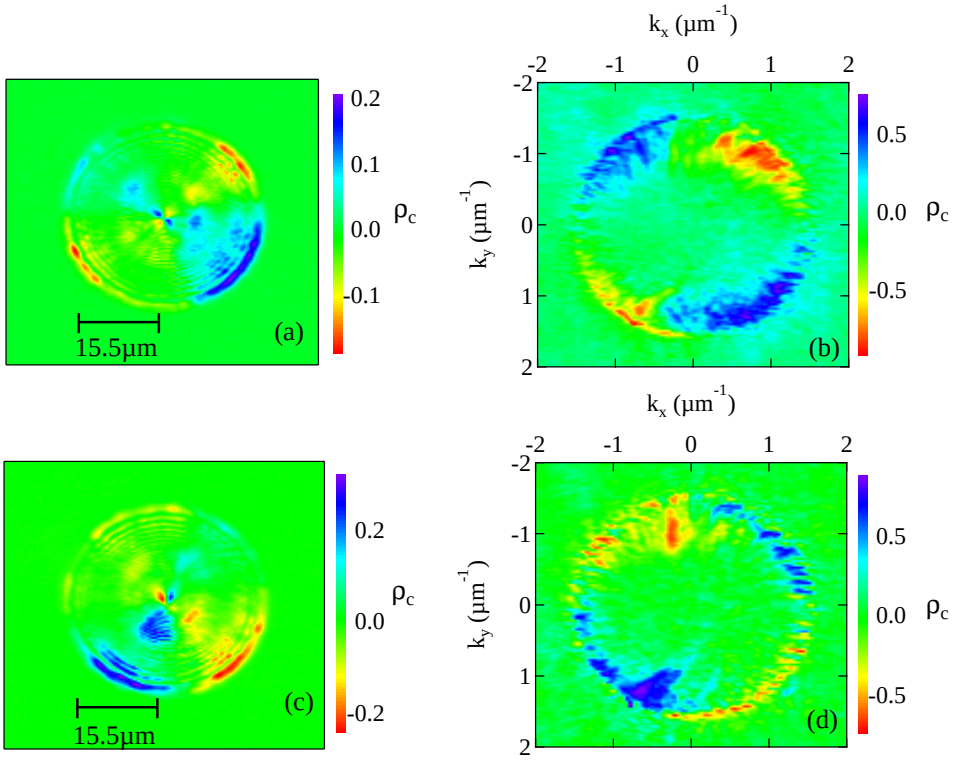

FIGURE 5.11: The measured degree of circular polarization under horizontal excitation in near (a) and far field (b). The resonant energy corresponds to an external angle of excitation of 12 degrees. The spin currents are inverted under vertical excitation in near (c) and far field (d).

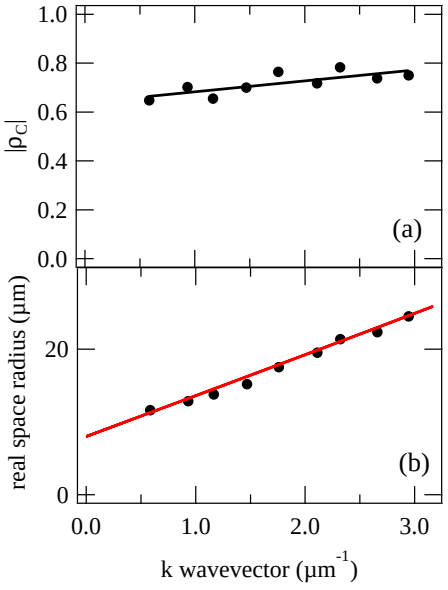

FIGURE 5.12: Evolution of (a) $|\rho_C|$ and (b) the distance of the ballistic propagation of photons in real space as the wavevector increases. The solid line in (a) is a guide to the eye and in (b) corresponds to theoretical calculations. The markers correspond to experimental data.

k-space rings is a constant with the linewidth of the incident beam. The numerical value of ρ_c is proportional to the incident beam energy and therefore the k wavevector of the particles, as shown in Figure 5.12a.

The real space images reveal an increase of the photons' ballistic propagation distance with increasing wavevector (Figure 5.12b). A simple model taking into account propagation of light in the substrate and interference with the cavity field can account for the real space intensity patterns, observed experimentally. As the rays escape from the cavity they propagate through the substrate, after multiple reflections on the sample surface. After the second reflection, only 10% of the initial intensity survives and it can be safely assumed that only the number of reflections N=1 or N=2 is allowed. Considering an angle of incidence ϕ and an angle of propagation in the substrate ψ, $n\sin\phi = \sin\psi$ and $k = \frac{2\pi}{\lambda}\sin\phi = k_0\sin\phi$, with λ the wavelength in vacuum. The ring radius, i.e. the distance after one reflection is given by

$$R = 2Nd\left[\left(\frac{k_0 n}{k}\right)^2 - 1\right]^{-1/2} + R_0 \tag{5.9}$$

where d is the substrate thickness and R_0 the excitation spotsize, using $Nd = 75$ μm

and $R_0 = 8$ μm. The model is valid for $v_g\tau = r > R$, as the intensities of the substrate and cavity fields must be comparable. Hence the choice of N=1 in the formula above. Experimental and theoretical results are shown in Figure 5.11b.

5.4 Theoretical modeling

Results from theoretical simulations using wave optics, performed by Tomáš Ostatnický (Charles University in Prague) are shown in Figure 5.13. The wavelength corresponding to the central frequency of the Bragg mirror stop-band is λ_B=834.691 nm. The cavity resonance has been deduced by numerical fitting of the position of the cavity mode peak in the spectral-resolved transmittance data and the corresponding wavelength is λ_B=835.91 nm. These two numbers give us the value of the detuning parameter δ=2 meV.

The cavity is considered to be a 2λ GaAs cavity with 24/27 pairs GaAs/AlAs Bragg mirrors grown on 20 μm thick GaAs substrate with anti-reflection coating. The incident light is considered to be a Gaussian beam of the following form in k-space:

$$E_{0x}(k) = \exp(\frac{-k^2}{\sigma^2}) \tag{5.10}$$

In the cylindrical coordinate system, the initial electric field intensity is decomposed to its TE and TM components:

$$E_{TE}(k,\phi) = E_{0x}(k)\sin(\phi) \tag{5.11}$$

$$E_{TM}(k,\phi) = E_{0x}(k)\cos(\phi) \tag{5.12}$$

The standard transfer matrix method is used to determine the TE and TM transmission coefficients $t_{TE,TM}(k)$ and backward transformation is performed towards the x-y coordinate system:

$$E_x(k,\phi) = E_{TM}(k,\phi)t_{TM}(k)\cos(\phi) + E_{TE}(k,\phi)t_{TE}(k)\sin(\phi) \tag{5.13}$$

$$E_y(k,\phi) = -E_{TM}(k,\phi)t_{TM}(k)\sin(\phi) + E_{TE}(k,\phi)t_{TE}(k)cos(\phi) \tag{5.14}$$

The transformation to the real space is done by means of the Fourier transform:

$$E_{x,y}(r,\phi) = \int_0^{2\pi} d\theta \int_0^{\infty} kE_{x,y}(k,\theta)\exp(ikr(\cos\theta\cos\phi + \sin\theta\sin\phi))dk \tag{5.15}$$

The intensities of circular components are calculated in the form $I_{\sigma_+,\sigma_-} =\mid E_x \pm E_y \mid^2$ and the corresponding circular degree of polarization is calculated from Equation 2.32.

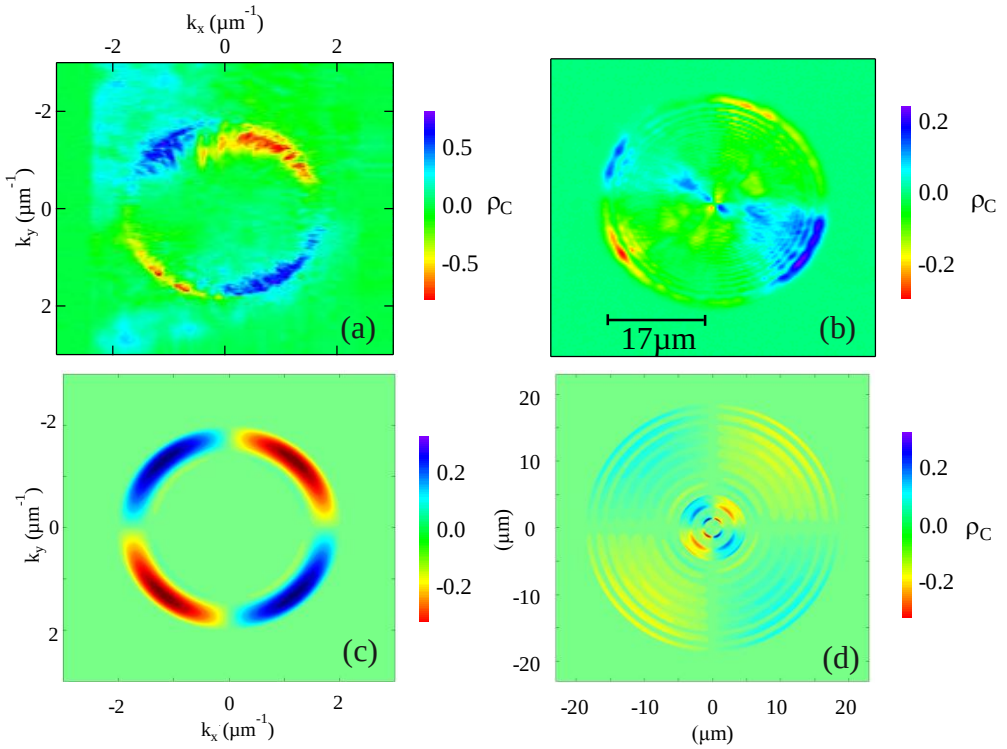

FIGURE 5.13: Far- (a) and near-field (b) Stokes parameters calculated for TE polarised excitation at 1.48663eV equivalent to 15 degrees. Theoretical calculations for the same conditions are given in (c,d).

5.5 Discussion

As explained in Chapter 5.2, the pseudospin vector rotates with a certain period around the polarization sphere, switching between linearly and circularly polarized states within the lifetime of the carriers. If the precession occurred for a full period, it would lead to zero degree of polarization in momentum space, due to averaging and polarization oscillations between the two circular polarization components in real space. As the above effects are not observed, the findings suggest that the photon lifetime (30 ps) is at least half the rotation period of the pseudospin vector, which corresponds to an energy

difference of 70 μeV. Therefore, the TE–TM splitting of the cavity must be less than the above value. The theoretical calculations produce an upper limit of about 100 μeV for the angles investigated in this experiment (Figure 5.2).

Both experiments and theory reveal a larger degree of circular polarization then the maximum of 50% allowed by Equation 5.6. The pseudospin formalism applies to the polarization state of the photons inside the cavity but does not comprise the role of the Bragg mirrors and/ sample surfaces. TE–TM splitting occurs in reflection but also in transmission and therefore if a linear polarization is incident on a Bragg mirror, some elliptical polarization is possibly transmitted. Therefore photon tunneling through the mirrors can notably increase the degree of circular polarization which may then exceed 50%.

Exchanging the half- and quarter-wave plate to illuminate with circularly polarised light and resolve the linearly polarised transmission, yields similar observations. A four-fold spin carriers' symmetry in real and momentum space is achieved. This further confirms the linear optics' origin of the observed effect.

The observed effect retains therefore many similarities with the spin Hall effect, mainly the separation of spin polarisation flux. In our system however, the injected photons are polarised and undergo polarisation conserving Rayleigh scattering whereas in the case of the spin Hall effect carriers are initially unpolarized and gain some degree of polarisation, either through polarisation dependent scattering (extrinsic spin Hall effect) or due to an external field that affects the carriers' wavevector (intrinsic spin Hall effect). Our observations can be interpreted in a simplified way through wave retardation caused by the cavity. In our structure the TE–TM splitting provides an effective birefringence which depends on the in-plane momentum and polarisation of the incoming photon. As the linear polarized photons form a ring of the same energy in k-space, via Rayleigh scattering or direct illumination of the whole k-space, they propagate in different directions. The directional birefringence results in photons in different quadrants of the k-ring experiencing different phase shifts and hence exhibiting different polarization rotation. The presence of the TE–TM splitting between the two linear polarisations propagating in the cavity is therefore essential.

5.6 Conclusions

This chapter described the successful observation of the optical analogue of the spin Hall effect in a pure photonic cavity under side and normal incidence illumination. Photons scatter across the elastic circle and, due to the TE–TM splitting of the cavity mode, develop an anisotropic polarization flux in momentum- and real- space. Their behaviour can be qualitatively described by the pseudospin formalism originally applied to polaritons in a strongly coupled microcavity. A theoretical model based on wave optics is developed due to the pure photonic nature of the effect. The TE–TM splitting related photonic component has been decoupled from the exciton component and the findings suggest that the presence of any active material is not essential for the observation of the optical spin Hall effect in semiconductor microcavities.

Chapter 6

Polariton condensation in a planar microcavity

The possibility of high temperature Bose Einstein condensation (BEC) in the solid state offers an attractive alternative to ultracold atomic BEC. As mentioned in the introductory chapters of this thesis, the de Broglie wavelength of polaritons is several orders of magnitude larger than that of atoms, allowing in principle for BEC even at room temperature. However, unlike atoms, the polariton lifetime is limited by the photon cavity lifetime to a few picoseconds. Although the ultrashort lifetime prevents thermalisation with the host lattice, inter-particle interactions allow for rapid relaxation and formation of a macroscopically occupied ground state, usually referred to as a polariton condensate. Investigations in a CdTe microcavity demonstrated striking similarities of polariton condensation with non-equilibrium BEC [21, 24, 82]. The recent demonstration of an electrically pumped polariton diode in planar GaAs microcavities [90–92] has paved the way for an electrically injected BEC in solid state. Polariton condensation in a 2D GaAs structure under non-resonant excitation remained elusive at the time these experiments were carried out, even under optical pumping [27].

In this chapter, findings regarding the transient formation of ground-state polariton condensation in a 2D GaAs/AlAs semiconductor microcavity under non-resonant pulsed optical excitation are reported. A threshold in photoluminescence intensity is observed with increasing excitation density, while angularly resolved photoluminescence shows that polariton condensation occurs directly at the ground-state. Near field imaging of

the polariton photoluminescence reveals a spatial collapse of the emission on the photonic disorder of the microcavity with the onset of polariton condensation occurring at a polariton occupancy of approximately three. Far field imaging confirms that a transition from the weak- to the strong-coupling regime occurs at high excitation densities. The coherence of the emission in the weak coupling regime is significantly lower than in the strong coupling regime, allowing to observe the build-up of a macroscopic coherent polariton state in the time domain.

The sample described in chapter 4.2 is used for the studies described in this chapter. The sample is held in a wide-field of view cold-finger cryostat and all experiments are performed at 7 K. In a previous study, photon lasing was observed in the same structure under non-resonant continuous wave excitation [77]. The transition to the weak coupling regime and the absence of any non-linear polariton effects in the strong coupling regime under CW excitation could be attributed to sample heating. Here such issues are eliminated using 180 fs optical pulses at 730 nm focused down to a 40 μm diameter spot with the excitation at the first minima of the Bragg reflector.

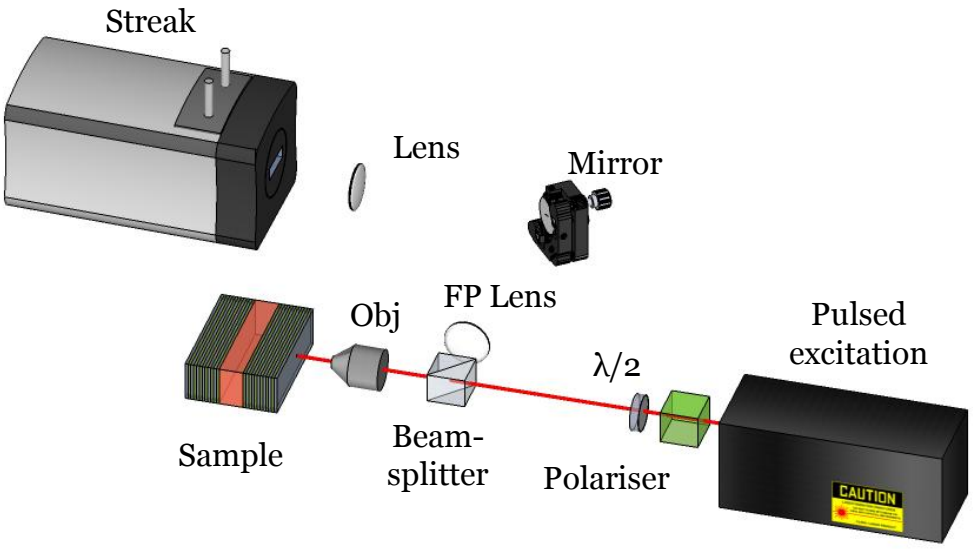

FIGURE 6.1: Experimental setup that allows for the collection of the Fourier plane and its imaging on a spectrometer, coupled with a streak camera. The sample is excited using pulsed excitation through a large aperture lens.

6.1 Setup

Energy dispersion curves are imaged using the reflection setup shown in Figure 6.1. A lens positioned on the emission Fourier plane images the momentum plane. For this reason, excitation and collection of the emission were realised through a lens with large numerical aperture. This technique offers directly information about the dispersion properties of the condensate (Equation 2.17). Simultaneous energy- and time-resolved photoluminescence measurements are taken using a 1200 grooves/mm grating in a 35 cm spectrometer coupled to a streak camera.

6.2 Experimental Results

Streak images of the emission at $k = 0$ can be seen on Figure 6.2. Images are taken at several pump powers, as annotated. The detuning used is -7 meV. Below threshold ($P_{th} =$ 6.5 mW), the observed time scales are of the order of nanoseconds, which reduce down to hundreds of picoseconds as the excitation power increases (Figure 6.2a-c). Polariton emission starts blueshifting at threshold (Figure 6.2d), where the decay times become much shorter as well. At about $6P_{th}$ (Figure 6.2g), the shape of the polariton relaxation changes, allowing for the observation of a linewidth increase. At later times, however, the linewidth becomes sharper. The above suggests that strong coupling is lost at early times but sufficient reduction of the number of carriers as they leak out from the cavity allows for the strong coupling to occur at later times. The transition between the two regimes is thoroughly analysed in Chapter 6.3.

The excitation density dependence of the photoluminescence for the $k = 0$ state confirms the nonlinear increase of the photoluminescence intensity by 10^3 at threshold [Figure 6.3a], already visible in Figure 6.2. The blueshift of the emission energy with increasing excitation density is usually considered characteristic of the strong coupling regime and is interpreted as the result of repulsive polariton-polariton interactions [115]. Figure 6.3b shows the energy shift of the peak emission as a function of the excitation density, which gradually flattens but remains below the bare cavity mode. The emission linewidth gradually broadens before threshold; collapses at threshold and broadens again above threshold with increasing excitation density as shown in Figure 6.3c. The rapid narrowing of the linewidth at threshold is attributed to the increased coherence of the polariton

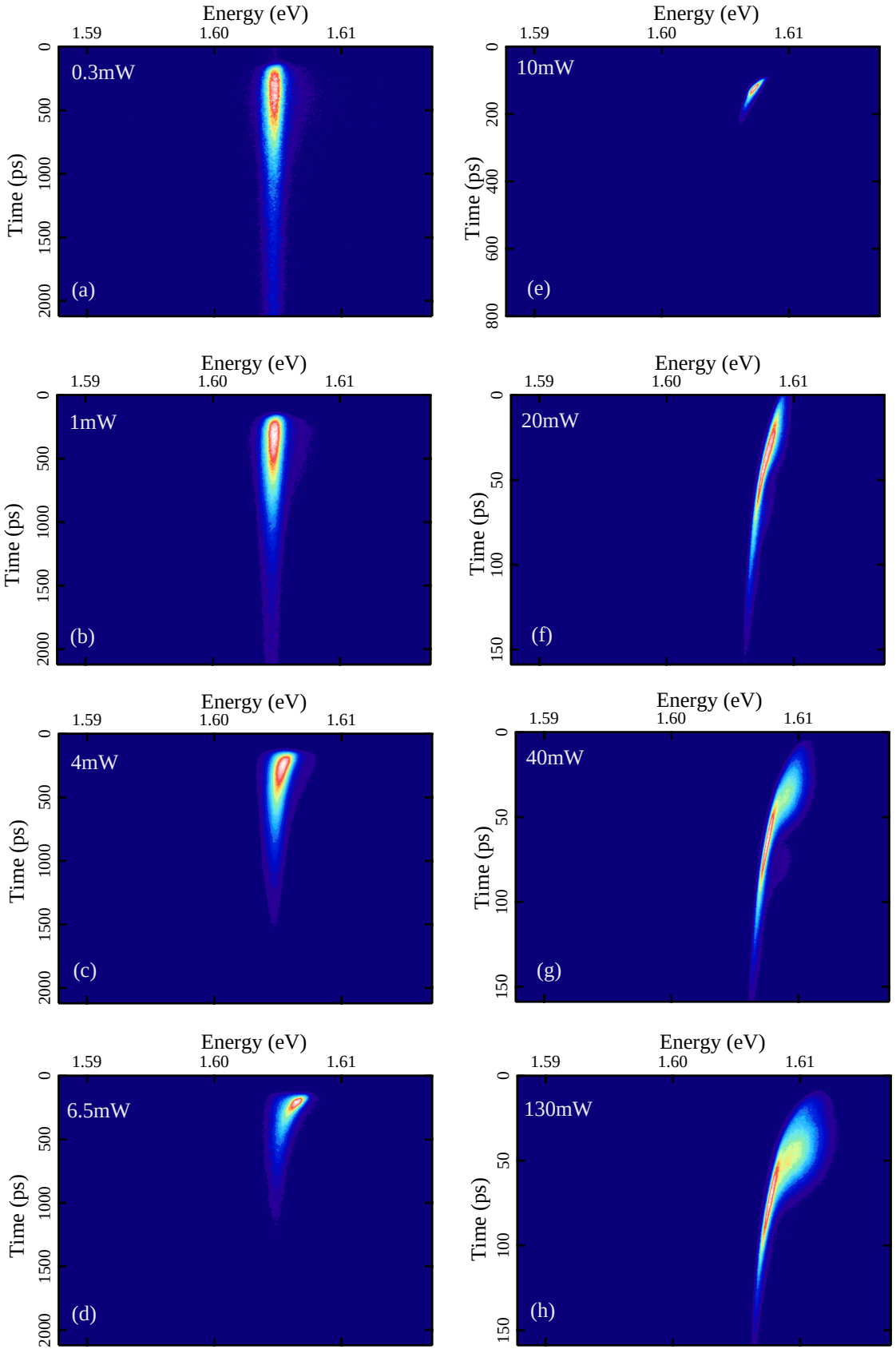

FIGURE 6.2: Time- and energy-resolved emission spectra for a -7 meV negative detuning for various indicated input powers.

condensate [9]. Further broadening above threshold is partially due to increased scattering within the condensate. This observation is congruent to previous reports in CdTe [116] and GaN microcavities [22]. However, as shown below, in the case of intermittent excitation time integrated photoluminescence measurements overestimate the linewidth of the emission due to the transient energy shift of the emissive states.

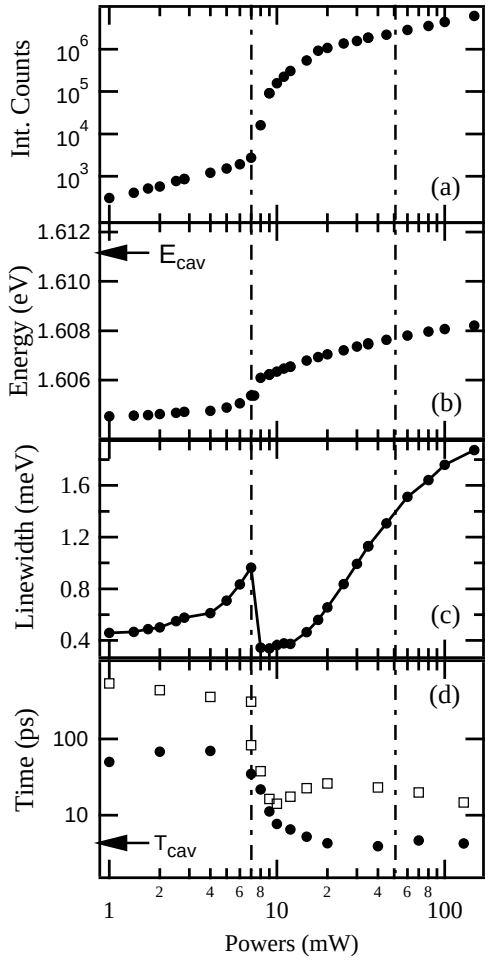

FIGURE 6.3: Power dependence of (a) the intensity, (b) the energy blueshift and (c) linewidth of the ground state emission as a function of the excitation power. (d) Rise (solid circles) and decay times (open squares) of the emission with increasing excitation power.

The build-up and decay of the emission at normal incidence is resolved using a streak camera with an overall resolution of 4 ps. Figure 6.3d shows the rise time of the build-up of the emission (solid circles) and the corresponding decay time (open squares) as a function of excitation density. Below threshold, the build-up ($\sim$ 90 ps) is driven by the relatively slow relaxation of polaritons at the ground-state through exciton-phonon

scattering and spontaneous exciton-exciton scattering that also dominate the photoluminescence decay dynamics [54, 58]. Above threshold stimulated scattering accelerates the build-up of the emission and the decay dynamics are now limited by the cavity lifetime (∼12 ps). Whereas the rise time follows a nearly monotonic dependence on the excitation density, it should be underlined that the decay time of the emission rapidly decreases above threshold nearing the cavity lifetime, while it increases for even higher excitation densities (open squares in Figure 6.3d). The above allows for the assumption that this is due to the depletion of the states in the exciton reservoir that feed the ground polariton state. At even higher excitation densities (to the right of the second vertical dashed line in Figure 6.3d), the decay time re-approaches the bare cavity lifetime but as shown in the following chapter, this trend is linked with the transition to the weak coupling regime.

The use of the grating was avoided while tracking the time dynamics presented in Figure 6.3d. The reason is that simultaneous use of spectral and time resolution, increases the resolution of the latter, therefore producing results that are not entirely accurate. Figure 6.4 provides a comparison between photoluminescence from the $k = 0$ state of the microcavity, pumped with 40 mW (Figure 6.2g), recorded (a) with and (b) without the use of the grating. A direct comparison between the profiles of the top panel is depicted in the bottom panel and underlines the difference between the two experimental configurations. The time scales of the polariton relaxation are quite fast and use of the grating doesn't offer the appropriate resolution for the measurements.

6.3 Transition from weak to strong coupling regime

As mentioned in chapter 6.2, the time resolved data indicates that the strong coupling is lost for input powers $P > P_{th}$. Below threshold the emission energy corresponds to the ground polariton state shown in Figure 6.5a. The horizontal dashed lines depict the bare cavity and heavy hole exciton energies. The photoluminescence decay extends to 1.5 ns and is dominated by the relaxation of polaritons through exciton-exciton and exciton-phonon scattering. The linewidth of the emission remains constant throughout the decay [Figure 6.5b]. At threshold the emission energy is initially blueshifted while remaining well below the bare cavity mode and then gradually red-shifts with decreasing polariton population [Figure 6.5c]. It is also evident that the linewidth of the emission at threshold is almost half the linewidth below threshold and remains virtually unchanged

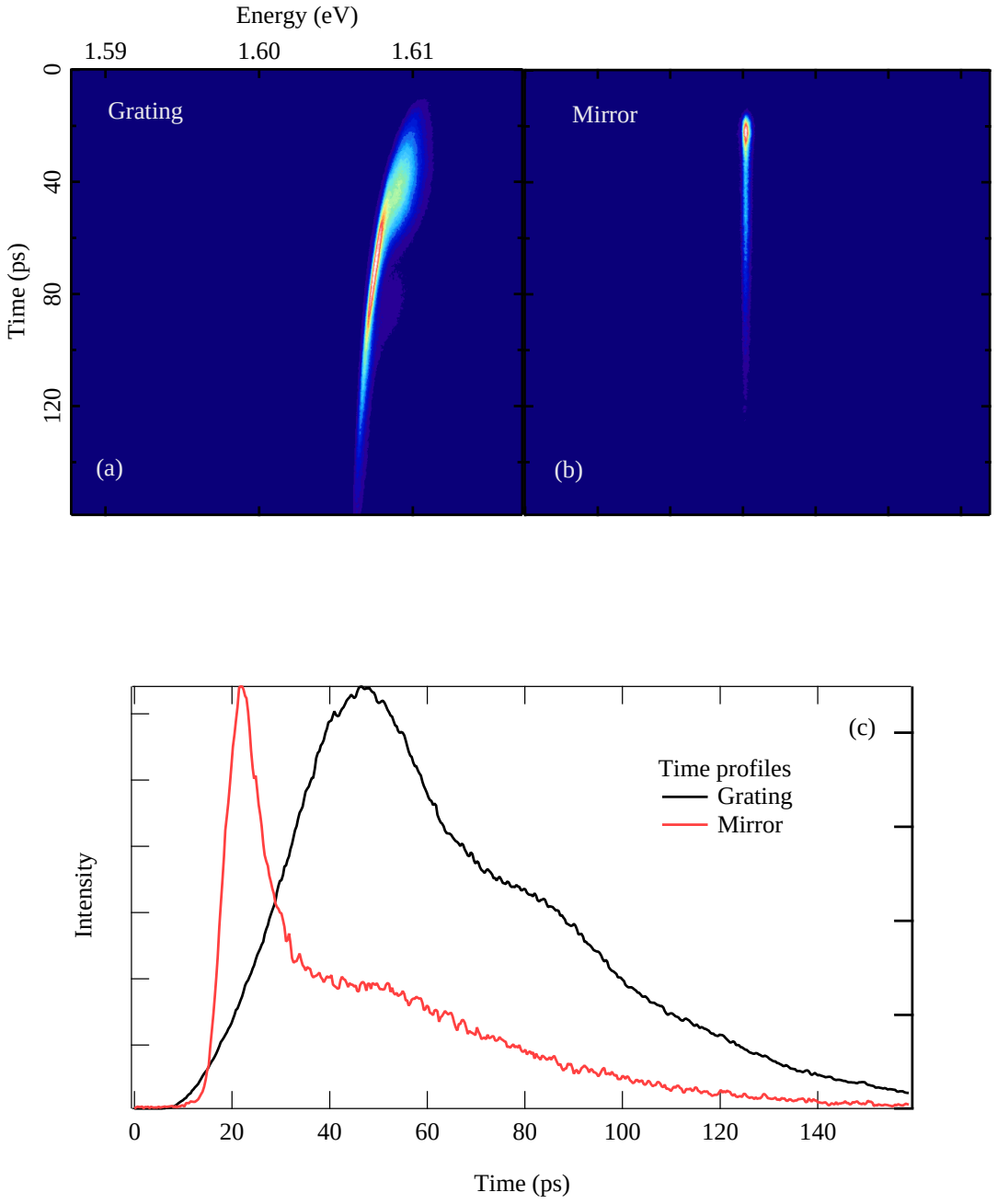

FIGURE 6.4: Time resolved emission from the k=0 state at a -4 meV detuning, (a) with and (b) without the use of the grating for spectral resolution. A direct comparison of the two profiles can be seen in (c).

with time [Figure 6.5d]. The dynamic bandwidth of the streak camera does not allow for resolution of the residual emission when the polariton dynamics return transiently to the linear regime.

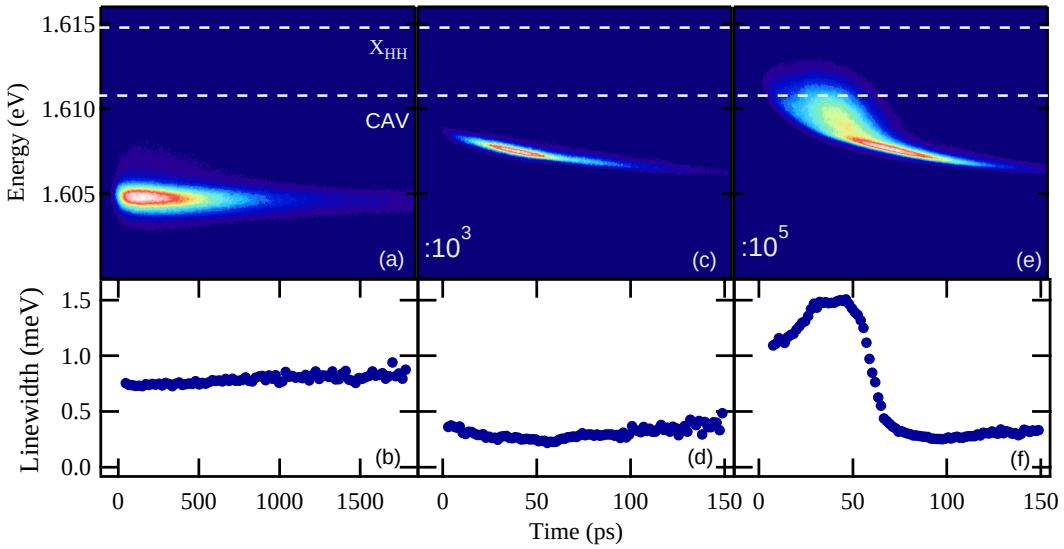

FIGURE 6.5: Time and spectrally resolved photoluminescence spectrum and the corresponding linewidth for excitations powers (a, b) below threshold, (c, d) at the nonlinear strong coupling regime and (e, f) at the weak coupling regime.

From the transient dynamics of the emission energy and the linewidth in the nonlinear regime it becomes apparent that integrated measurements of the photoluminescence under pulsed excitation produce only an upper estimate of the emission linewidth. This can also explain the broadening of the linewidth above threshold. Indeed, at short times shown earlier in Figure 6.3 the dynamic blueshift of the emission energy increases with increasing excitation density. However, the emission energy of the polariton condensate always relaxes to the ground state of the polariton dispersion in the linear regime. This results in an increased time integrated linewidth with increasing excitation density when the instantaneous linewidth remains almost unchanged [Figure 6.5d].

Evidence that the observed nonlinearities in semiconductor microcavities occur in the strong coupling regime is produced when a clear transition to the weak coupling regime can be demonstrated for high excitation densities. In this study, for excitation densities $6P_{th}$ (Figure 6.2g), an asymmetric spectral broadening of the emission is observed, on the high energy side of the polariton line. At an excitation density 20 times above threshold (Figure 6.2h) this feature can clearly be resolved both spectrally and in the time domain

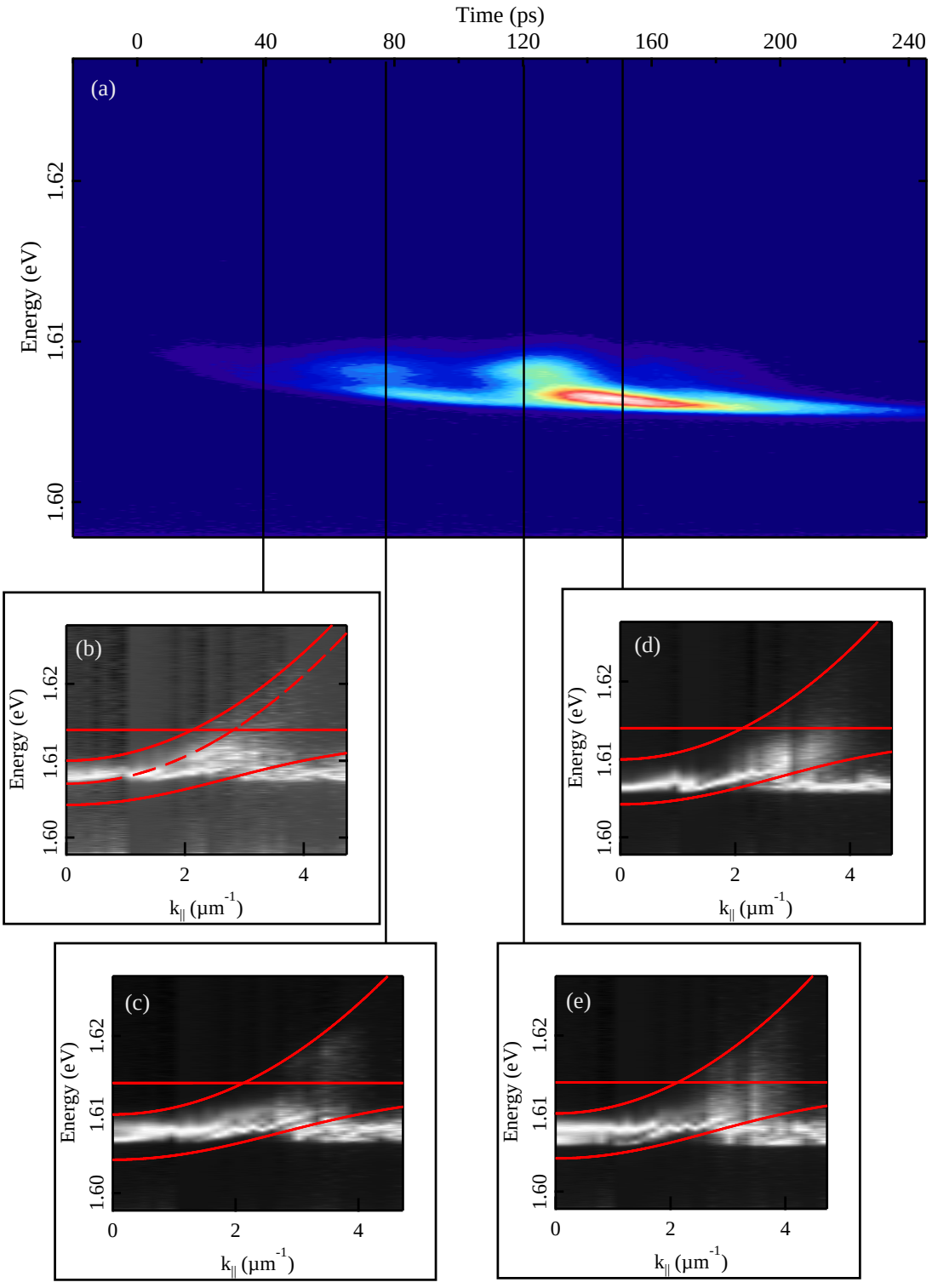

FIGURE 6.6: Energy and time resolved emission from the $k = 0$ state at a detuning of -4 meV (top panel (0-240 ps after excitation)). Dispersion images at the bottom panel correspond to times indicated by the black vertical lines. The red solid lines correspond to calculated exciton, cavity and lower polariton dispersions when the cavity operates at the linear strong coupling regime, i.e. below threshold. The dashed line in (b) corresponds to the redshifted cavity mode.

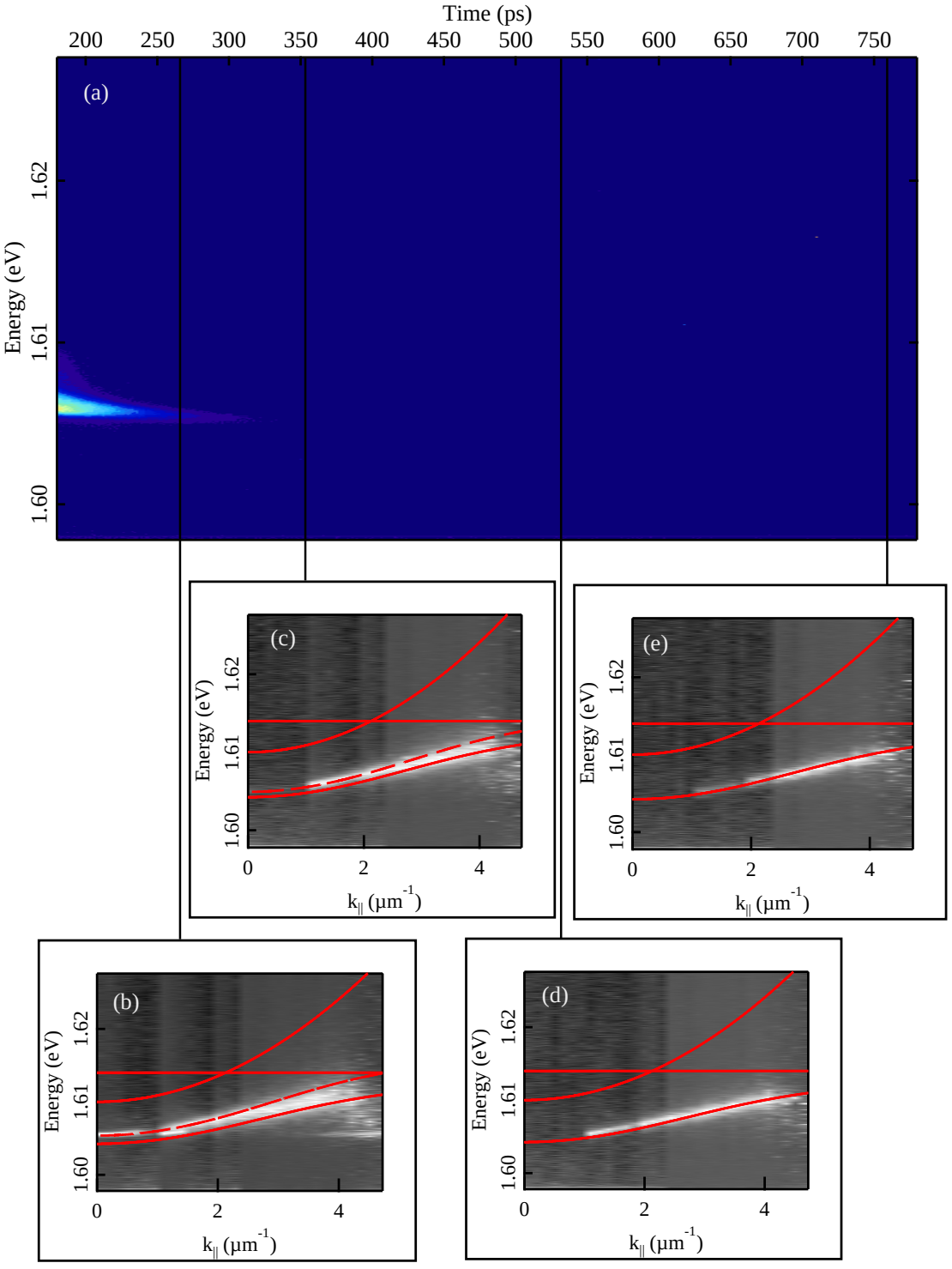

FIGURE 6.7: Energy and time resolved emission from the $k = 0$ state at a detuning of -4 meV (top panel (200-760 ps after excitation)). Dispersion images at the bottom panel correspond to times indicated for the black vertical lines. The red solid lines correspond to calculated exciton, cavity and lower polariton dispersions when the cavity operates at the linear strong coupling regime, i.e. below threshold.The dashed line in (b) corresponds to the blueshifted LPB.

as it precedes the emission from the ground polariton state [Figure 6.5e]. The transient nature of this measurement allows us to resolve the evolution of the photoluminescence from the weak coupling regime, where the emission approaches the bare cavity mode, directly into the nonlinear strong coupling regime. Interestingly, in the weak coupling regime the emission linewidth is broader than the linewidth in the nonlinear strong coupling regime. As the number of carriers in the quantum wells is reduced with time a clear transition to the nonlinear strong coupling regime is observed. While the two regimes overlap, the total emission linewidth is increased [Figure 6.5f]. With the system evolving exclusively into the nonlinear strong coupling regime the linewidth is narrowing to the value observed above threshold but at lower excitation densities.

Further evidence of the transition from the weak coupling to the strong coupling regime can be confirmed by studying in time the dynamic evolution of the whole LP branch. This is made possible by introducing a piezo-actuated mirror to the input of the time-resolved detection system described earlier. As previously mentioned, the setup tracks the LPB dispersion simply by focusing the Fourier plane onto the slit of the monochromator. Figures 6.6 and 6.7 present the LPB dispersion at different times as the polaritons leak out of the cavity and have their population reduced. For comparison, the time- and spectrally-resolved emission from $k = 0$ have been plotted in order to indicate the corresponding times for the dispersions presented at the lower panel of each figure. The red solid lines correspond to the linear strong coupling exciton, cavity and LPB dispersions. The intensity of each dispersion image is not constant throughout and therefore no information regarding the polariton populations across the branch can be extracted. Sufficient number of counts to allow for the observation of the shape of the curve at high k-states was implemented as this was the primary goal of this part of the experiment.

At early times, emission along the cavity mode can be detected as well as emission from states above the calculated LPB. High input powers and therefore increased carrier populations cause the polariton branch to blueshift in energy and the cavity mode to redshift (Figure 6.6b), due to a localized change of the refractive index [77]. The above explains the mismatch between the calculated and experimental dispersions. As carriers escape from the cavity strong coupling is resumed. The cavity mode is no longer present in the spectrum (Figure 6.7) but the LPB is still blueshifted (Figure 6.7b). Apart from the polariton dispersion, a flat line in energy can also be resolved at early times, due to the

photonic disorder, present in the cavity. At much later times, the cavity operates below threshold and the usual LPB dispersion is resumed, in accordance with the calculations.

6.4 Coherence

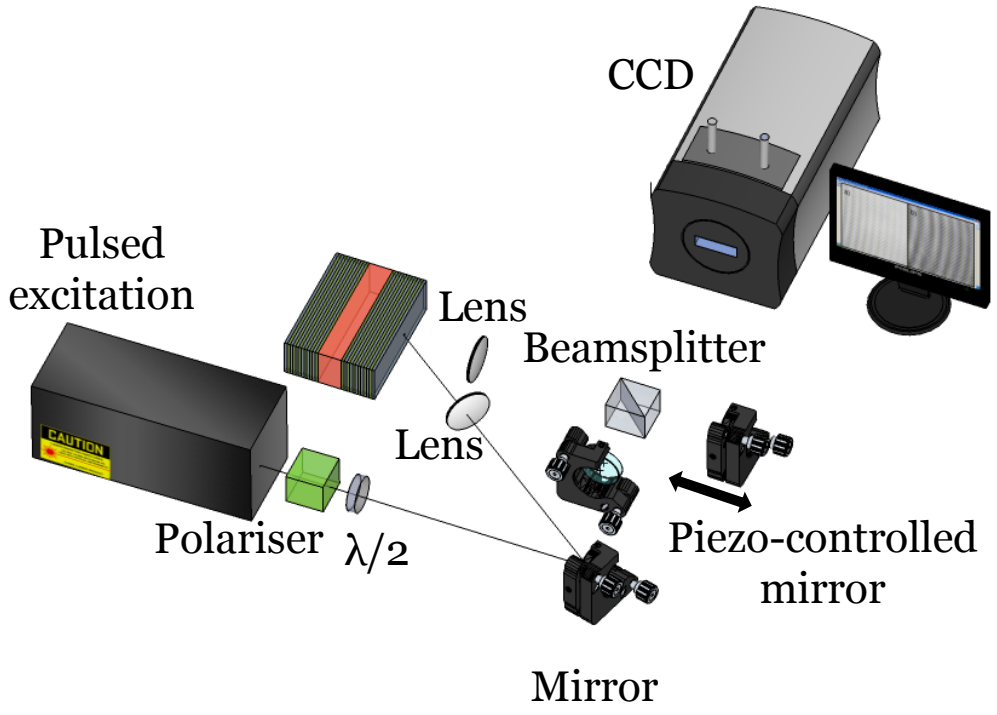

FIGURE 6.8: Michelson interferometer setup used for coherence measurememts.

The inference of coherence from the linewidth of the emissive states is further endorsed by directly measuring the first order coherence of the photoluminescence both in the weak and strong coupling regime. For that purpose a Michelson interferometer is built and the far field interference is recorded [83]. Figure 6.9 (a,b) show the interference fringes at zero time delay in the weak and the nonlinear strong coupling regime respectively. The corresponding contrasts, calculated using the following formula:

$$\frac{I_{max} - I_{max}}{2 \cdot I_{avg}}, \tag{6.1}$$

are 10% and 40% exemplifying the higher coherence of the emission from the ground polariton state. The decay time of the contrast of the observed fringes is longer in the ground polariton state (∼8 ps) in comparison to the weak coupling regime (∼4 ps)

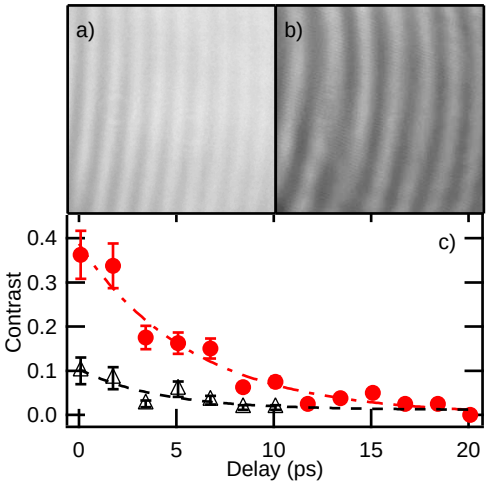

FIGURE 6.9: Far field interferograms of the ground state photoluminescence at zero time delay (a) in the weak coupling and (b) nonlinear strong coupling regime. The dependence of interference contrast on time delay for the weak (black open triangles) and strong coupling (red solids circles) is shown in (c).

[Figure 6.9c]. In the weak coupling regime the coherence lifetime is shown to be shorter than the cavity lifetime. In the nonlinear strong coupling regime the measurement of the coherence lifetime is mostly limited by the rapid transient of the emission energy.

6.5 Emission from k=0

The occurrence of nonlinear photoluminescence intensity either at the ground-state or at a higher wavevector of the polariton dispersion varies in the literature and it appears to depend strongly on the excitation conditions [75, 117]. As discussed in the following chapter, the excitation spotsize is of crucial importance regarding the k-wavevector state of the formed condensate. A tight spotsize leads to an accumulation of polaritons at higher k wavevectors allowing for the condensation to form a ring with radius k_c. A larger spotsize, which is the case here, allows for polaritons to relax towards the lowest energy state and for a $k = 0$ condensate.

The polariton dispersion is therefore mapped for the regimes below threshold, at threshold and in the weak coupling regime with the help of a goniometer that allows characterisation of the dispersion from normal incidence to 60°. Excitation occurs at an angle φ to the plane of the optical bench. Time integrated photoluminescence is recorded with

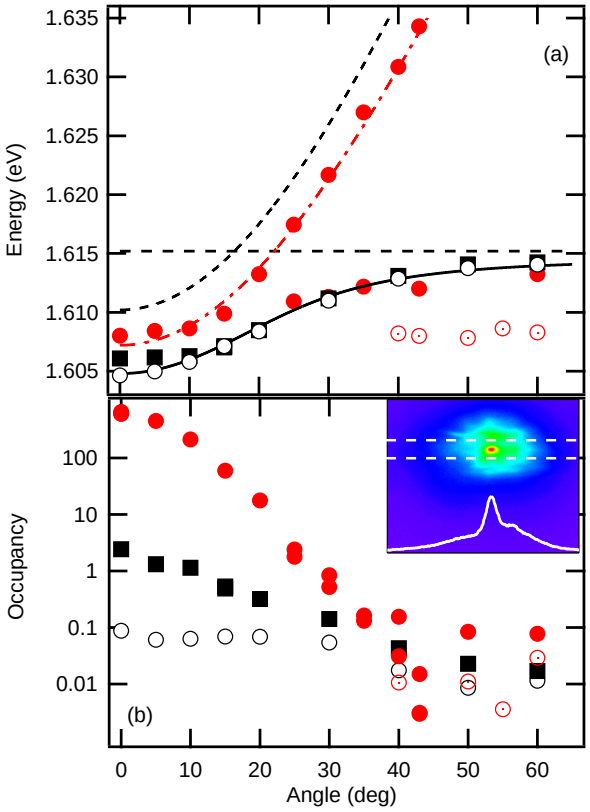

FIGURE 6.10: (a) Emission energy as a function of the detection angle for excitation powers (black open circles) below threshold, (black solid squares) at threshold and (red circles) at the weak coupling regime. The open red markers correspond to emission due to uncoupled excitons, observed at high angles. The black solid line correspond to the calculated lower polariton branch and the dashed black line to the heavy hole exciton and the cavity mode whereas the dashed red line to the cavity mode redshifted by 3 meV. (b) Polariton occupancy as a function of the detection angle. (Inset) Real space image at threshold and the corresponding intensity profile.

a 3° collection angle using a spectrometer coupled to a CCD camera. The polariton dispersion in the linear regime (below threshold) is plotted in Figure 6.10a (open black circles), where the solid line is the calculated LPB and the solid lines correspond to the uncoupled bare heavy hole exciton and cavity modes. At threshold, the polariton dispersion blueshifts to create a flat region between zero and 10°, while the polariton states at higher angles remain virtually unaffected [Figure 6.10a (solid squares)]. In an attempt to understand the angular broadening of the polariton dispersion near normal incidence the near field image of polariton photoluminescence at the excitation spot is resolved. Whereas the photoluminescence intensity below threshold follows the excitation intensity across the 40 μm spot, above threshold the data reveals a spatial collapse of the high intensity emission in a single spot of approximately ∼3 μm diameter [inset

in Figure 6.10b]. A cross section of the excitation spot shows that most of the excited area remains in the linear regime that explains the observation of the linear polariton dispersion at wide angles. Also the spatial localisation of the polariton condensate in a 3 µm spot results in a symmetric angular broadening

$$\Delta\vartheta = 2 \cdot tan\left(\frac{0.61 \cdot \lambda}{d}\right)^{-1} = 19°, \tag{6.2}$$

which can explain the observed flattening of the dispersion between zero and 10°. d and λ correspond to the spot diameter and the emission wavelength. From the intensity of the emission at threshold and the area of the emission the occupancy is calculated to be

$$n = \frac{I}{D \cdot f \cdot E \cdot N_{states}} \sim 3, \tag{6.3}$$

where I is the emitted intensity at threshold (190nW), D is the spotsize (7 x 10ˆ-8) , f is the repetition rate of the laser (80MHz), E is the polariton energy (1.59 eV) and N_{states} is the number of states for a collection angle of 5.7° (4.1 x 10ˆ-10 states/cm^2).

The occupancy for all other excitation densities is scaled using this value. Figure 6.10b shows the occupancy of polaritons as a function of detection angle below threshold, at threshold and in the weak coupling regime. Evidently, polariton nonlinearities spontaneously occur at the ground polariton state. In contrast to the observations in the strong coupling regime, in the weak coupling regime and for excitation densities 15 times above threshold the dispersion follows the bare cavity mode red-shifted by ∼3 meV due to refractive index changes [solid red circles in Figure 6.10a [118]. At high angles the bare cavity mode coexists with emission from other states red-shifted from the bare exciton mode [open red circles in Figure 6.10a], which is due to the photonic disorder, present in the sample.

In the next chapter, the role of the spotsize is investigated with regards to the k-wavevector of the formed condensate.

6.6 Role of the spotsize regarding the condensation

Much work in semiconductor microcavities has been devoted to proving the similarities between BEC and polariton condensates. While BEC generally occurs for the ground state, the first reports on polariton condensates in a CdTe microcavity showed condensation for $k > 0$ [24]. Condensation at the ground state was achieved upon adoption of a relatively large pump spot [21, 75, 82].

A theoretical proposal based on a mean field study of nonequilibrium condensates from M. Wouters *et al* [119], explained the peculiar connection between the spotsize and the properties of polariton condensates in real and momentum space. Experimental evidence regarding the spatial and spectral properties of polariton condensations are presented as a function of the pump spot size, in excellent agreement with the preceding theory.

6.6.1 Setup

The setup used (Figure 6.11) allows for collection of the Fourier plane and imaging of the far field emission as a function of pump power directly in the monochromator slit. An arrangement of lenses allows for the spatial modulation of the excitation spot size, whose FWHM varies from 0.8-25 μm.

6.6.2 Experimental Results

6.6.2.1 Large excitation spot

Integrated emission intensity from the LPB for various pump powers, using a spotsize with FWHM of 25 μm is shown for various pump powers in Figure 6.12(a-d). For excitations powers below threshold (Figure 6.12(a-b)), polaritons cannot relax efficiently to the bottom of their dispersion curve and accumulate at higher wavevector states. Phonon scattering is not efficient due to energy-momentum conservation rules, leading to the accumulation of polaritons in the bottleneck region. At threshold however, scattering towards the bottom of the trap becomes extremely efficient due to the onset of polariton-polariton scattering. The nonlinear increase of the photoluminescence intensity by 10^2 that occurs at threshold is evident with increasing excitation density (Figure 6.12e). The

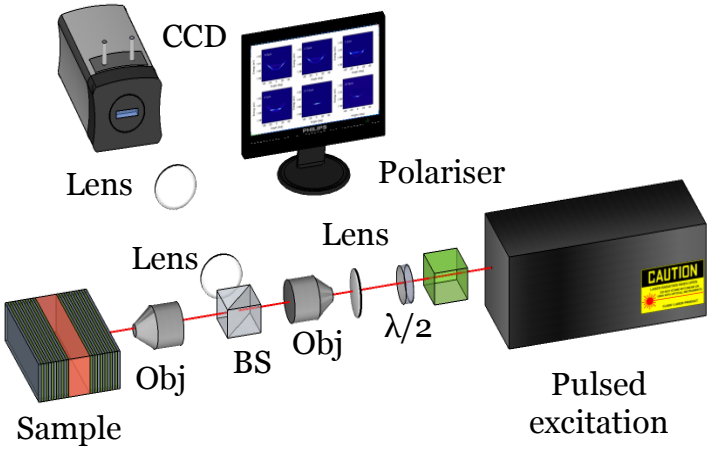

FIGURE 6.11: Experimental setup that allows for the collection of the Fourier plane and its imaging on a spectrometer. An arrangement of lenses allows for the spatial modulation of the excitation spotsize.

condensate forms at threshold as the polaritons collapse to a single state. Self interaction results in a blueshift of the photoluminescence by ∼2 meV [Figure 6.12b] and an increase in coherence causes a collapse of the linewidth (Figure 6.12f).

The blueshift of 2 meV that occurs at threshold is about 4 times the broadening of the ground state (Figure 6.12b); a result of the repulsive interactions of the polaritons. Given that [120]

$$E_{shift} = 4X_h E_b a_b^2 \frac{N}{S} \tag{6.4}$$

where E_b is the exciton binding energy, a_b the Bohr radius, X_h the excitonic fraction of the lower polariton branch, N the number of polaritons in the system and S the area of the sample, it follows that the polariton density at threshold equals 3x10ˆ11 cm^{-2}, which corresponds to 2.5x10ˆ10 excitons/cm^{-2} in each of the twelve quantum wells. The microcavity is still strongly coupled, even though the energy of the emission of the condensate is only 2 meV below the cavity mode. Time resolved dispersion emission data also supports this argument, since at threshold, the polariton dispersion can be clearly resolved without any sign of the cavity mode.

The full angular width of the emission is ∼20°, as shown in Figure 6.12g. This angular broadening comes as a result of spatial localization of the condensate [121]. Stronger

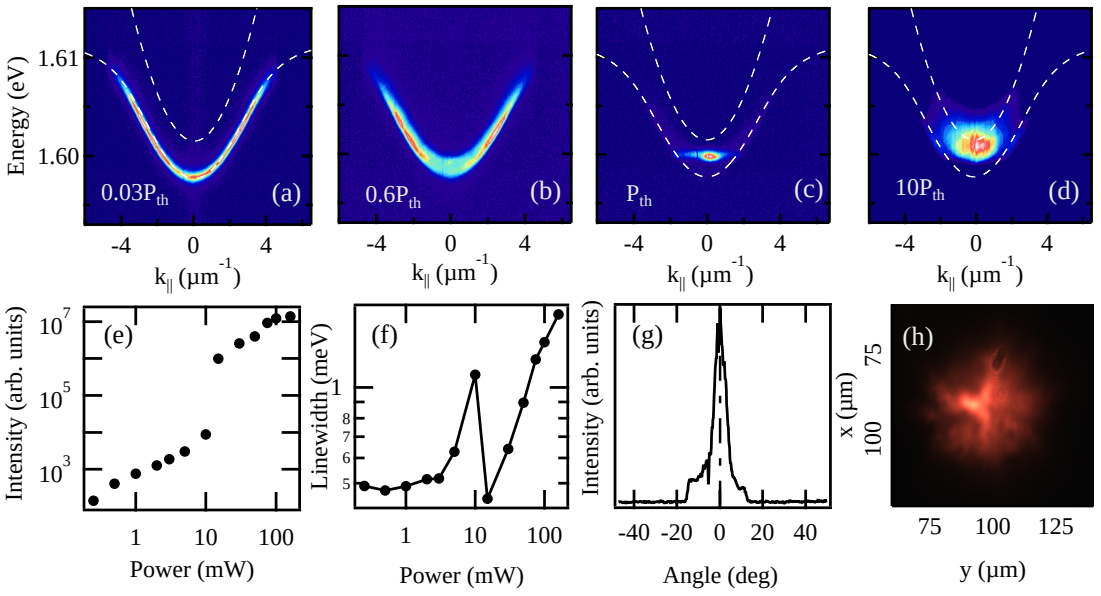

FIGURE 6.12: Lower polariton branch energy dispersions for -11 meV detuning conditions with a spotsize of 25 μm FWHM for pump powers (a-b) below, (c) at and (d) above threshold (P_{th}=15 mW). Doted white lines indicate the calculated dispersions for the lower polariton branch and the cavity mode. Power dependence of (e) the emission intensity and (f) the linewidth of the lower polariton ground state as a function of the excitation power. (g) Angular profile of the emission at 1.6 meV for $P = P_{th}$, corresponding to (c). (h) Near field polariton emission for $P = P_{th}$.

emission from certain smaller areas than the rest of the larger spot is evident in the real space profile, shown in Figure 6.12h. For much higher powers (Figure 6.12d), the strong coupling is lost and emission occurs in the weak coupling regime, a conclusion furthermore supported by time resolved emission data, where the cavity mode can be seen.

6.6.2.2 Small excitation spot

Integrated emission intensity from the LPB at various pump powers but for smaller excitation spots are shown in Figures 6.13 (4 μm FWHM) and 6.14 (0.8 μm FWHM). Below threshold excitations powers, polaritons accumulate at higher k states due to the bottleneck. Upon reaching the threshold for the nonlinear strong coupling regime, condensation occurs at these states, forming a ring with radius k_c. A weak pedestal is contained inside the polariton dispersion for $k < k_c$ but no emission outside the boundaries is observed. The polariton dispersion distorts further as the strong coupling

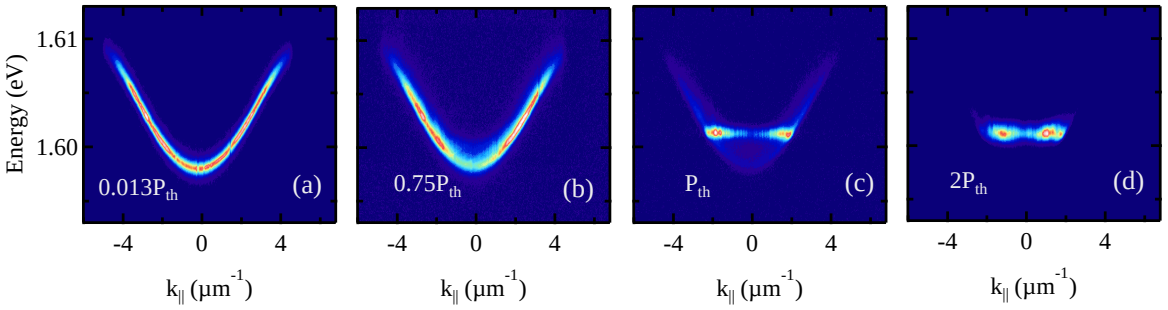

FIGURE 6.13: Lower polariton branch energy dispersions for -11 meV detuning conditions with a spotsize of 4 μm FWHM for pump powers (a-b) below, (c) at and (d) above threshold (P_{th}=75 mW).

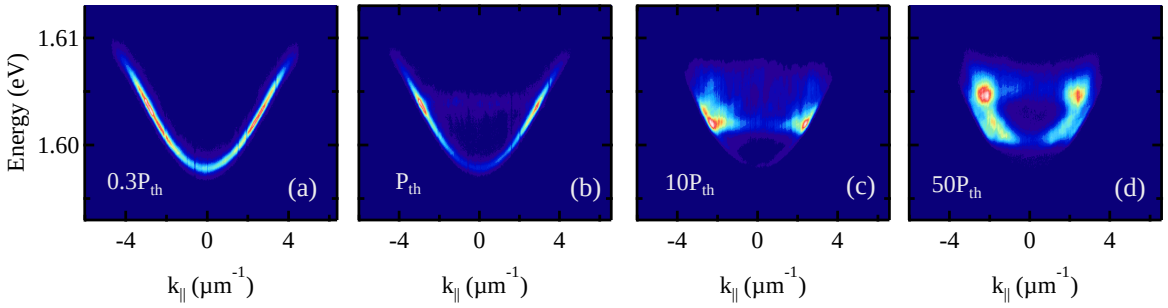

FIGURE 6.14: Lower polariton branch energy dispersions for -11 meV detuning conditions with a spotsize of 0.8 μm FWHM for pump powers (a-b) below, (c) at and (d) above threshold (P_{th}=30 mW).

is lost [Figure 6.13d, Figure 6.14c]. As these images present time integrated data under pulsed excitation, at high pump powers they include the transitions between all three regimes, hence both polariton and photon lasing can be observed in Figure 6.14d.

6.6.3 Theory

The energy dispersions of the polariton condensates at threshold for numerous excitation spot sizes are shown in Figure 6.15. For smaller spotsizes, condensation occurs at higher energies forming a ring in k-space. As the spotsize gets bigger, condensation moves towards the bottom of the trap, allowing for its formation at $k = 0$. These results are summarised in Figure 6.16, where the energy of the condensate has been plotted against the excitation spot size. The detuning is kept constant at -11 meV. The near field emission images under some of the conditions presented in Figure 6.15 are shown

in Figure 6.17. Emission for all cases occurs from small areas of diameter 2-5 µm (e.g. Figure 6.12h, Figure 6.17c).

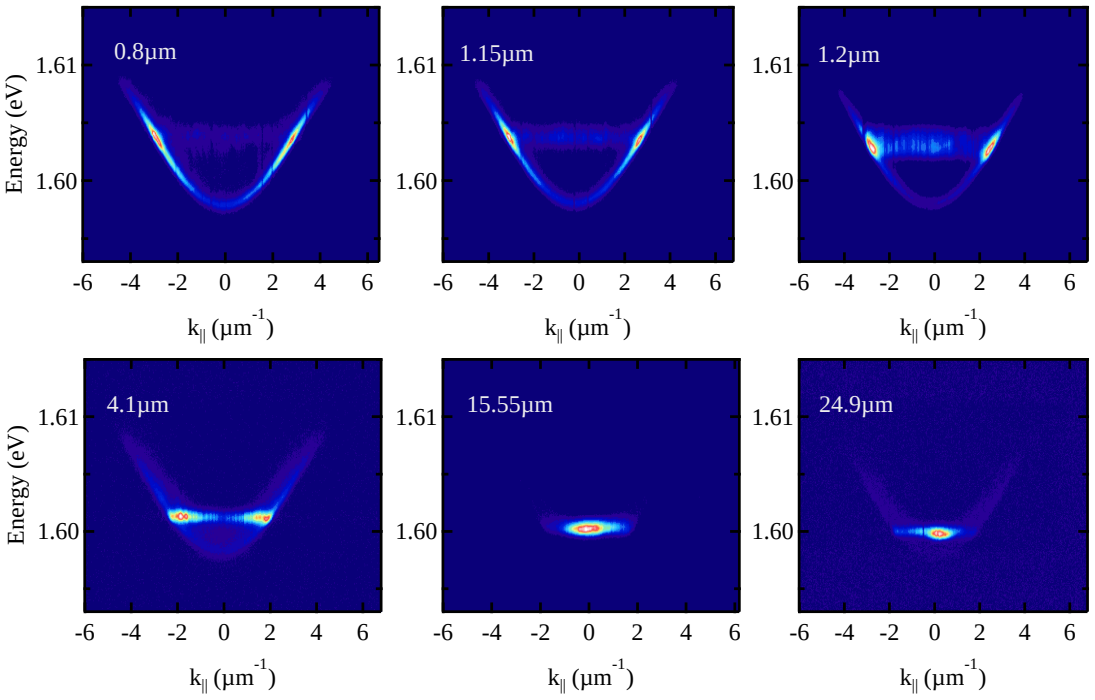

FIGURE 6.15: Lower polariton branch energy dispersions for -11 meV detuning conditions for various excitation spot sizes at $P = P_{th}$.

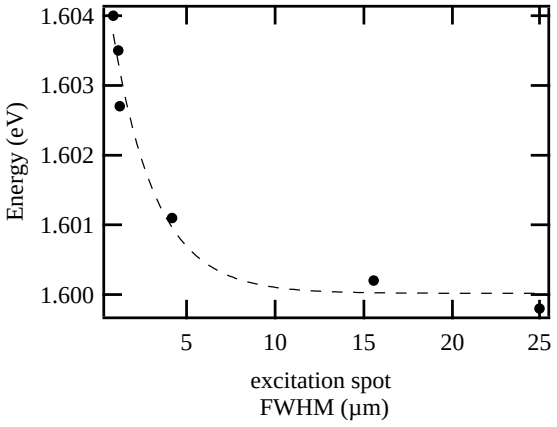

FIGURE 6.16: Energy of the polariton condensate at threshold *vs* the FWHM of the excitation spot size. The dashed line is a guide to the eye.

A complete theoretical model describing the above experimental results has been developed in Ref. [119]. The authors by means of a generalised Gross-Pitaevski equation [122] take into account the effect of the spotsize on the formation of the condensate. The main

reason for the observed condensation behaviour is the ballistic propagation of polaritons due to repulsive interactions. For a spotsize larger than 25 μm, condensation occurs at $k = 0$. The repulsive interactions create an anti-trapping potential that ballistically accelerates polaritons away from the centre, hence the k-space distribution is contained in the $k < k_c$ region. Although the frequency, ω_c, at which the condensation occurs is fixed, the variation of the (spatially dependent) pumping rate P_r across the pump spot is compensated by a spatial variation of the local wavevector k_c. The non-equilibrium character of polariton condensates is evident from the fact that the momentum space broadening is much larger than the energy broadening, predicted by the Heisenberg position-momentum principle. This is in contrast to condensates in equilibrium where the local wavevector k_c is zero everywhere.

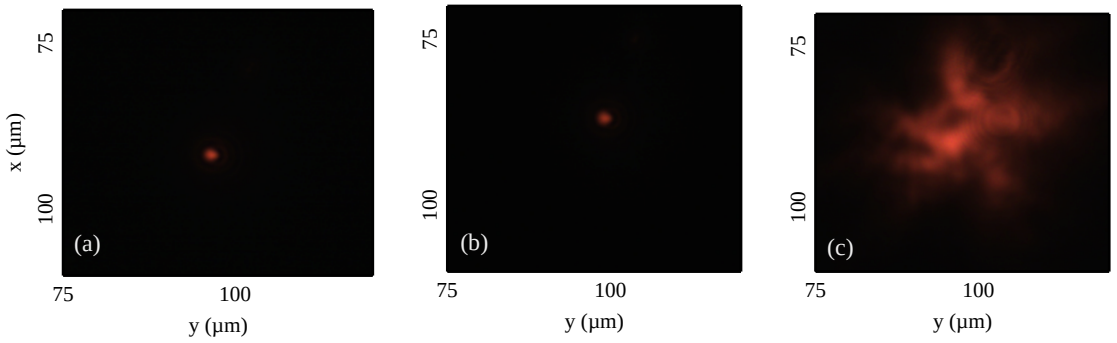

FIGURE 6.17: Near field polariton emission for $P = P_{th}$ for excitation spot sizes of (a) 0.8 μm, (b) 1.2 μm and (c) 4.1 μm.

However, a narrow peak centered at $k \neq 0$ can be observed upon large spotsize excitation [Figure 6.15f]. A weak disorder potential, included in the theoretical calculations presented in [119], can account for this feature. It leads to emission from several different, smaller areas within the excitation spot, which are mutually coherent and connected by lower density regions. This further underlines the non-equilibrium character of polariton condensates.

Further reduction of the spotsize leads to formation of the condensate at higher energies along the dispersion branch. For sizes less than 5 μm, the spotsize is comparable to the photonic disorder of the microcavity, and therefore causes spatial disorder of the polaritons. The condensate frequency, ω_c, is again fixed by the dynamics of the excitation region. However, most of the polaritons are found outside this region, ballistically propagating in the outward direction. Stronger emission occurs from a ring with radius

k_c while weakest emission is located in the region $k < k_c$. Polaritons still remaining in the central excitation region are responsible for this effect.

While operating in the linear regime, the emission spot is comparable to the excitation area. The free carriers that are created by the non-resonant excitation do not thermalize fast enough in order to form polaritons and don't live long enough to propagate in the plane. Polaritons that do manage to form on the other hand tend to accumulate in the bottleneck region. Given their energy dispersion, they obtain quite high group velocities, especially compared to lower energy polaritons, and can travel within their lifetime a distance of about 10 μm. Therefore, even in a highly disordered system like this one, polaritons can within their short lifetimes propagate over a few microns. In the nonlinear regime, as the condensate is formed, a strong reduction of the emission area is recorded, as well as the appearance of concentric rings.

The real- and the k-space are conjugated by the Fourier transform. Applying a Fourier transform to the k-space ring results in a much localised real space pattern, while the same method applied to the polariton ground state condensation gives a Gaussian shape. The appearance of concentric rings in the real space emission pattern confirms the transform relation between near- and far-field emissions, underlying the spatial coherence of the source [Figure 6.17 (a-b)].

6.6.4 A simplified explanation

By making several assumptions, a simple theoretical explanation can be derived regarding the behaviour of the condensate due to the spotsize. Assuming that the intensity profile of the spot represents an energy profile, its derivative gives the force $F(x) = dE/dx$. At the same time, this quantity equals the change in momentum in time dk/dt. Polaritons from the centre of the spot feel an accelerating force. As the force changes with their position, so does their acceleration. The force $F(x) = dE/dx$ is plotted in Figure 6.18 for the various spotsizes that have been experimentally studied. The derivative is, of course, higher in value for smaller spotsizes. The force is proportional to the obtained acceleration, $a(x)$. Within their lifetime, polaritons cover a certain distance x that is proportional to the acceleration $a(x)$, and subsequent force that they feel. Finally the position to which they manage to travel is translated in a specific force value, that is a specific wavevector.

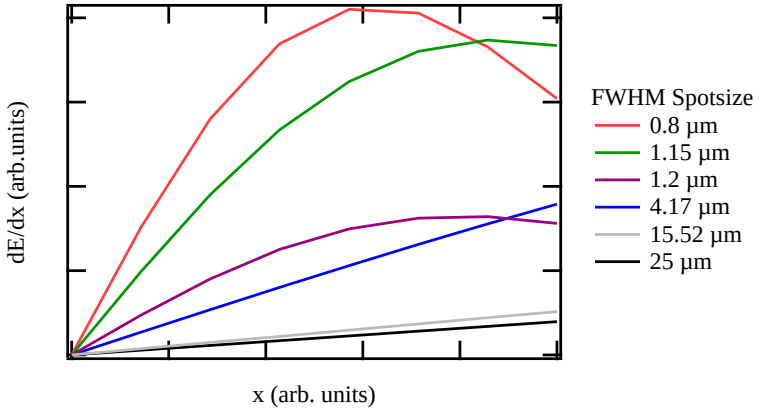

FIGURE 6.18: The force $F = dE/dx$ calculated for the various spotsize intensity proiles, annoted in different colors.

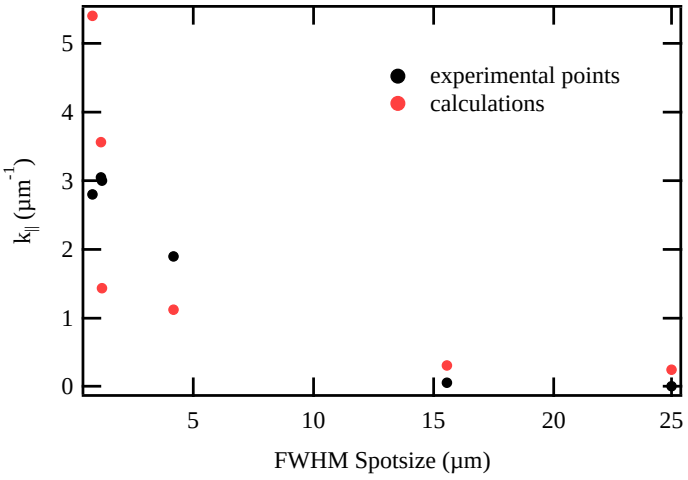

FIGURE 6.19: Experimental data and theoretical calculations regarding the wavevector of the condensate with respect to the FWHM of the spotsize.

For a certain range, the force F is linearly dependent on the position x, i.e. $F = dE/dx \propto x \propto a \cdot t^2 = dk/dt$. Integration of the last terms reveals that the wavevector k can be estimated by the slopes of the curves in Figure 6.18 after fitting their linear part. A comparison between experimental and theoretical points can be found in Figure 6.19. There is an agreement between the behaviour of the condensates with respect to the spotsize, i.e. polaritons obtain higher wavevector values upon use of a small excitation spot, but exact calculations demand a much more complicated model.

6.7 Conclusions

In conclusion, the formation of a macroscopic coherent polariton state in the time domain under non-resonant excitation is achieved. The transition between weak and strong coupling regime from a single excitation pulse allows for the observation of the formation of ground-state polariton condensation in a planar microcavity. Evidence including the evolution of the linewidth, the coherence as well the lower polariton branch dispersion with time further supports the above interpretation of the data. In the second half of the chapter, experimental data from a similar setup investigates the role of the excitation spotsize regarding polariton condensates when the microcavity is detuned at -11 meV. Condensation can occur at the ground or higher energy states, depending on the size of the excitation spot. Emission in the real space always from localized spots, within the excitation area due to photonic disorder. The spatial and spectral characteristics of the condensates are in excellent agreement with theoretical predictions.

At the time, polariton condensation at $k = 0$ under non-resonant conditions was still elusive. Since then a number of individual reports came to light, including condensation in a GaAs planar structure under continuous wave excitation [93] and a study regarding the time evolution of the coherence of a ground state condensate [123].

Chapter 7

Investigating the role of LO phonons in the generation of a ground state polariton condensate

Upon non-resonant excitation, the newly formed excitons relax first to high k-states and then rapidly along the dispersion branch due to scattering with acoustic phonons. Further relaxation to the bottom of the trap is hindered by the peculiar shape of their dispersion curve, as explained in Chapter 2.4. The bottleneck effect stands between polaritons and their condensation, the possibility for the population at the $k = 0$ state to exceed unity (probability of scattering is proportional to occupation number of final state to which they are scattered). Phenomena linked with polariton condensation have already been mentioned throughout this thesis, varying from fascinating physics (superfluidity, vortices etc) to possible applications (fabrication of low threshold, inversionless polariton lasers). A very important step has already been achieved towards the latter, with the realisation of electrically pumped polariton light emitting diodes in GaAs based microcavities that operate in the linear regime [90–92]. Two parameters have been hindering the realization of such devices: the efficient population of ground polariton states and the persistence of strong coupling under high carrier injection conditions. The efficient injection of active excitons in the microcavity and the overcome of the bottleneck is the key that will allow operation in the non linear strong coupling regime.

One possible solution is by exploiting the presence of phonons in the system [124]. Phonons are quantized modes (longitudinal or transverse) of vibration in a crystal lattice. There are two types of phonons: oscillations in which the atoms within the unit cell vibrate about their centre of mass (optical) and oscillations in which the centre of the unit cell vibrates (acoustic). The latter offer a very effective but slow scattering mechanism. Each relaxation step requires about 10 ps and can lead to the exchange of no more than 1 meV. On the other hand, interactions with the optical phonons are much more efficient, as they allow for the exchange of larger amounts of energy, on a picoseconds scale. More details on phonons, as well as their dispersion curves for GaAs can be found in Chapter 2.4.1.

The aim of the experiment is to create the following condition:

$$E_{exc} = E_{LP(k=0)} + E_{LO} \tag{7.1}$$

i.e. the excitation input energy should equal the sum of the energy for the LPB at the k=0 state and the longitudinal optical (LO) phonon energy. As for GaAs E_{LO} =36 meV, injection of carriers at 36 meV above the k=0 state will allow for population of the LPB by thermalization of a hot electron-hole pair with large k either by emission of a single optical phonon or multiple acoustic phonons. The latter is quite inefficient as the intermediate states have a finite probability of emitting photons out of the cavity, either by non-radiative decay or relaxation to states with $k \neq 0$. Therefore, creating conditions that would render the LO phonon emission the dominant relaxation process would lead quickly to the formation of a polariton condensation from the hot electron-hole pair that is initially created (Figure 7.1). The concept of utilising LO phonon emission to accelerate polariton relaxation was introduced by Imamoglu and co-workers [7] and experimental evidence of the process was shown in the linear regime by Pau *et al* [125].

In this experiment, the role of LO phonons is explored following the successful optical injection of carriers resonantly with the light-hole exciton energy (E_{LH}) and further formation of a condensate at k=0 for different detuning conditions, under pulsed excitation. Variation of the detuning conditions equals the tuning of the energy difference between the injected excitons (E_{LH}) and the lower polariton (E_{LP}). An increase in the intensity in the linear regime and a threshold reduction when $E_{LH} - E_{LP} = E_{LO}$ provide evidence

for the efficient use of LO phonons in the relaxation of the electron hole pairs towards the LPB.

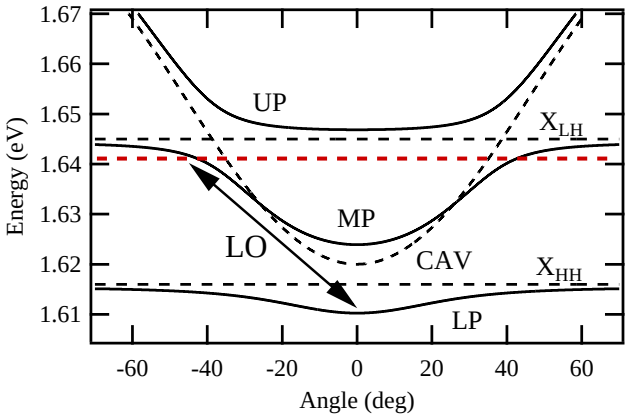

FIGURE 7.1: LO phonon assisted polariton scattering in a microcavity. When the microcavity is excited 36 meV above the $k = 0$ state of the LPB, polaritons with high wavevectors relax instantly to the lowest state of the branch, avoiding the bottleneck.

7.1 Experiment

The energy dispersions of the modes in the microcavity for various detuning conditions, δ, can be seen on Figure 7.2a. The changes in δ are essentially equal to the tuning the energy difference between the exciton and the LPB below, at and above E_{LO} (36 meV for the GaAs). As the LO phonons are dispersionless within the light cone, the electron-hole pairs that are injected in our system at high k-vectors can relax rapidly towards the k=0 state of the LP dispersion by emitting one LO phonon of negligible wavevector. This way, other relaxation mechanisms that are slower and inefficient (via exciton-exciton, acoustic phonon or polariton-polariton scattering) are obsolete. The open markers in Figure 7.2a are obtained experimentally and correspond to the LP emission energy peak below threshold. Their size is scaled with the LO phonon scattering strength that varies with detuning. The strength is proportional to the transition rate, $W(D)$, which can be extracted from the slope, S, of the power dependence in the linear regime (Chapter 7.2). The angular dispersion for the optimum detuning (-4 meV) is shown in Figure 7.2b.

Integrated photoluminescence is recorded at normal incidence with ±3° collection angle and is spectrally resolved using a 1200 grooves/mm grating in a 55 cm spectrometer coupled to a cooled CCD camera, as shown in Figure 7.3. A nonlinear increase of the

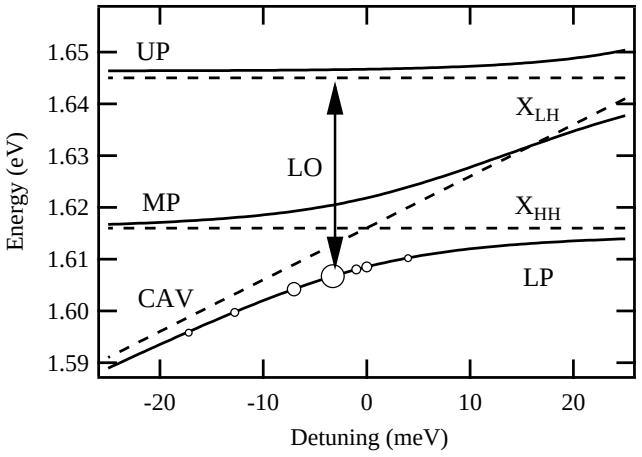

FIGURE 7.2: Energy dispersion of the cavity and exciton modes (dashed lines) and lower, middle and upper polariton (solid lines) as a function of detuning. The open markers correspond to experimental data and their size is proportional to the LO phonon scattering strength.

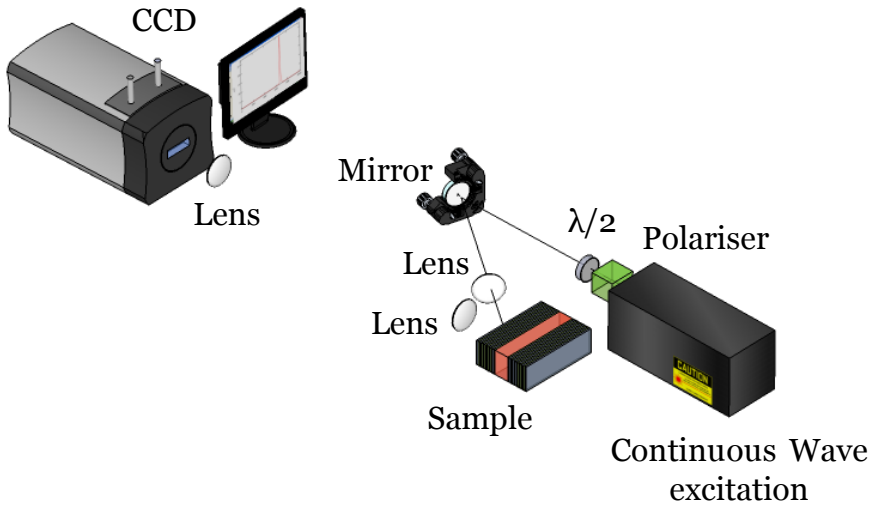

FIGURE 7.3: Experimental setup for the investigation of the role of LO phonons in polariton relaxation. The sample is excited non-resonantly at an oblique angle and emission from $k = 0$ is collected and spectrally resolved.

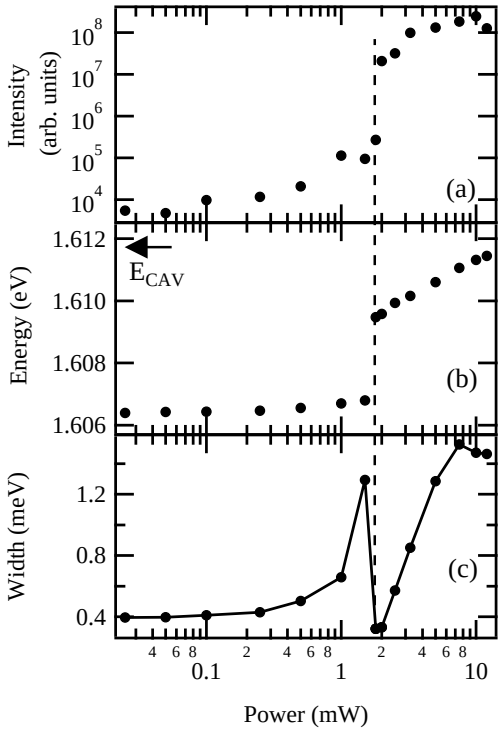

FIGURE 7.4: Power dependence of (a) the emission intensity, (b) the energy blueshift and (c) linewidth of the lower polariton branch as a function of the excitation power for -4 meV detuning.

photoluminescence intensity by 10^2 at threshold is observed with increasing excitation density [Figure 7.4a]. As expected, the emission energy blueshifts [Figure 7.4b] by about 3 meV at threshold, and continues until it coincides with the bare cavity mode at 1.612 meV. The emission linewidth gradually increases on approaching threshold where it collapses to a minimum value before increasing again [Figure 7.4c].

For comparison, the power dependence from a different, not optimum detuning is shown in Figure 7.5. The graph corresponds to a detuning of -17 meV and includes a power dependence of the emission intensity, energy and width. The traits are similar to the data shown in Figure 7.4, confirming that strong coupling hasn't been lost under these circumstances and polariton lasing is achieved, even under different detuning conditions. The intensity increases by two orders of magnitude, emission energy blueshifts and the width collapses to its smallest value as the cavity reaches the threshold to the nonlinear strong coupling regime. The difference lies in the excitation power value needed to achieve occupation of 1 in the lower polariton state , which is nearly twice the threshold for δ=-4 meV. It should be noted that the excitation powers have been scaled with the

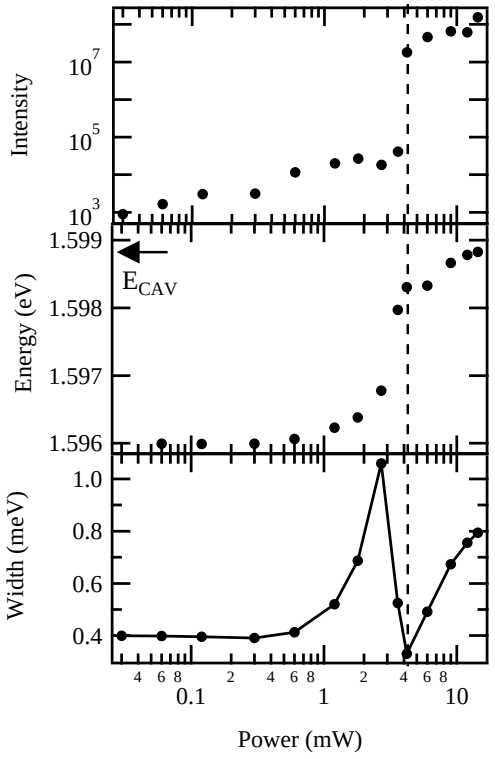

FIGURE 7.5: Power dependence of (a) the emission intensity, (b) the energy blueshift and (c) linewidth of the lower polariton branch as a function of the excitation power for -17meV detuning.

absorption coefficient of each detuning, allowing for a direct comparison between results obtained at different detunings.

7.1.1 Blueshift

Figure 7.6 combines the theoretical calculations regarding the bare cavity and heavy hole exciton modes (black dashed lines) as well as the lower and middle polariton modes' energies (black solid lines) with the emission spectra (red solid lines) obtained just above threshold for various δ. The black dots in Figure 7.6 correspond to the polariton emission energy below threshold whilst the red ones correspond to the emission energy just above it. Despite the observed blueshift, the LPB remains energetically below the bare cavity mode. One should also note that the emission at different δ undergoes different blueshift. The inset in Figure 7.6 shows the blueshift as a function of δ (black markers) and of the corresponding excitonic fraction (red markers). The blueshift has been studied extensively and is considered to be a combination of an individual blueshift due to the

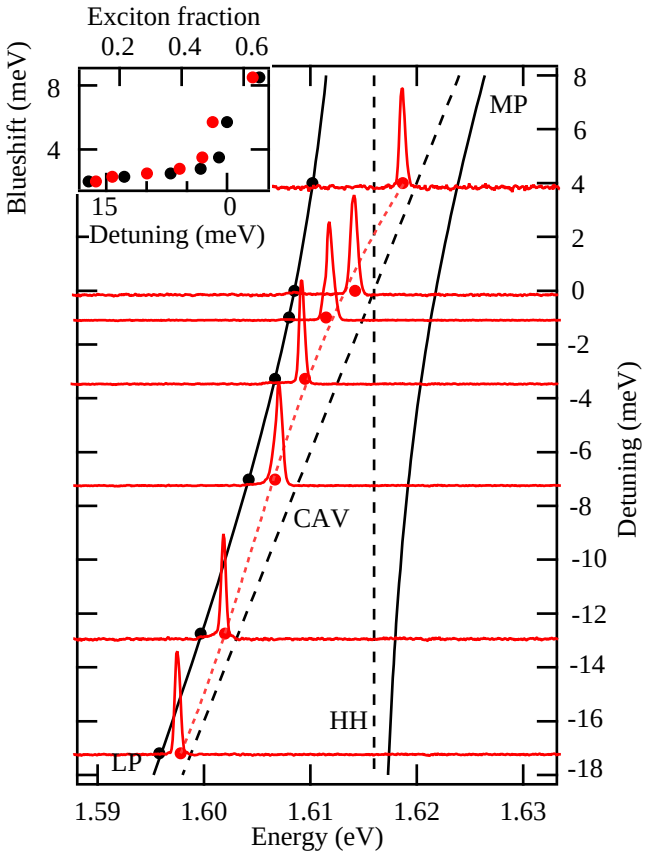

FIGURE 7.6: Energy dispersions of the cavity and heavy hole exciton (dust lines) and lower and upper polariton (solid lines) calculated theoretically. Emission spectra (red solid lines) above threshold, obtained under various different detuning conditions have been added. The black dots correspond to the emission energy below threshold while the red ones correspond to the blueshifted polariton emission just above it. (inset) Emission blueshift at threshold vs exciton fraction (red markers) and detuning (black markers).

polariton population of the mode and a collective one due to the excitonic blueshift that affects all the modes in the system [115]. It originates from the excitonic component of the polaritons which increases as δ becomes more positive, and hence explains the dependence of the blueshift at threshold on δ. Under pulsed excitation the blueshift of the LP evolves with time but this information is lost in time-integrated measurements and the dominance of polariton lasing results in an artificially large jump in mode energy upon reaching threshold [Figure 7.4b and Figure 7.5b]. Emission at threshold should not be attributed to emission from a redshifted cavity mode due to localised changes in the refractive index, as time resolved measurements confirm that at threshold, strong coupling is not lost. Snapshots of the LPB dispersion for the optimum detuning of -4 meV at different times at threshold are shown in Figure 7.7. The absence of the cavity

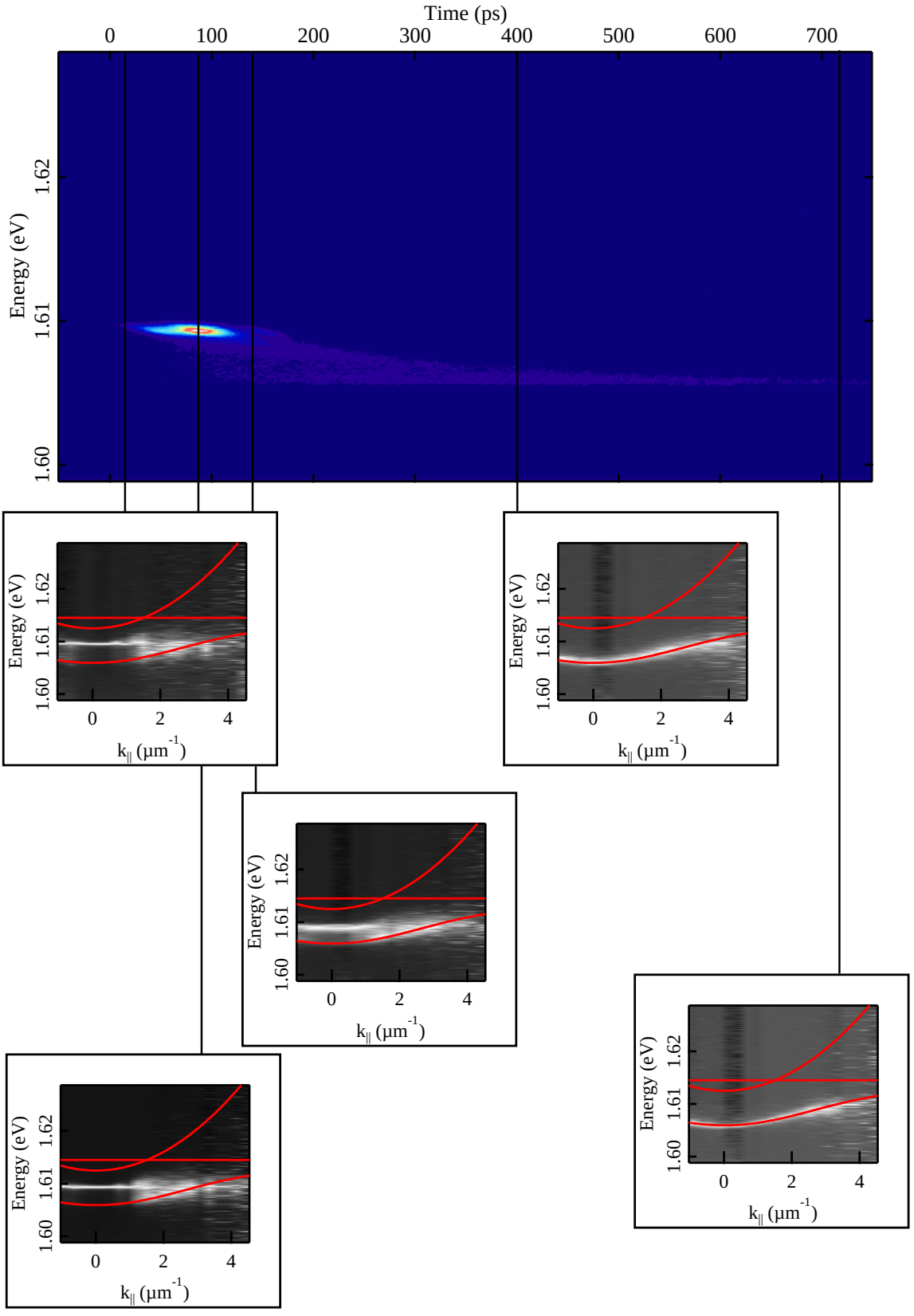

FIGURE 7.7: Energy and time resolved emission from the $k = 0$ state at a detuning of -4 meV (top panel). Dispersion images at the bottom panel correspond to times indicated by the black vertical lines. The red solid lines correspond to calculated exciton, cavity and lower polariton dispersions when the cavity operates at the linear strong coupling regime, i.e. below threshold.

mode dispersion strongly supports the above argument.

7.2 Theoretical explanation

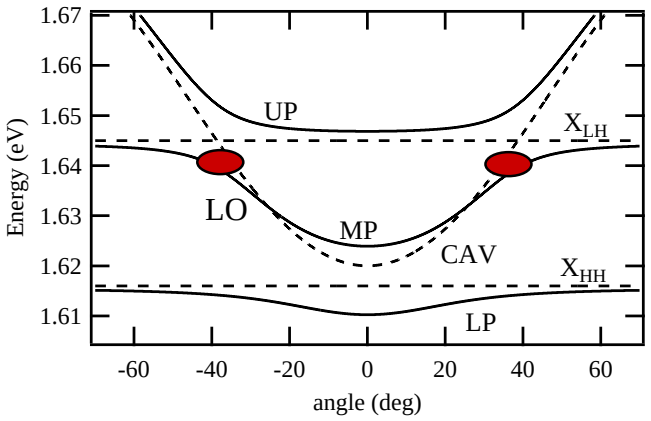

FIGURE 7.8: Energy dispersion of the cavity and exciton modes (dust lines) and lower, middle and upper polariton (solid lines) as a function of angle. The solid ellipses indicate the energy of the middle polariton bottleneck.

The theoretical explanation and simulations that follow, were conceived by by Tomáš Ostatnický (Charles University in Prague). After optical excitation by a short pulse, free electron-hole pairs quickly form exciton-polaritons in the middle (MP) and upper (UP) polariton branches due to wave vector and energy conservation [126]. They are further subject to energy relaxation by polariton-phonon and pair polariton interactions. The energy relaxation by longitudinal acoustic (LA) phonon emission predominantly allows for thermalization of the excited particles within the two upper branches while the LO phonon emission and pair polariton scattering lead to population of the lower polariton branch below the bottleneck region only due to the energy conservation. Coupling to the lower branch by LA phonon emission involves exchange of a momentum comparable to the inverse exciton Bohr radius and is therefore almost forbidden [58]. MP states are mostly LH-like in the initial stage of thermalization and therefore cannot effectively relax to the HH-like LP by LO-phonon emission (the relaxation rate is limited by the weak electron-hole exchange interaction). Strong exciton-photon coupling in a microcavity, on the other hand, mixes both LH and HH excitons in the MP bottleneck region and therefore coupling of the MP and LP bands by LO phonons becomes the strongest relaxation process in the system. The steep dispersion of the middle and lower polariton

branches around k=0 inhibits LA phonon emission resulting in polariton accumulation in the 'bottleneck' region of the MP dispersion curve, about 1-3 meV below E_{LH} [Figure 7.8]. This reservoir then strongly interacts with LO phonons, losing the rest of the energy by phonon emission and populating the system ground state at k=0 of the LP. The presence of the MP bottleneck provides a polariton reservoir from which the LP states are populated by a single LO phonon emission.

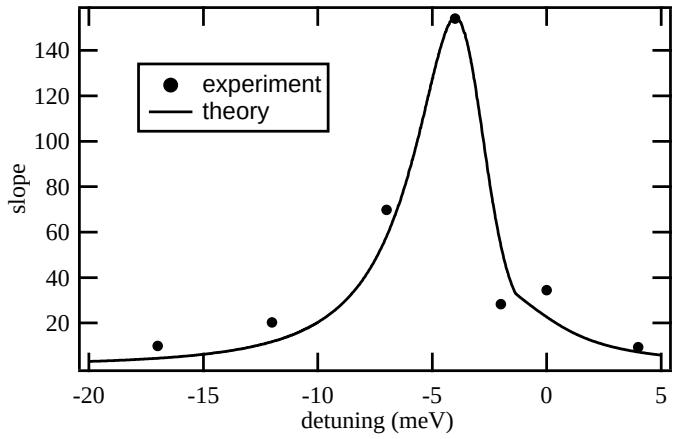

FIGURE 7.9: Experimental data (markers) and theoretical fit (line) for the slope $S(\delta)$ below threshold for a range of detunings.

As discussed above, by changing the cavity-exciton detuning δ, the energy gap between the MP bottleneck and the LP ground state can be tuned through the E_{LO} resonance. This leads to a detuning dependence of the LO phonon transition rate $W(\delta)$, which is maximum at resonance. The transition rate $W(\delta)$ can be found from the slope S of the power dependence in the linear regime (Figure 7.4a). A greater slope indicates an increased transition rate:

$$S(\delta) \propto C_{k_\parallel}^2(\delta) W(\delta) \tag{7.2}$$

where $C_{k_\parallel}(\delta)$ is the photon Hopfield coefficient of the $k = 0$ LP ground state. Figure 7.9 shows experimental (black dots) data for the detuning dependence of $S(\delta)$. It can be seen that the slope is almost two orders of magnitude greater when the LO phonon resonance condition is met, at a detuning of -4 meV, compared to e. g. the off-resonance condition of +4 meV or -13 meV. The black line in Figure 7.9 is a theoretical fit calculated using Fermi's golden rule (Appendix A) for the relaxation rate $W(\delta)$, assuming that the MP bottleneck occurs 2 meV below the E_{LH} and that the polariton line broadening is 1.3meV (taken from Figure 7.4c).

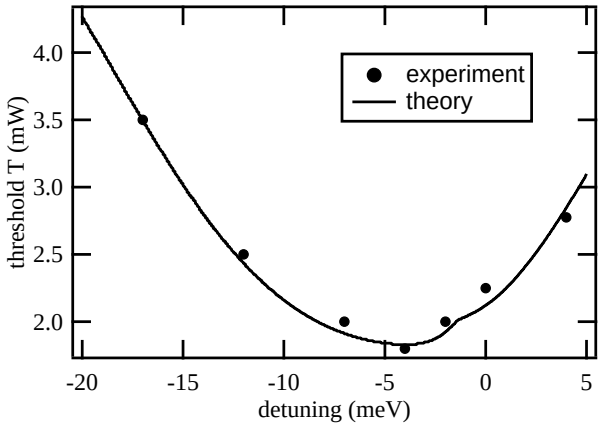

FIGURE 7.10: Experimental data (markers) and theoretical fit (line) for the stimulation threshold $T(\delta)$ for a range of detunings.

The stimulation threshold T is also dependent on $W(\delta)$. An increased transition rate means that the ground state is populated more efficiently, allowing the macroscopic population required for stimulation and condensation to occur at reduced pump powers. Experimental data for the detuning dependence of the condensation threshold is shown in Figure 7.10 (black dots). The stimulation threshold is assumed to have the form

$$T(\delta) = \alpha + \frac{\beta}{W(\delta)} \tag{7.3}$$

where α and β are constants chosen to best fit the experimental data. It is shown that the threshold is a minimum at the detuning where the LO phonon transition is on resonance (-4 meV), 50% lower than the off resonance case. The black line is a fit to the data based on the simple model and assumptions described above.

7.3 Comparison with non-resonant excitation

A similar set of studies has been performed with the pump laser tuned to be resonant with the first Bragg mode. In this case, similar trends to those in the resonant injection scheme were obtained. The optimum detuning remains at -4 meV, where lowest threshold and highest slope are achieved. Interestingly the threshold (scaled with the absorption coefficient) is similar for both excitation configurations, suggesting that LO phonon mediated relaxation mechanisms are present in both pumping schemes. However,

the slope of the power dependence in the linear regime is about 3 times lower compared to resonant excitation. It could be argued that under non-resonant excitation, a smaller proportion of the injected carriers collect at the MP bottleneck and undergo relaxation via LO phonons. In this case, it is likely that more carriers undergo LA phonon relaxation to the LPB, which would not be desirable for electrical injection. Resonant pumping is therefore proven to be much more efficient, contrary to reports in Ref. [127].

7.4 Conclusions

In this chapter, the possible role of LO phonons regarding polariton relaxation is investigated. A 50% reduction in the polariton stimulation threshold in a 2D GaAs microcavity is achieved by using LO phonons to efficiently relax polaritons from the MP bottleneck to the LP ground state. Several power dependencies allow for a complete study of the LO phonon transition rate and the findings suggest that relaxation is more efficient when carriers are injected resonant with the E_{LH} compared to non-resonant excitation.

The use of LO phonons to reduce the polariton stimulation threshold may prove significant in the development of electrically pumped polariton lasers, which is one of the ultimate goals of the field. Resonant injection allows LO phonon mediated relaxation to dominate over LA phonon, bypassing the bottleneck effect that prevents operation of electrically pumped polariton lasers to date. Relaxation under such pumping conditions proves to be more efficient than non-resonant, as shown in the above results. The MP bottleneck turns out to be a very useful reservoir from which LO phonon scattering can occur directly to the lower polariton ground state. Operation relies on the light- and heavy-hole exciton energies being approximately equal to the LO phonon resonance energy, as that will place the MP bottleneck in the appropriate energy. The existence of such a state in GaAs based systems, renders this material more appropriate for the development of polariton lasing devices.

Chapter 8

Polariton condensation in 0D microcavities

The pursuit of polariton condensation in semiconductors has triggered several experiments to overcome the peculiar shape of the lower branch dispersion curve and the resulting bottleneck effect. As no polariton condensation was unambiguously demonstrated in GaAs structures at the time, it was believed that spatial confinement would be the solution, as it increases the density of polaritons per state, without increasing the density of excitons per cm^2. This would facilitate reaching the condensation threshold of one polariton per state, without losing the strong coupling and the bosonic properties of polaritons. One efficient way of confinement along all spatial directions is by laterally patterning a planar microcavity in the shape of micropillars. In such cavities, photons are confined not only vertically by the Bragg mirrors but also laterally by the contrast in the index of refraction between air and the semiconductor. Confinement by the latter case results in the appearance of a number of photon modes in the system, due to the broken translational invariance, depending on the size and shape of the pillars. In the strong coupling regime, polaritons come from the mixing between each of these 0D photon modes and the QW excitons. Due to their light effective mass, lateral confinement on the micron scale is sufficient for quantising the polariton states, which makes fabrication and optical addressing much easier than for other nanostructured systems. Several nonlinear phenomena have been reported in such structures including parametric oscillations and polariton parametric scattering [28, 101].

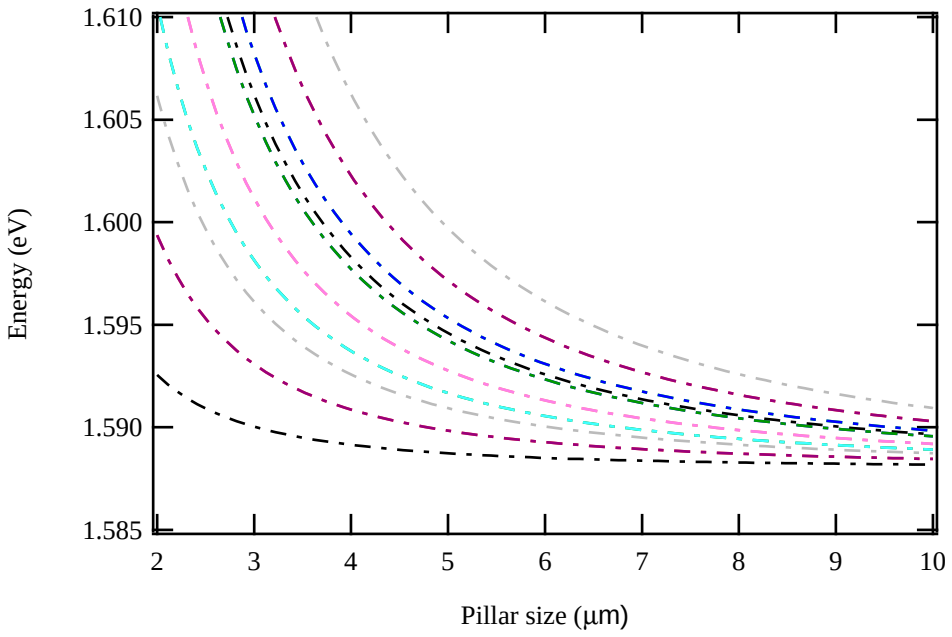

FIGURE 8.1: Energy spectrum of a number of photon modes confined in micropillars versus their size.

8.1 Zero dimensional polaritons

In this chapter temporal and spectral properties of polaritons created in a GaAs microcavity etched down into pillars of different sizes and detunings are investigated. As mentioned above, confinement in two directions results in the appearance of multiple cavity resonances in the cavity. Calculations for the optical modes in rectangular pillars can be found here [98], whereas the case of circular pillars has been treated here [99]. Energy spectra of the confined photon modes for the latter and their evolution as the pillar size increases are shown in Figure 8.1. Their energy separation strongly depends on the pillar size. Our experiments were performed on square pillars and 'pillar size' from here onwards refers to the 'pillar side size'. As the pillar size decreases the modes become more clearly separated in energy. When strongly coupled with the exciton resonance, a plethora of polariton modes is created.

A wedge in the layer thickness of the cavity provides access to a variety of detunings through the relative change in energy between the lowest cavity mode with respect to the exciton. The different traits that occur in pillars of different sizes and detunings

under nonresonant excitation are studied both in time- and spectral- domain. A kinematic model that includes various scattering mechanisms is introduced to describe the experimental data including condensation switching from non ground to ground states.

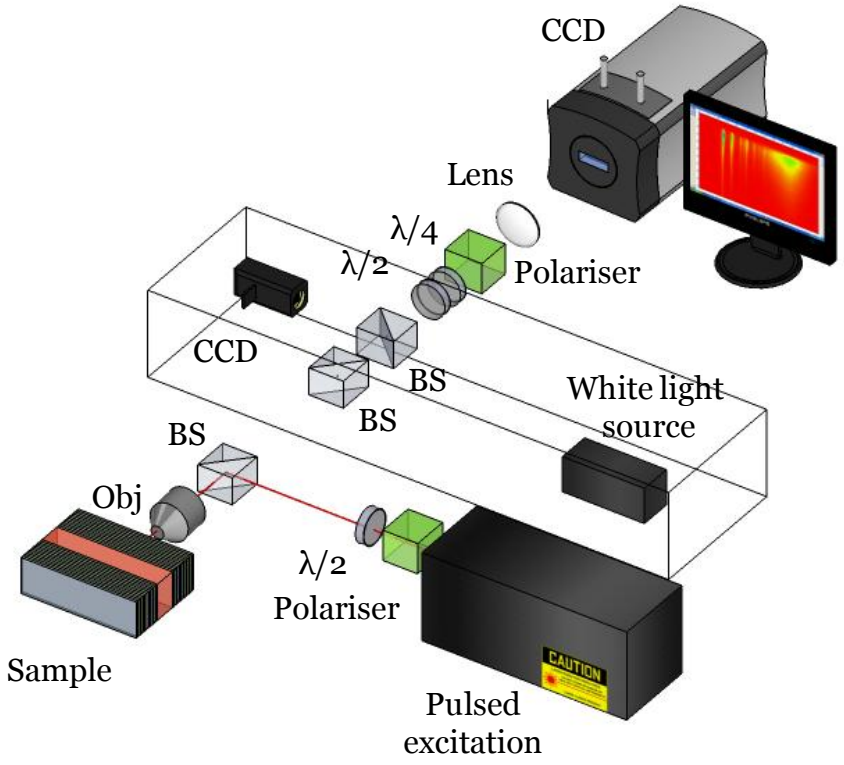

FIGURE 8.2: Experimental setup for the investigation of polariton dynamics in a 0D structure. The components within the box constitute an imaging microscope for 'navigation' over the sample. The waveplates in front of the CCD allow for the investigation of the polarisation properties of the sample.

8.1.1 Experimental setup

The sample, described in section 3.3, is excited non-resonantly using 150 fs transform limited pulsed excitation with a repetition rate of 80 MHz. A microscope objective, aligned normal to the sample surface, is used to both focus the excitation beam to a spot of about 3 μm and collect photoluminescence (PL). The excitation spot covers the whole area of the sample and allows to consider homogeneous exciton density across the sample. The objective is always positioned in order to detect maximum PL from the ground state polariton mode, i.e. in the centre of the ground mode. The sample is cooled to 7 K in a continuous flow cold finger cryostat (Figure 8.2). In order to achieve efficient

excitation the laser is tuned to 1.70 eV, corresponding to the second Bragg mode of the system above the stop band, where the reflectivity is at a minimum, as shown with an arrow in Figure 8.3. A spectrometer coupled to a streak camera is used to simultaneously record the temporal and energy dynamics of the photoluminescence.

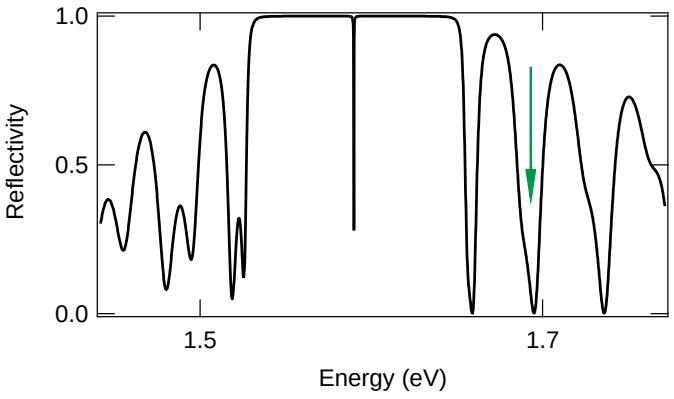

FIGURE 8.3: Calculated reflectivity spectrum of the sample; the arrow indicates the energy of excitation.

8.1.2 PL measurements

Figure 8.4 presents below threshold photoluminescence spectra for zero detuned pillars of side dimensions 2.4 μm (a), 3.2 μm (b), 5 μm (c), 6 μm (d), and 10 μm (e). Previous interpretations of data obtained from the same sample in a similar experiment assumed that the highest energy state (FWHM 4-5 meV) corresponds to uncoupled quantum well exciton PL collected from the side of the pillars. However, further evidence does not support this assumption, but suggests that the high energy state PL corresponds to the bottleneck reservoir (for more details see Section 8.4). For the pillar with the smallest side size (Figure 8.4a) one can see that the energy separation allows only two modes to appear below the high energy wide band while for larger pillars a larger number of modes is allowed (e.g. (Figure 8.4e)). Unfortunately they can't be resolved as their separation is below the energy resolution of the streak camera system. Although polariton lasing is observed in all pillar sizes [27], the threshold to the strong coupling non linear regime occurs at different excitation powers, with the threshold having a linear relation with the pillar size (Figure 8.4f)

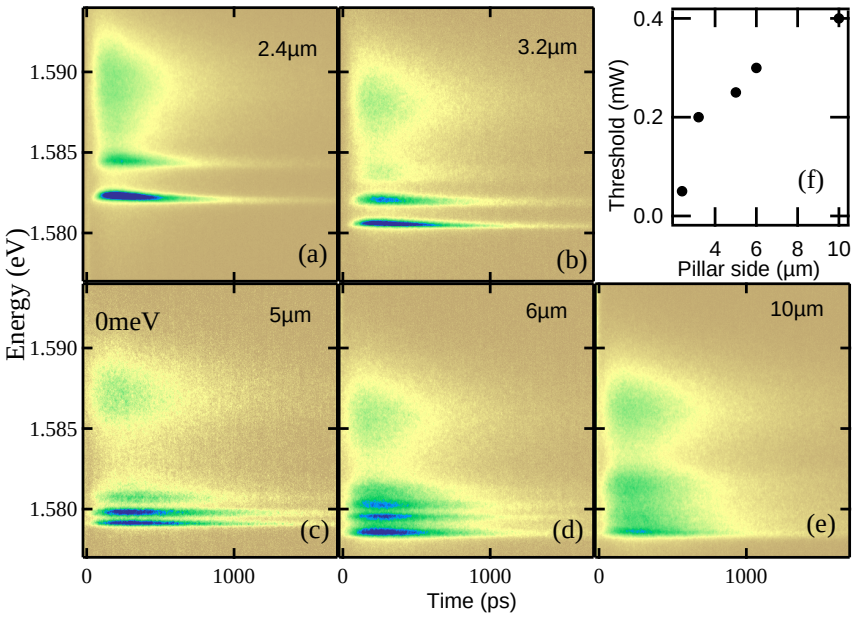

FIGURE 8.4: Below threshold photoluminescence for a square pillar with (a) 2.4 μm side, (b) 3.2 μm side, (c) 5 μm side, (d) 6 μm side and (e) 10 μm side for zero detuning conditions. (f) Threshold power for polariton amplification vs side.

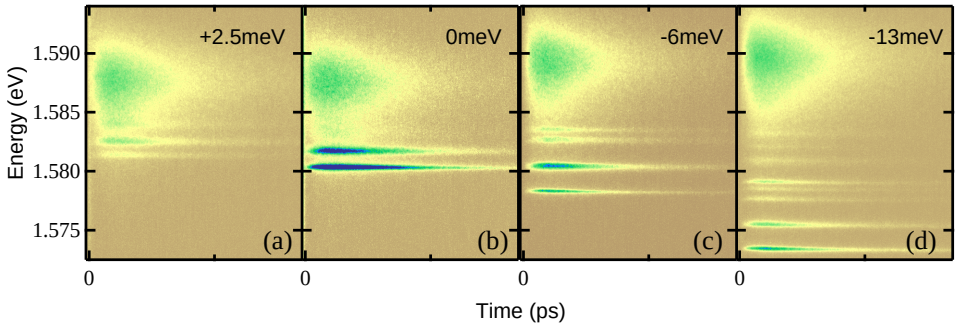

FIGURE 8.5: Below threshold photoluminescence for 3.2 μm side square pillar at (a) 2.5 meV, (b) 0 meV, (c) -6 meV and (d) -13 meV detuning.

Figure 8.5 presents below threshold photoluminescence spectra for 3.2 μm side pillars at (a) -2.5 meV, (b) 0 meV, (c) -6 meV and (d) -13 meV detuning. As there is no variation in the size of the pillars, the energy separation between the modes is expected to be the same. The detuning however (which is calculated as the energy difference between the exciton resonance and the ground photon mode for pillars), affects the number of modes that are allowed below the exciton energy. As the detuning becomes negative, the number of visible polariton modes in the spectrum increases. The PL decay dynamics of the lower energy states are not defined by the cavity lifetime ($\sim$ 15 ps here) but from the

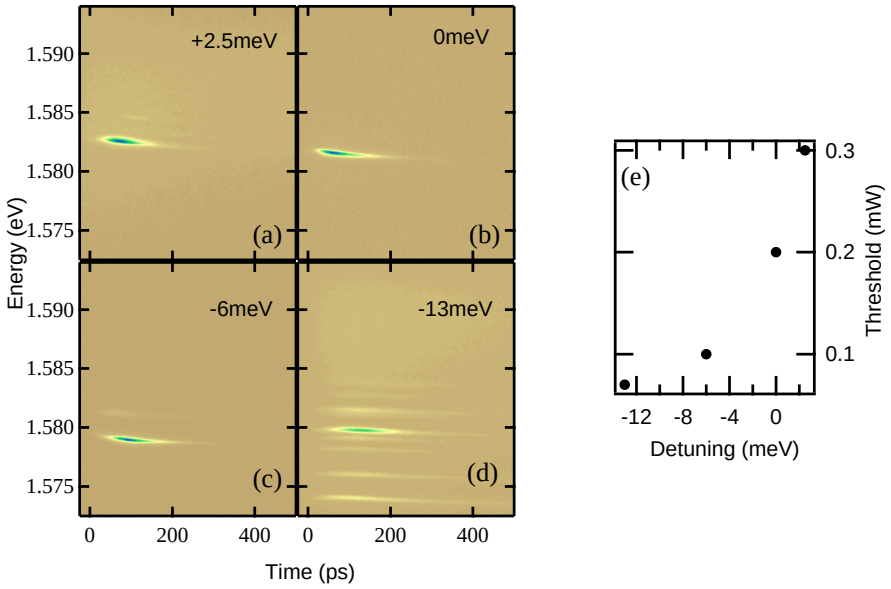

FIGURE 8.6: At threshold to the strong coupling non linear regime photoluminescence for 3.2 μm side square pillars of (a) 2.5 meV, (b) 0 meV, (c) -6 meV and (d) -13 meV.

relaxation dynamics to each state. The main relaxation mechanisms are exciton-exciton scattering and pair polariton scattering when the energy separation of the modes allows for energy conservation between the involved states. Relaxation via acoustic phonons only occurs when the energy difference between the states is favorable and is therefore limited. For all detuning conditions, it is evident that states that are energetically closer to the exciton reservoir decay faster due to the scaling of the exciton-exciton scattering strength, which is proportional to the exciton fraction of the polariton state (Section 2.4.2). The interplay between the two main relaxation mechanisms is different for the various detunings as it depends on the excitonic fraction of the modes. Therefore the first mode that, reaches unit occupancy by multiple relaxation leading to operation in the strong coupling non linear regime is not always the ground state. Figure 8.6. presents PL spectra at threshold for each one of the detunings of Figure 8.5. All detunings achieve only ground state condensation with the exception of δ=-13 meV where competition between the exciton-exciton scattering and pair polariton scattering mechanisms allows for a non-ground state to reach threshold first, before changing finally to the ground state as the carrier density in the system increases. Negatively detuned pillars exhibit a lower lasing threshold as one can see in Figure 8.6e.

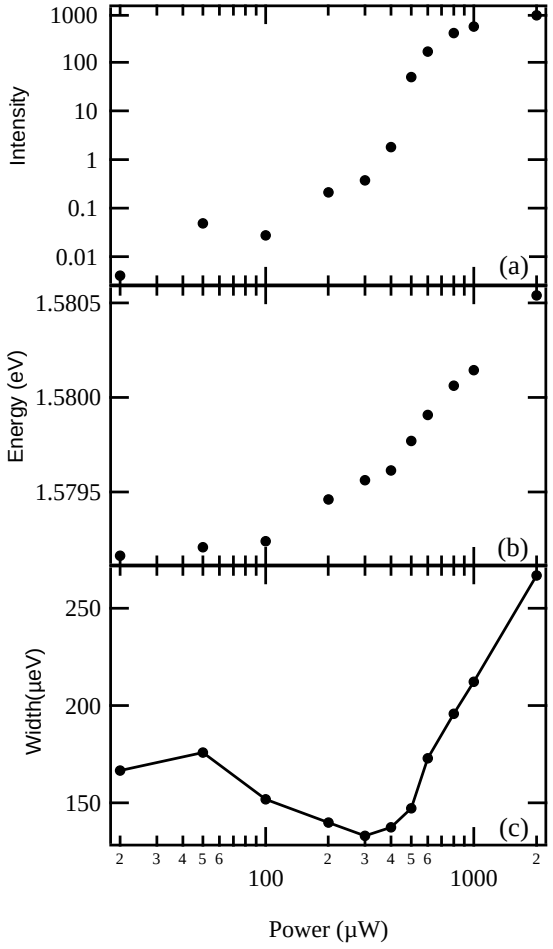

FIGURE 8.7: Power dependence of (a) the intensity, (b) the energy blueshift and (c) linewidth of the ground state emission as a function of the excitation power for a 5 μm side square pillar at zero detuning.

8.1.3 Polariton Condensation in Micropillars

Figure 8.7 presents a typical power dependence performed on one of the pillars regarding the emission intensity, energy and width (for a 5 μm side square pillar at zero detuning). A non-linear increase of the PL intensity at threshold is observed with increasing excitation density (Figure 8.7a). The emission energy, on the other hand, exhibits the expected blueshift, basic characteristic of strong coupling non linear regime (Figure 8.7b). The emission linewidth gradually increases and collapses to a minimum value at threshold, due to the increased coherence in the newly formed polariton condensate. Above threshold it increases again due to increased scattering within the condensate (Figure 8.7c). The experiment findings confirm that polariton lasing is achieved in all square pillars

with size and detuning conditions as the one described above, showing similar behaviour regarding the intensity, energy peak and width [27].

8.1.4 Blueshift

An important issue that has been the topic of intense discussions is the origin and the mechanism behind the observable blueshift of the polariton mode when it undergoes lasing, whether it occurs in a 2D or 0D structure. Generally it is considered to be a combination of an individual blueshift due to the polariton population of the mode in question and a collective one due to the excitonic blueshift caused by the exciton screening and carrier carrier interaction at the reservoir [115, 128, 129]. Previous experiments on this sample [27] report that under continuous wave non-resonant excitation, the modes were shown to blueshift differently, suggesting that each mode's polariton population is responsible. Figure 8.8 presents the energy of various polariton modes as the excitation power increases. Figure 8.8a corresponds to a 3.2 μm size pillar at a -13 meV detuning whereas Figure 8.8b corresponds to a zero detuned 5 μm size pillar. In both cases, all modes exhibit the same blueshift indicating that the blueshift is mainly due to the excitonic blueshift and is only slightly affected by the individual polariton mode population.

8.2 Non ground state polariton condensation

Although polariton condensation occurred in the lowest energy state in most of the investigated pillars, in one case, non ground state condensation was achieved. This section is dedicated to this peculiar observation.

8.2.1 Overview

Spontaneously occurring ground state condensates have been reported in atomic and solid state systems and are well described by the theory of equilibrium and non-equilibrium BEC [130]. An interesting extension to this theory has predicted that BEC can occur in states other than the ground state, but to date there has been no experimental

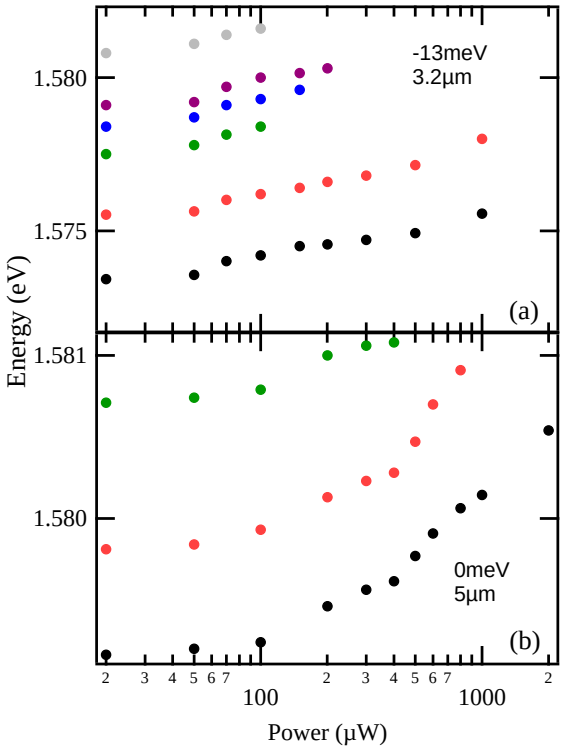

FIGURE 8.8: Power dependence of the energy emission of various polariton modes for (a) a 3.2 μm side square pillar negatively detuned at -13 meV and (b) a 5 μm side square pillar at zero detuning.

evidence of non-ground state BEC. Spontaneously occurring non-ground-state polariton condensation in GaAs/AlGaAs pillar microcavities is achieved under non-resonant optical excitation. Tuning the level separation of the polariton energy states in pillar microcavities provides control of the mode switching between non-ground-state and ground-state polariton condensation. A kinematic model is introduced where the interplay of exciton-exciton and pair polariton scattering can adequately describe the observed mode switching as each of the above scattering mechanisms becomes prevalent at different carrier densities.

8.2.2 Experimental Data

The power dependence of the emission intensity of pillars at -13 meV and at zero detuning is shown in Figure 8.9(a-b), with hollow markers indicating the regime where emission is strongest from the higher energy mode. The fact that emission occurs in the strong coupling regime can be confirmed by the continuous relative blue shift of the

involved polariton states involved. For comparison the blue shift of the ground polariton state at zero detuning is plotted as well. At -13 meV the higher occupied energy state is switching from the ground polariton state to a higher energy state and back to the ground polariton state. The spontaneous mode switching occurs at the threshold to the non-linear regime rendering this observation interesting in the framework of spontaneously occurring non-ground state polariton condensation. Non-ground state polariton condensation was previously observed in pillar microcavities under non-uniform excitation conditions, where edge excitation of a pillar was used to trigger stimulated scattering towards polariton modes with matching field spatial distribution. Here, the pillars are uniformly illuminated and thus non-ground state polariton condensation is not driven by the excitation beam profile but is spontaneously occurring.

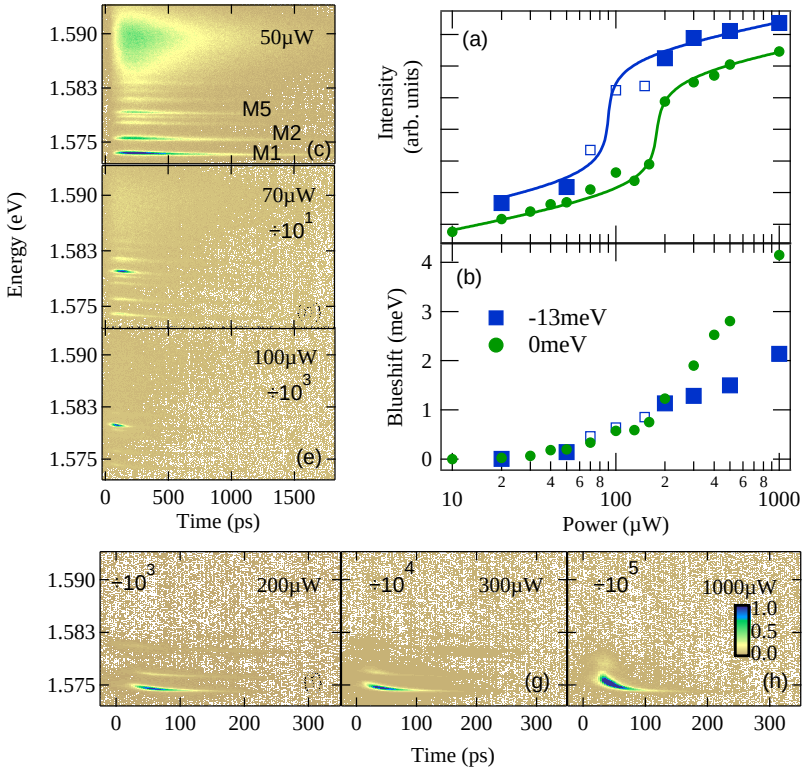

FIGURE 8.9: Power dependence of (a) the emission intensity and (b) the energy blueshift that occurs for a 3.2 μm square pillar at zero and -13 meV detuning. The hollow markers correspond to the higher energy mode that exhibits polariton amplification for a certain range of excitation powers.(c-h) Power dependence of photoluminescence from a 3.2 μm pillar at -13 meV detuning.

8.2.3 A simple kinematic model

Polaritons in pillar microcavities are not in thermal equilibrium, and therefore studying the transient dynamics of polariton relaxation at the detuning condition where non-ground state polariton condensation is observed, provides meaningful insight to the dynamics that lead to this unusual occurrence. Hereafter M1 is used to refer to the lowest energy polariton mode, M2 to the second lowest polariton mode and M5 to refer to the mode where non-ground state polariton condensation occurs. The naming convention is shown in Figure 8.9c. The results of a power dependence, under non-resonant optical excitation in Figure 8.9(c-h) show the PL decay dynamics of the different polariton modes. In the linear regime (Figure 8.9c) the photoluminescence decay is of the order of several hundred picoseconds. At threshold (Figure 8.9d) polariton condensation occurs at the higher energy mode M5. The transition to the non-linear regime is observed by the power dependence of the emission intensity (Figure 8.9a), the collapse of the photoluminescence to a single mode (Figure 8.9b) and the reduction of the decay time by an order of magnitude (Figure 8.9d). At an excitation power of three times above threshold, polariton condensation switches to the lowest polariton mode, M1 (Figure 8.9f). At this excitation power, past polariton condensation the re-population of M5 at approximately 200 ps from the residual exciton reservoir can be resolved (Figure 8.9g).

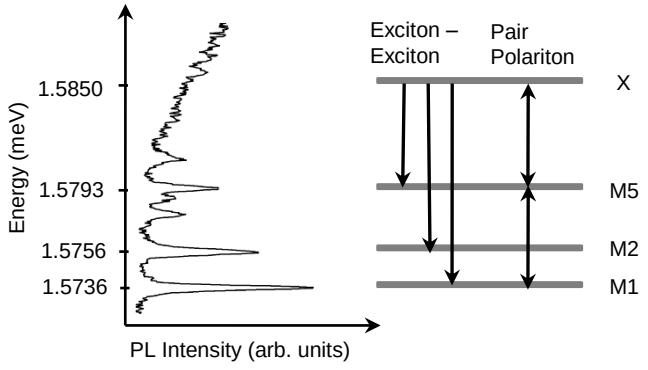

FIGURE 8.10: Below threshold photoluminescence spectrum from a 3.2 μm square pillar at δ=-13 meV detuning and schematic representation of the energy transitions between the exciton reservoir and polariton states M1, M2 and M5. Arrows indicate exciton-exciton and pair-polariton scattering between the states.

For polariton condensation to switch from a higher energy state (M5) to a lower energy state (M1) there needs to be a scattering mechanism that will populate M1 while depopulating M5. Figure 8.10 presents a photoluminescence spectrum in the linear regime

depicting the three polariton modes that dominate the observed dynamics and the relaxation channels coupling them. Other than exciton-exciton scattering, pair polariton scattering can occur for any three modes that are equidistant in energy, and at -13 meV detuning this process is indeed possible between M5, M1 and the low energy tail of the exciton reservoir. Scattering via acoustic phonons is not included in the model as the maximum allowed exchange energy doesn't exceed 1 meV, and this rule can't be satisfied in our system. It is expected that when M1 reaches occupation larger than one, final state stimulation of pair polariton scattering occurs, rapidly depleting M5 and therefore switching polariton condensation to M1. Pair polariton scattering in pillars does not require conservation of the in-plane wavevector and therefore the exciton states populated from pair polariton scattering will be distributed across a large range of wavevectors on the exciton dispersion. This can explain the absence of any observable enhancement of the emission from these exciton states within the light cone.

The observed dynamics can be quantitatively described by considering a simple kinetic model that couples exciton reservoir and polariton modes through exciton-exciton, and pair polariton scattering. The following rate equations (Chapter 2.4) describe the population n_i, for each of the states: [42, 54, 115]

$$\begin{aligned}\frac{\partial n_x}{\partial t} = &-\Gamma_x n_x - \sum_3 A n_x^2 (C_j n_j + 1) \\ &+ B(-C_{M1} n_{M1} D n_x (C_{M5} n_{M5} + 1)^2 \\ &+ C_{M5}^2 n_{M5}^2 (C_{M1} n_{M1} + 1)(D n_x + 1)) + f(t)\end{aligned} \tag{8.1}$$

$$\begin{aligned}\frac{\partial n_j}{\partial t} = &-\Gamma_j n_j + A n_x^2 (C_j n_j + 1) \\ &+ B(-C_{M1} n_{M1} D n_x (C_{M5} n_{M5} + 1)^2 \\ &+ C_{M5}^2 n_{M5}^2 (C_{M1} n_{M1} + 1)(D n_x + 1))\delta_{jM1} \\ &- 2B(-C_{M1} n_{M1} D n_x (C_{M5} n_{M5} + 1)^2 \\ &+ C_{M5}^2 n_{M5}^2 (C_{M1} n_{M1} + 1)(D n_x + 1))\delta_{jM5}\end{aligned} \tag{8.2}$$

$$j = M1, M2, M5 \tag{8.3}$$

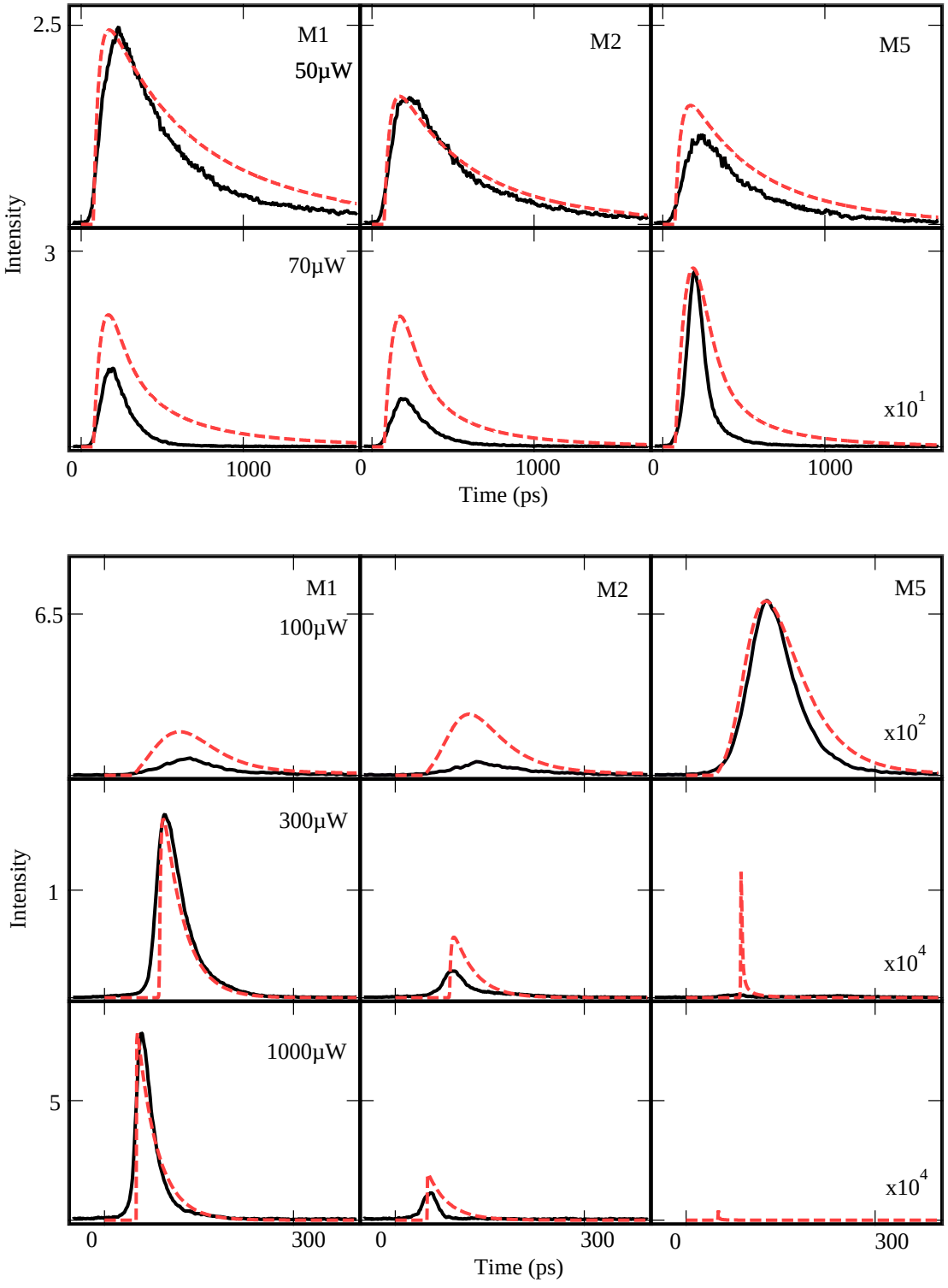

FIGURE 8.11: Comparison of the measured photoluminescence decay curves (solid lines) and the fit of the theoretical kinematic model (dotted line). Columns correspond to different polariton states (M1, M2, M5 from left to right) and rows to different excitation power (50 μW, 70 μW, 100 μW, 300 μW and 1000 μW from top to bottom).

where n_x is the exciton population at the exciton reservoir; A, B are the exciton-exciton and pair polariton scattering constants;[1] C_j is the exciton fraction of the j state; D is the fraction of the exciton reservoir that participates in pair-polariton scattering; and $f(t)$ is the pumping term. The first term on the right hand side of the equations describes radiative decay from each state, where the decay rate Γ_j is extracted from the measured linewidth of each mode. The second term describes exciton-exciton scattering and the last terms describe the pair-polariton scattering. Energy conservation is required and limits pair polariton scattering between modes M1, M5 and the lower energy tail of the exciton reservoir ($\leq$4% of the total population), which are spaced equidistantly in energy.

The coupled differential equations are solved for different excitation powers and the transient populations of the three polariton modes scaled through the corresponding photon fraction are shown alongside the experimental data in Figure 8.11. Each column corresponds to one polariton mode and each row to a different excitation power, matching those shown in Figure 8.9 (c-e, g, h). For low excitation powers (top panels) exciton-exciton scattering is the dominant relaxation mechanism and all modes exhibit PL of similar intensity, and decay times of hundreds of picoseconds, in agreement with the experimental data. At threshold (third row of panels in Figure 8.11), the higher energy state M5 is first to reach occupancy of one leading to a collapse of polaritons towards this state at threshold. As the pump power is increased above threshold pair polariton scattering dominates the dynamics and relaxation begins to favour the ground state again. The model replicates the experimental data and condensation switches to state M1 (fourth row in Figure 8.11). This simple kinetic model adequately describes the most important features of the experiment, including condensation from different modes and changes in relaxation times of more than an order of magnitude. The disagreement between the experimental data and the theoretical results at excitation powers of 100 μW and 300 μW can be attributed to the fact that not all the modes that appear in the experimental data are included in the model and therefore the decay mechanisms between them are missing. This results in higher predicted transient populations in the model compared to the measured time profiles.

In conclusion, the tunability of the relaxation mechanisms in pillar microcavities due to the discretisation of the energy states offers unique control over the state where polariton condensation occurs. Both ground and non-ground state polariton condensation

[1] The relative strength of the scattering constants A, B is 1:17.

is possible and the choice between the two is determined by the relaxation mechanism that is prevalent in the system for a particular carrier density. Within the framework of non-equilibrium BEC this is a manifestation of spontaneously occurring non-ground state BEC, the theory of which, although developed for trapped atoms, is currently work in progress for polaritons in semiconductor microcavities.

8.3 Polarisation related findings

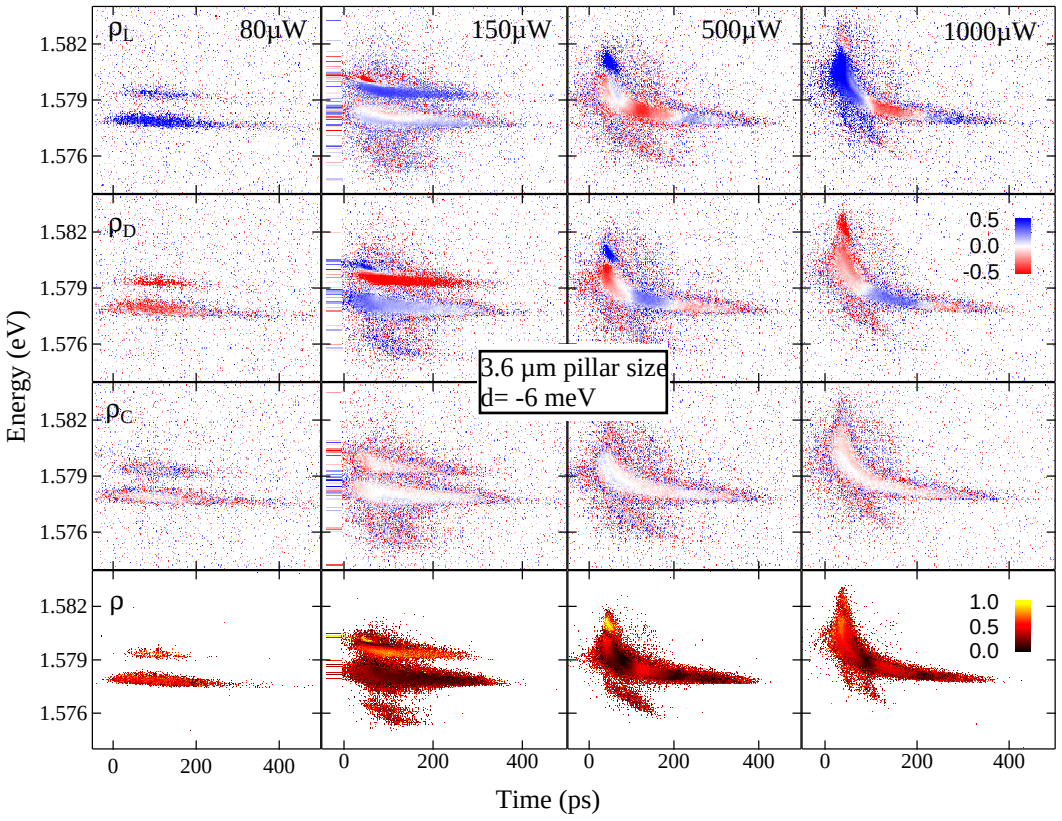

FIGURE 8.12: Comparison of the measured polarization components and the overall polarization for a negatively detuned pillar (δ=-6 meV) of 3.2 μm side size. Columns correspond to different excitation powers (80 μW, 150 μW, 500 μW and 1000 μW from left to right) and rows to the different polarization components (ρ_L, ρ_D, ρ_C and ρ from top to bottom.

The polarization of light can be fully characterised through the Stokes parameters, as described in chapter 2.5.1. In order to measure the 3 degrees of polarization (linear, diagonal and circular), the 6 polarization components (Equation 2.41) are collected through waveplates accordingly aligned, allowing for calculation of the three degrees of polarization in the Stokes sphere, as well as calculation of the overall polarization.

Figure 8.12 presents the three polarization components as well as the overall polarization for a negatively detuned pillar (δ=-6 μeV, for various input powers). Due to the detuning of the pillar, two modes are clearly detected below threshold. Emission is mostly unpolarised for the linear regime. As the input power increases to 150 μW, the higher energy mode gets strongly polarised in the linear plane, even though the cavity is still in the linear regime. At higher powers (500 μW and 1000 μW) oscillations occur on the linear plane with constant period, regarding all components but the circular one. Throughout the power dependence the circular component remains zero.

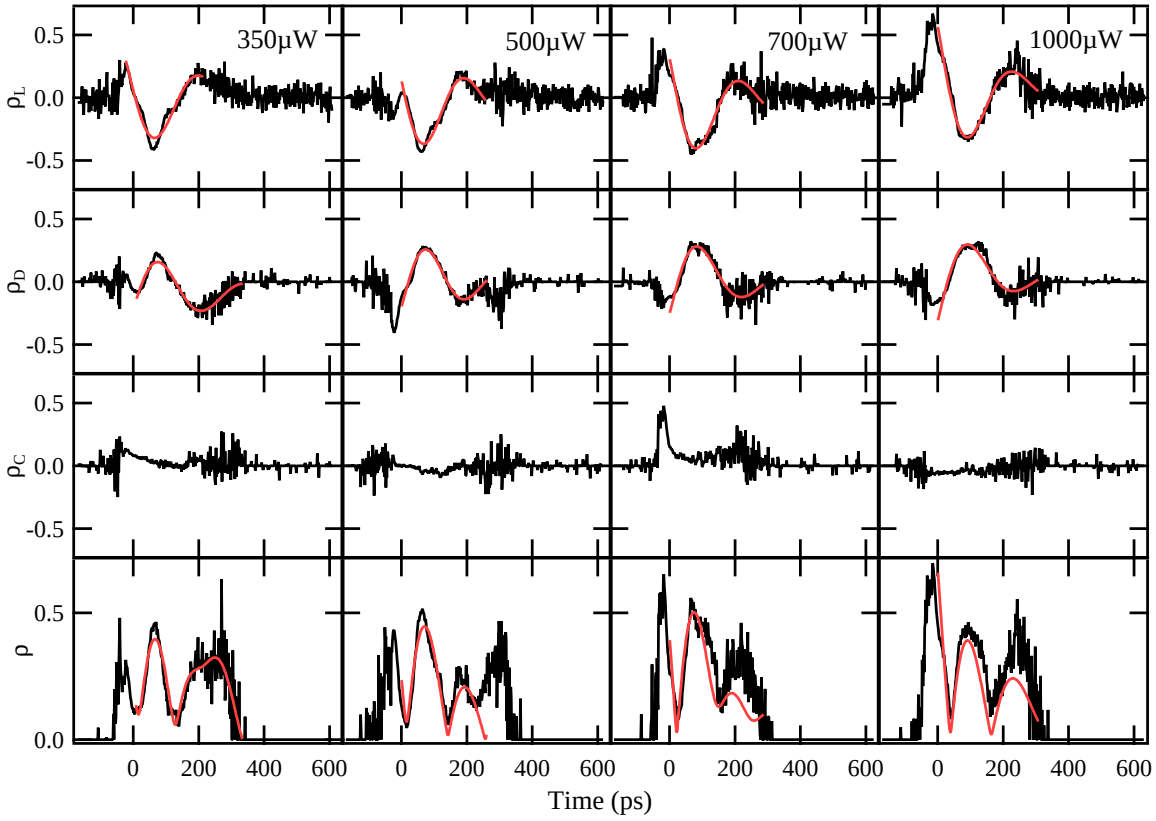

FIGURE 8.13: Time profiles of the polarization components of the emission above threshold from a negatively detuned pillar (δ=-6meV) of 3.2μm side size. Columns correspond to different excitation powers (350 μW, 500 μW, 700 μW and 1000 μW from left to right) and rows to the different polarization components(ρ_L, ρ_D, ρ_C and ρ from top to bottom).

The time profiles of the three polarization components above threshold are shown alongside the overall polarization in Figure 8.13. As expected, the circular component (ρ_C) is practically zero, while the linear (ρ_L) and diagonal components (ρ_D) as well as the overall degree of polarization (ρ) exhibit strong oscillations. These oscillations can easily

be fitted with an exponential of the form

$$f(x) = y_0 + \sin(ax + \phi)\exp(\frac{-x}{\tau_c}) \tag{8.4}$$

where τ_c stands for the coherence time. The oscillation periods remain roughly the same for each component with increasing power, as shown in Figure 8.14 for the linear and diagonal component, and in Figure 8.15 for the overall polarization degree. The overall coherence time is about half of the oscillating period of that in the linear plane.

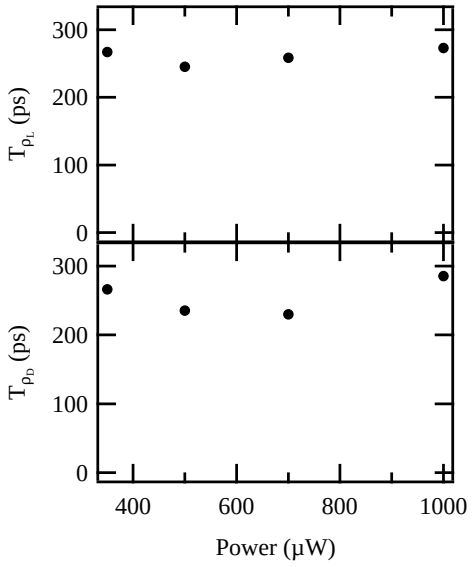

FIGURE 8.14: Coherence times of the (a) the linear and (b) the diagonal component of the emission above threshold from a negatively detuned pillar (δ=-6 meV) of 3.2 μm side size vs. excitation powers.

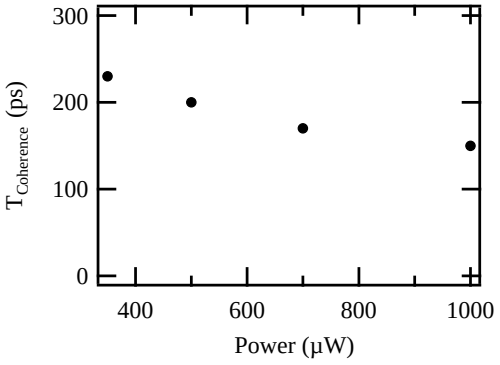

FIGURE 8.15: Coherence time of the polarization p of the emission above threshold from a negatively detuned pillar (δ=-6 meV) of 3.2 μm side size vs. excitation powers.

As stated in previous chapters, the polarisation of photoluminescence from a microcavity in the strong coupling regime is directly linked to the spin state of the polaritons when they decay, i.e. polaritons with spin-up or spin-down. Due to polariton self interaction, an imbalance in population between the spin states causes a splitting in energy, which leads to an oscillation in the linear polarisation of the photoluminescence.

The above fittings reveal an average oscillations period of 270 ps, which corresponds to an energy splitting between the two polariton states of $\approx$ 15 μeV. The blueshift of the lowest energy mode is about 6 times larger than the broadening of the mode and given the fact that it originates from the repuslive interaction of polaritons V [120], the latter can be calculated by the following formula (Equation 6.4)

$$V = 6X_h E_b a_b^2 / S = \alpha_1 + \alpha_2 \tag{8.5}$$

where E_b is the exciton binding energy, a_b the Bohr radius, X_h the excitonic fraction of the lower polariton branch and S the area of the sample. α_1 and α_2 correspond to the interaction constants for the polaritons with parallel and anti-parallel spins respectively, with $\alpha_2 < 0 < \alpha_1$ and $\alpha_1 > |\alpha_2|$ [131, 132].

The details of the sample produce a value of 9 μeV. Experimental findings in [133] regarding the measured value of the polariton interaction constant report that $V \approx 12$ μeV. These findings may raise a discussion to whether the above effect can be attributed to the inbalance of the populations of the spin up and spin down polaritons by a single polariton. The absence of polarisation oscillations in the linear regime excludes any polarisation oscillations due to the geometry of the pillars in study. Unfortunately, the data is quite inconclusive and claiming observation of an odd number of polaritons in the polarisation state of a polariton laser would require further investigation.

8.4 Theoretical discussions

The main concepts and results discussed in this section were developed by Tomáš Ostatnický. As stated above, the present hypothesis [27], attributes the wide band feature found in all pillars spectra corresponds to excitonic emission, coupled to the detection system through the side walls of the pillars. However, this only seems like a reasonable

assumption for pillars of small sizes, for which the lateral size of the pillar is important due to diffraction. As the detection is properly aligned to collect the PL only from the centre of the pillar surface only polariton emission is expected. Since the wide PL band is detected even in such large pillars, it should be ascribed to some kind of polariton modes rather than exciton which is not coupled to the detection system at all. The feature is attributed to bottleneck states. The model includes the following relaxations mechanisms (Figure 8.16):

1. exciton + exciton → exciton + polariton

2. exciton → polariton + phonon

3. exciton + exciton → polariton + polariton

Relaxation via emission of optical phonons is ruled out as it is not allowed from the energy conservation rule. Interactions via acoustic phonons are taken into account only when the energy difference between the modes allows. Although the in-plane momentum conservation rule is relaxed in exciton-phonon interaction due to the confinement effect, the bulk wave vector must be conserved during the interaction. The maximum exchanged momentum is therefore given by the size of the exciton wave function in reciprocal space, leading to the limit $q_{max} \approx 2\pi/L_z$, where L_z is the lateral size of quantum well. Inserting the value L_z=8 nm and sound speed v_s = 3.5x10ˆ5 cm/s, we get the limiting energy for exciton-phonon interaction $\Delta E_{max} = \frac{2\pi\hbar v_s}{L_z} \approx 2$ meV.

To estimate the minimum energy to which an exciton can relax via exciton-exciton scattering to an exciton and a lower polariton modes (process 1), parabolic dispersion $E(k) = \hbar^2 k^2/2m$ and Boltzmann distribution of excitons $n(k) = 2\pi k \exp(-E(k)/k_B T)$ is assumed.

Excitons with initial momenta $\boldsymbol{k}_1$ and $\boldsymbol{k}_2$ scatter to the final states with momenta 0 (polariton) and $\boldsymbol{k}_1 + \boldsymbol{k}_2$ (exciton), polariton momentum can be set zero because of the small momentum extent of the light cone compared to exciton distribution in k-space. The energy of the resulting polariton state is simply given as $E_{pol} = -\hbar^2 \boldsymbol{k}_1 \cdot \boldsymbol{k}_2/m$. To estimate the energy at which most polaritons are populated by exciton-exciton scattering, let us set $\boldsymbol{k}_1 = \boldsymbol{k}_2 = \boldsymbol{k}$. Then the number of polaritons scattered to the state with energy E_{pol} is $n_{scat}(E_{pol}) = 2n^2(\sqrt{-mE_{pol}}/\hbar)$ where we account for the density of states of the initial and final states and their thermal distribution. The maximum is where $\frac{dn_{scat}}{dE_{pol}} = 0$

and we find the result $E_{pol} = k_B T$. Assuming the temperature of exciton gas T=40 K , we get the maximum polariton population at $E_{pol} \approx$ -3.5 meV.

It has been shown that the peak polariton population due to the first two types of scattering processes lies 2–4 meV below the exciton resonance, which is expected to populate a wide band of bottleneck states below the exciton line. Although the photonic Hopfield coefficient is fairly small for the bottleneck states as they are mostly exciton-like, observation of the PL from these states should still be possible due to their nonzero magnitude.

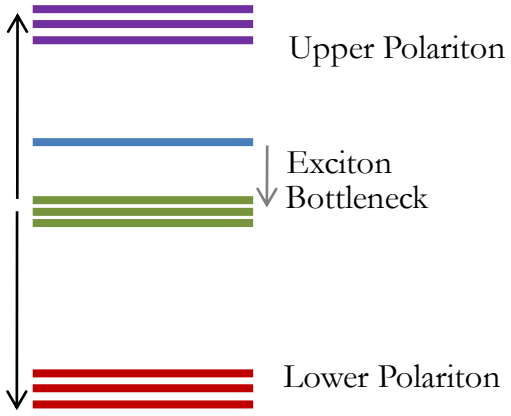

FIGURE 8.16: Level scheme for the model proposed. Parametric exciton exciton scattering to LP and UP states is depicted by black arrows, phonon emission and exciton exciton scattering to exciton + LP state is gray.

As mentioned in Chapter 8.1.2, a ladder of quantized polariton modes appears in all pillars, with a clear gap observed between the polariton and 'wide band' including the ones described above. The latter has a FWHM of 45 meV at the highest energy and is clearly resolved in all pillars, including the biggest one (10 μm), with the same relative strength compared to the polariton band. Both pillars exhibit the same temporal evolution, differing only by its magnitude. An initial rise and further mono-exponential decay is reported regarding the time dynamics, with a time constant of 800 ps.

8.4.1 Spontaneous scattering regime dynamics

The relaxation dynamics at the spontaneous regime are driven by the population of the bottom of the exciton band only, represented by a single broadened state, shown

in blue in Figure 8.16. In microcavities with one quantum well in the cavity, excitons quickly relax via phonon emission to the polariton bottleneck due to relatively strong exciton-phonon interaction. In the samples with a large number of quantum wells, on the contrary, density of exciton states at the exciton band minimum is led by dark states which do not couple to photon modes due to either spin or mode spatial symmetry. In the particular case of a microcavity with 15 quantum wells and considering only modes with spin +1, there are two polariton modes and 14 'dark' exciton modes. Interaction with phonons cannot couple dark excitons to polaritons leading to depopulation of the bottom of exciton band and therefore the existence of dark states opens a way for parametric exciton-exciton processes which simultaneously populate the upper and the lower poalriton band.

In the model, a rectangular pillar with lateral dimensions l_x and l_y is considered. The resonance energy of the bare cavity at normal incidence is $\hbar\omega_{cav} = \hbar c k_{cav}$. The pillar photon modes must satisfy resonance condition and are characterized by the 3D wave vector ($\frac{\pi m}{l_x}$, $\frac{\pi n}{l_y}$, $k_c av$) where the positive integer indexes m and n ambiguously define the particular mode. The mode energy can be evaluated as $E_{m,n} = \hbar\sqrt{\omega_{cav}^2 + c^2\pi^2\left(\frac{m^2}{l_x^2} + \frac{n^2}{l_y^2}\right)}$. Each of the modes then couple to the exciton modes and forms a discrete polariton energy level and is fully characterized by the indexes n, m, spin, and upper/lower index. We can assign hopfield coefficients, lifetimes and linewidths to all discrete polariton modes. The population of a lower polariton mode with indexes (M, N) due to spontaneous exciton-exciton scattering is:

$$n_{ex-ex}(N,M) \propto \int dE_1 \int dE_2 n(E_1) n(E_2) \sum_{n,m} \delta(E_1 + E_2 - E(m,n) - E(M,N)) C_x(M,N) C_x(m,n) / [w(m,n) w(M,N)], \quad (8.6)$$

where we integrate over exciton energies. $n(E)$ is the exciton population at energy E and the summation goes over all upper polariton states. The variable C_x is the Hopfield coefficient and w stands for linewidth of the appropriate polariton state. The delta-function ensures energy conservation in the parametric process in which two excitons are scattered to two polaritons, one being in the upper and the other in the lower polariton band.

The model can be further improved accounting for phase shifts of photons at pillar/air

boundaries during their total internal reflection. This is, however, a non-analytical problem and involves a numerical solution. As a result, originally twice degenerate modes split and we observe complex multiple peak structure in the experimental data. Besides the exciton-exciton scattering, there is the relaxation process which involves phonon emission. The population of the mode (M,N) due to phonon emission has been modeled using the formula

$$n_{ex-ph}(N,M) \propto \int dEn(E)C_x(m,n)W_{ph}(E - E(M,N))/w(M,N) \tag{8.7}$$

where the function W_{ph} describes dependence of phonon scattering amplitude on exchanged energy. In the calculations,the approximative Gaussian profile

$$W_{ph}(E) \propto exp\left(-\frac{E^2L_z^2}{(2\pi)^2}\right) \tag{8.8}$$

was used.

The model successfully predicts the exact energies of the polariton modes as well as the wide band energy, for all pillars under study. Results for pillars of various sizes and detunings can be seen in 8.17. The green line depicts the exciton position, E_x. The photon modes were calculated via wave optics, taking full account of the TE–TM splitting and some anisotropy in the pillar sizes.

8.4.2 Stimulated scattering regime dynamics

Although the data from the spontaneous scattering regime shows onset and mono-exponential decay, the behaviour in the stimulated regime is completely different. The temporal dynamics shorten as the pump power increases and exhibit strongly non-exponential behaviour implying relaxation dynamics stimulated by the populations of the polariton states. Depending on the pillar size and/or detuning, the modes reveal oscillating behaviour or interchange order in maximum intensity. The behaviour of the modes in the nonlinear regime requires that the blueshift of the exciton resonance as well as possible parametric scattering processes are taken into account. The latter was thoroughly exploited in Chapter 8.2, in an attempt to explain the observation of non ground state condensation. The exciton blueshift renormalizes the strength of the exciton-exciton interaction between the modes and the exciton bath, affecting their intensity. The above

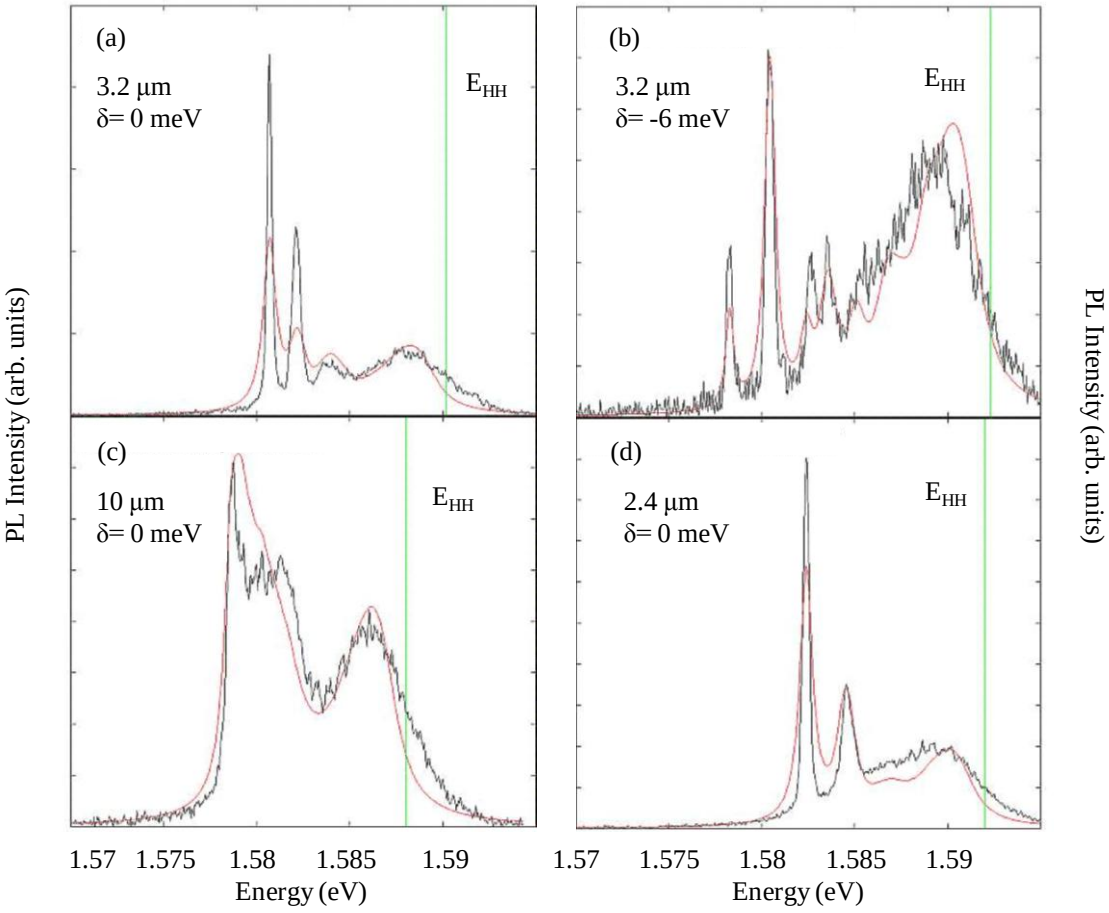

FIGURE 8.17: Theoretical fits of the PL curves for (a) a 3.2 μm pillar, at zero detuning, (b) a 3.2 μm pillar, detuned at -6meV, (c) a 10 μm pillar, at zero detuning and (d) a 2.4 μm pillar, at zero detuning.

is obvious for e.g. a 6 μm size pillar at zero detuning, where the visibility of the modes is much dependent on the input pump power (Figure 8.18). Theoretical simulations of the PL spectra from this pillar as the blueshift increases are shown in Figure 8.19, underlining the importance of this parameter in modeling the micropillars' dynamics.

8.4.3 Discussion

The experimental data reveals features which were expected: occurrence of discrete polariton modes and their interplay in the dynamics. A detailed study of the whole set of data proves that the assumptions in theoretical models to date are not sufficient to predict the observed spectral and temporal behaviour. The interactions of the lower polariton modes, upper polariton band, the bottleneck modes and the exciton bath turn out to be of utmost importance. As phonon-assisted relaxation mechanisms are forbidden

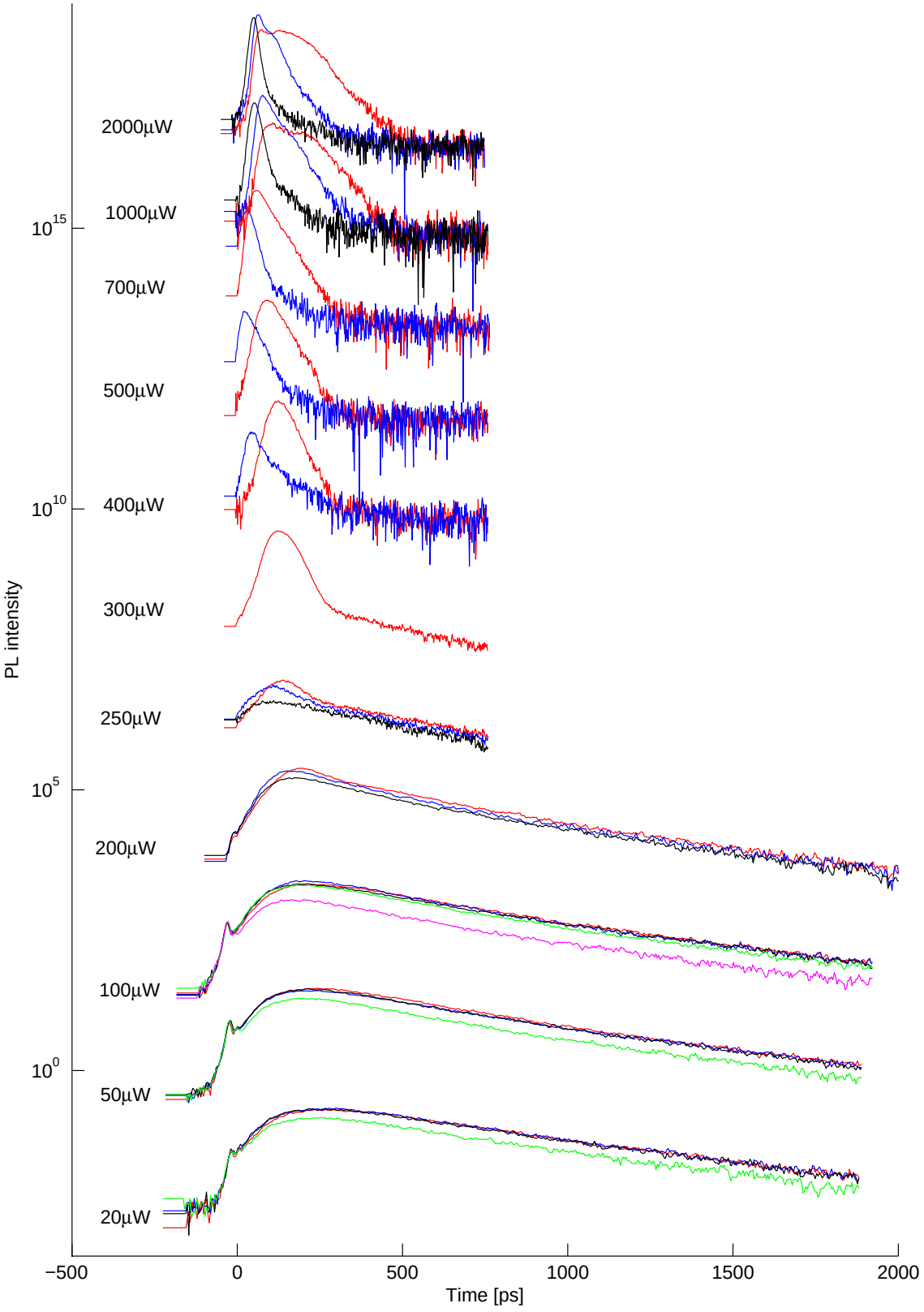

FIGURE 8.18: Dynamics of the visible modes of a 6 μm size pillar at zero detuning at various pump intensities.

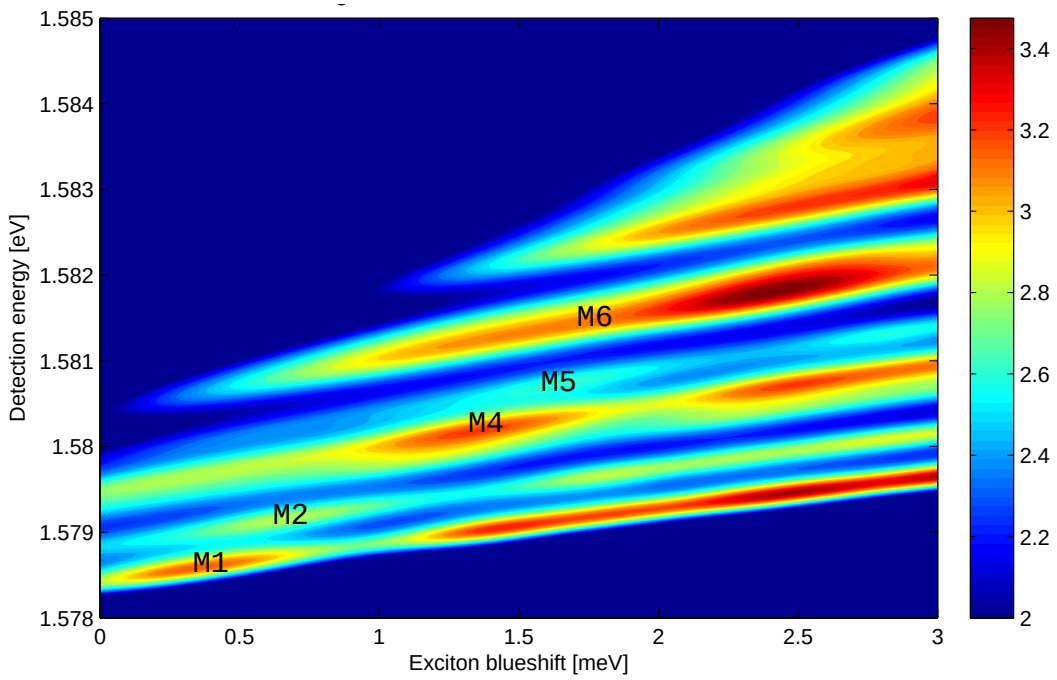

FIGURE 8.19: Calculated PL spectra of a 6 μm size pillar at zero detuning, depending on the blueshift of exciton resonance due to exciton-exciton interactions.

in most of the pillars under study due to the large inter-level splittings, exciton-exciton interactions seem to determine the dynamics in 0D cavities, an observation in contrast with the dynamics in 2D structures.

8.5 Conclusions

In this chapter, the temporal and spatial dynamics of polariton condensates occuring in zero dimensional microcavities have been presented. The broken translational invariance facilitates the formation of a condensate as the wavevector conservation rule no longer applies to the system. Interesting observations such as bizarre polarization findings or the formation of non ground state polariton condensation have been analysed separately, with theoretical explanation of the latter based on a simple kinetic model, where the interplay of exciton-exciton and pair polariton interactions accounts for this peculiar observation. A complete theoretical model including various relaxation mechanisms that can fit spectra from pillars of various sizes and detunings is developed. The wide band mode at higher energies is attributed to bottleneck states and not to uncoupled exciton states, as the literature suggests. The above confirms that the reduction in dimensionality

of the cavities influences not only the polariton mode spectrum but also the dynamics involved, rendering polariton studies in such systems extremely interesting.

Chapter 9

Conclusions

The work presented in this thesis investigated the spatial and temporal properties of polariton condensation, occuring in zero- and two-dimensional structures, as well as the origin of the so called spin Hall effect recently realized in semiconductor microcavity. The polaritons are the superposition of trapped excitons in quantum wells and confined cavity photons and inherit therefore properties stemming from light and matter. Their uniqueness lies in their peculiar shaped energy dispersion, which results in a very light effective mass and acts as a thermodynamic trap. As a result, they are ideal candidates for Bose Einstein condensation and polariton lasing, both effects based on their bosonic character. The exploration of fundamental physics as well as the potential for technological applications have been driving polariton related research since the discovery of these unique particles in 1992.

Although GaAs was the material of choice for the community, its low exciton density prevented initially the observation of the above phenomena. Improved manufacturing techniques allowed for the achievement of polariton condensation under pulsed, non resonant excitation first in 0D microcavities and then in a 2D structure, both described in this thesis. Etching of planar samples to micropillars lifted the need for wavevector conservation in polariton relaxation and allowed for ground and non ground state polariton condensates to form. The key for condensation in a planar cavity was the excess number of quantum wells, inserted in the centre and first antinodes of the electromagnetic field within the cavity.

The polariton dynamics in both cases were studied spatially and temporally, revealing important issues of the relaxation mechanisms. The switching between ground and non ground state condensation was explained by the use of a simple kinematic model, based on the interplay of exciton-exciton and pair polariton scattering mechanisms. A complete theoretical model, developed by Tomáš Ostatnický proposes significant correction to the to date theoretical treatment of confined polaritons. Several aspects of the polariton condensation in the planar structure have been studied, including the transition from weak to strong coupling in the time domain.

As mentioned above, several efforts have been focused on the development of electrically injected polariton lasers, with their operation limited however in the linear regime. In this thesis, the role of the LO phonons as a potential relaxation mechanism to overcome the bottleneck has been proposed and studied. Resonant injection of carriers with the light hole exciton allows for carriers to accumulate in the middle polariton bottleneck, acting as a reservoir that feeds the $k = 0$ state. When the energy difference between the reservoir and the lowest polariton state coincides with the E_{LO}, polaritons relax rapidly and form a condensate. Evidence including the reduction of the threshold of the non linear regime, suggest that the LO phonons mechanism can prove extremely useful in the creation of the first electrically pumped polariton laser.

Despite the rich experimental potential of polaritons for exploration of fundamental quantum physics phenomena, they don't cease to be composite particles, with inherited photon and excitonic properties. This thesis includes investigation of the true origin of the so called spin Hall effect, recently observed in a semiconductor microcavity. Obtainment of similar results in the absence of any active material in the cavity suggests that the photonic part of polaritons drives the effect. The results are explained on the basis of linear optics, underlining the realization of the effect in a much more simplified system.

9.1 Future work

The field of polaritons is still driven by the development of low threshold electrical lasing devices and study of transportation phenomena occuring in microcavities. Both spring from the well established ability of polaritons to condense. However, both research paths have still a long way to go. Polaritons have yet to be proven that they can condense

after the electrical injection of carriers. The work presented in this thesis suggests the exploitation of the LO phonons relaxation mechanism but of course, this simplified idea needs to proven, as the evidence presented here origin from optical excitation conditions.

The polaritons' BEC character has been proven under non resonant excitation, with evidence included in chapters of this thesis, and has allowed for the very exotic observation of half-integer vortices and superfluidity. Several aspects, like superfluidity under non resonant excitation conditions have yet to be established. Nevertheless, a plethora of other possible effects have attracted the community' s interest, as the combination of their bosonic character with various spin mechanisms occuring in microcavities has opened new research doors for the field. Optical logical gates, spin memory elements and polariton neurons are for the moment only theoretical suggestions, congesting an intense relevant experimental activity.

For some though, polaritons still seem to be nothing but photons or excitons in disguise. Their photonic or excitonic character is always present, as shown with the realisation of the optical spin Hall effect in a bare photonic cavity, described in this thesis. Nevertheless, it seems they have kept only the best qualities of each character, rendering themselves truly unique.

Appendix A

Time-dependent perturbation theory and Fermi's golden rule

Fermi's golden rule is used to calculate transition rates. The result is obtained by applying the time dependent perturbation theory to a system that undergoes a transition from an initial state m to a final state k, that is part of a continuum of states. A detailed derivation of the scattering and decay time, based on Fermi's golden rule can be found in [134, 135].

Assuming the system is described by the Hamiltonian H

$$H\psi = i\hbar\frac{\partial}{\partial t}\psi, \tag{A.1}$$

where $H = H_0 + H'$ is the unperturbed Hamiltonian, whose eigenfunctions ψ_n are known and H' is the time dependent perturbation. The eigenfunctions satisfy the following conditions:

$$H_0\psi_n = E_n\psi_n \tag{A.2}$$

$$\langle\psi_a|\psi_b\rangle = \delta_{ab} \tag{A.3}$$

where the Dirac notation implies integration over continuous variables and summation over discrete variables. In this context, δ_{ab} represents a Kronecker delta-function for discrete variables and a Dirac delta function for continuous variables.

By expressing the solution to (A.1) as a sum over eigenstates of H_0 with the time-dependent coefficients:

$$\psi(t) = \sum_n a_n(t)\psi_n \exp(-iE_n t/\hbar) \tag{A.4}$$

Combining (A.1), (A.2) and (A.4), we obtain a Schrödinger equation equivalent, expressed in terms of the coefficients $a_n(t)$.

$$i\hbar \frac{da_k(t)}{dt} = \sum_n H'_{kn} a_n(t) \exp(i\omega_{kn} t) \tag{A.5}$$

where the matrix element $H'_{kn} = \langle \psi_k | H'(t) | \psi_n \rangle$ and $\hbar\omega_{kn} = E_k - E_n$.

As a first approximation, the system is assumed to be initially in the state m, in which case, $a_n^0(t) = \delta_{nm}$ and

$$i\hbar a_k^{(1)}(t) = \int_\infty^t dt' H'_{km}(t') \exp(i\omega_{km} t') \tag{A.6}$$

Assuming that the perturbing force described by H_0 'turns on' at $t = 0$ and is constant over the interval $0 \leq t' \leq t$, Equation (A.6) can be integrated to give:

$$i\hbar a_k^{(1)}(t) \approx 2H'_{km}(t) \exp(i\omega_{km} t/2) \left(\frac{\sin \omega_{km} t/2}{\omega_{km}} \right) \tag{A.7}$$

Assuming $a_k(t) \approx a_k^{(1)}(t)$, the probability $P_k(t)$ that the system undergoes a transition from state m to state k is:

$$P_k(t) = |a_k(t)|^2 \approx \frac{4|H'_{km}|^2}{\hbar^2} \frac{\sin^2 \omega_{km} t/2}{\omega_{km}^2} \tag{A.8}$$

The number of possible transition states dn within an interval $d\omega_{km}$ can be written:

$$dn = \rho(k) dE_k \tag{A.9}$$

where $\rho(k) = dn/dE_k$ is the density of states per unit energy interval near E_k. $\rho(k)$ and H'_{km} are smoothly varying functions of momentum or energy near the state k. The meaningful quantity though is the total transition rate to states near the state k:

$$W_k = \frac{1}{t} \sum_{k' near\, k} P_{k'}(t) \tag{A.10}$$

which can be replaced by an integral over dE_k:

$$\begin{aligned} W_k &= \frac{1}{t}\sum P_{k'}(t)\rho(k')dE_{k'} \\ &= \sum dE_k\rho(k)\frac{4|H'_{km}|^2}{\hbar^2}\frac{1}{t}\left(\frac{\sin^2\omega_{km}t/2}{\omega_{km}^2}\right) \\ &= \frac{4}{\hbar}|H'_{km}|^2\rho(k)\int_{-\infty}^{\infty}d\omega\frac{1}{t}\left(\frac{\sin^2\omega t/2}{\omega^2}\right) \end{aligned} \tag{A.11}$$

As the last integral's value is $\pi/2$, Fermi's golden rule is obtained:

$$W_k = \frac{2\pi}{\hbar}|H'_{km}|^2\rho(k) \tag{A.12}$$

Appendix B

Transfer Matrix Method

The transfer-matrix method is a general technique for solving problems in statistical mechanics. It is used when the total system can be broken into a sequence of subsystems that interact only with adjacent subsystems. The simplest case in which the Transfer Matrix Method can be applied is the propagation of a light wave in a medium characterised by a refractive index n_1 and thickness l, between two layers of medium with refractive indices n_0 and n_t respectively.

The boundary conditions require that the electric field and its derivative are both continuous, therefore at the first interface

$$E_0 + E_r = E_1 + E_1' \tag{B.1}$$

$$n_0 E_0 + n_0 E_r = n_1 E_1 - n_1 E_1' \tag{B.2}$$

where E_0 and E_0 correspond to the propagating waves in the media with refractive indices n_0 and n_1 respectively. E_r and E_1^1 correspond to their partially reflected waves respectively. At the second interface

$$E_1 e^{ik_l l} + E_1' e^{-ik_l l} = E_t \tag{B.3}$$

$$n_1 E_1 e^{ik_l l} - n_1 E_1' e^{-ik_l l} = n_t E_t \tag{B.4}$$

with $k_l = \frac{2\pi}{\lambda} = \frac{2\pi n_l}{\lambda_0}$. Elimination of the E_1 and E_1' leads to

$$1 + \frac{E_0'}{E_0} = \left(\cos(k_l l) - i\frac{n_t}{n_l}\sin(k_l l)\right)\frac{E_t}{E_0} \tag{B.5}$$

$$n_0 - n_0\frac{E_0'}{E_0} = \left(-in_l\sin(k_l l) + n_t\cos(k_l l)\right)\frac{E_t}{E_0} \tag{B.6}$$

In matrix form, the above equation becomes

$$\begin{bmatrix}1\\ n_0\end{bmatrix} + \begin{bmatrix}1\\ -n_0\end{bmatrix}\frac{E_0'}{E_0} = \begin{bmatrix}\cos(k_l l) & -\frac{i}{n_l}\sin(k_l l)\\ -in_l\sin(k_l l) & \cos(k_l l)\end{bmatrix}\begin{bmatrix}1\\ n_t\end{bmatrix}\frac{E_0'}{E_0} \tag{B.7}$$

And it gets further more simplified with the reflection coefficient $r = \frac{E_0'}{E_0}$ and the transmission coefficient $t = \frac{E_t}{E_0}$

$$\begin{bmatrix}1\\ n_0\end{bmatrix} + \begin{bmatrix}1\\ -n_0\end{bmatrix} r = M\begin{bmatrix}1\\ n_t\end{bmatrix} t \tag{B.8}$$

In the case of a multilayer structure with refractive indices $n_1, n_2, n_3, .., n_N$ and thicknesses $I_1, I_2, I_3, .., I_N$, the above equation becomes

$$\begin{bmatrix}1\\ n_0\end{bmatrix} + \begin{bmatrix}1\\ -n_0\end{bmatrix} r = \begin{bmatrix}1+r\\ n_0(1-r)\end{bmatrix} = M_1 \cdot M_2 \cdot M_3 \cdot \ldots M_N \begin{bmatrix}1\\ n_t\end{bmatrix} t = M\begin{bmatrix}1\\ n_t\end{bmatrix} t \tag{B.9}$$

where $M_1 \cdot M_2 \cdot M_3 \cdot \ldots M_N = \begin{bmatrix}A & B\\ C & D\end{bmatrix}$. By defining the elements of the matrix as A, B, C and D, we can derive the reflection and transmission coefficients as

$$r = \frac{A \cdot n_0 + B \cdot n_0 \cdot nt - C - D \cdot n_t}{A \cdot n_0 + B \cdot n_0 nt + C + D \cdot n_t} \tag{B.10}$$

$$t = \frac{2n_0}{A \cdot n_0 + B \cdot n_0 \cdot nt + C + D \cdot n_t} \tag{B.11}$$

The reflectance and transmittance are given by $R = |r|^2$ and $T = |t|^2$. In the oblique incidence case, the above calculated transfer matrix keeps its form provided the following substitutions are made:

$$k_z = k \cdot \cos\varphi \tag{B.12}$$

$$n \to n \cdot \cos\varphi \tag{B.13}$$

where φ is the propagation angle in the corresponding medium. Note that at any two propagation angles φ_i and φ_j in layers with refractive indices n_i and n_j are linked by Snell' s law:

$$n_i \cdot \sin\varphi_i = n_j \cdot \sin\varphi_j \tag{B.14}$$

Appendix C

Programming codes in Igor Pro

The following appendix includes excerpts of codes written in Igor Pro, regarding useful calculations of mcrocavity properties.

C.1 Transfer matrix method

Declaration of variables, lo=central wavelength and moires=degrees. Default calculation is for a cavity of 24 (27) layers for the Bragg mirrors in the top (bottom) and a substrate of 200 μm.

```
variable theta, no, nt, n1, n2,ns, ns2, lo,ls, ls2, M,N,L, th, l11, l22, br1, br2, n3, n4, l33, l44, l3, l4, O, P, moires  moires=0

Prompt moires, "Enter theta "
DoPrompt "Enter mc specifications for the angle", moires
if (V_Flag)
return -1 //User canceled
endif

theta=pi*moires/180
```

`no=1*cos(theta)` before sample (outside front)

`nt=1` after substrate(outside sample)

`ns=3.55*cos(asin(sin(theta)/3.3))` substrate

`n1=3.55*cos(asin(sin(theta)/3.3))` refractive index of layer1

`n2=2.94*cos(asin(sin(theta)/2.86))` refractive index of layer 2

n3=3.55*cos(asin(sin(theta)/3.3)) QW

l11=59.8, l22=72.2, l33=239.2 in nm

br1=24 how many pairs for mirror1

br2=27 how many pairs for mirror2

ls=200 layer thickneses of substrate

M=2*pi*n1*l11*cos(asin(sin(theta)/3.3)) constant ki*l without devided by lamda running for layer 1 (bragg)

N=2*pi*n2*l22*cos(asin(sin(theta)/2.86)) for layer 2 (bragg)

L=2*pi*ns*ls*cos(asin(sin(theta)/3.3)) for substrate

P=2*pi*n3*l33*cos(asin(sin(theta)/3.3)) constant $k_i * l$ for cavity spacer

variable i=0, mm=0

Make/d/o/n=(15000,4) xRTvalues column 0: lamda, column 1: reflectance, column 2: transmitance

Setscale/p x (780),(0.01),xRTvalues

xRTvalues[][0]=x

Do

Make/o/c mat1={{0,0},{0,0}} layer n1

Make/o/c mat2={{0,0},{0,0}} layer n2

Make/o/c mat3={{0,0},{0,0}} substrate

Make/o/c mat4={{0,0},{0,0}} Total Matrix

Make/o/c mat5={{0,0},{0,0}} first mirror

Make/o/c mat6={{0,0},{0,0}} second mirror

Make/o/c mat7={{0,0},{0,0}} mat1xmat2

Make/o/c mat8={{0,0},{0,0}} mat2xmat1

Make/o/c mat10={{0,0},{0,0}} cavity spacer

Make/o matA= {{cos(M / (xRTvalues[i][0])),0},{0,cos(M / (xRTvalues[i][0]))}} real part of layer 1(mat1)

Make/o matB= {{0,(1 / n1)*sin(M / (xRTvalues[i][0]))},{ n1*sin(M / (xRTvalues[i][0])),0}} imaginary part of layer 1(mat1)

Make/o matC={{cos(N / (xRTvalues[i][0])),0},{0,cos(N/ (xRTvalues[i][0]))}} real part of layer 2(mat2)

Make/o matD={{0,(1 / n2) *sin(N / (xRTvalues[i][0]))},{n2*sin(N / (xRTvalues[i][0])),0}} imaginary part of layer 2(mat2)

Make/o matE={{cos(L / (xRTvalues[i][0])),0},{0,cos(L/ (xRTvalues[i][0]))}} real part of substrate matrix

Make/o matF={{0,(1 / ns)*sin(L / (xRTvalues[i][0]))},{ns*sin(L / (xRTvalues[i][0])),0}} imaginary part of substrate matrix

Make/o matI={{cos(P / (xRTvalues[i][0])),0},{0,cos(P/ (xRTvalues[i][0]))}} real part of cavity spacer matrix

Make/o matJ={{0,(1 / n3)*sin(P / (xRTvalues[i][0]))},{n3*sin(P / (xRTvalues[i][0])),0}} imaginary part of cavity spacer matrix

mat1=matA - cmplx(0,1)*matB transfer matrix of layer 1

mat2=matC - cmplx(0,1)*matD transfer matrix of layer 2

mat3=matE - cmplx(0,1)*matF transfer matrix of substrate

mat10=matI - cmplx(0,1)*matJ transfer matrix of cavity spacer

for the first mirror

MatrixMultiply mat1,mat2 M_product=mat1 x mat2= transfer matrix of layer 1and layer 2 (1stack)

```
Duplicate/o/c M_product, mat_7
variable ii=1
do
if (ii > (br1-1))
break
endif
MatrixMultiply M_product,mat_7
ii += 1
while(1)
Duplicate/o/c M_product,mat5// single mirror starting with high ending with low
```

for the second mirror

MatrixMultiply mat2,mat1 M_product=mat2 x mat1= transfer matrix of layer 2 and layer 1

```
Duplicate/o/c M_product, mat_8
ii=1
do
if (ii > (br2-1))
break
endif
MatrixMultiply M_product,mat_8
ii += 1
```

```
while(1)

Duplicate/o/c M_product,mat6//single mirror starting with low ending with high

for the whole structure

MatrixMultiply mat5,mat10,mat6,mat3 Bragg1, cavity spacer, Bragg2, substrate

Duplicate/o/c M_product,mat4

Make/d/o/n=(2,4) aux more compact expressions for the auxilliary wave

aux[1][0]=(real (mat4[0][0])* no + real (mat4[0][1]) *no*nt -real (mat4[1][0]) -real (mat4[1][1]) * nt)

aux[0][1]=(imag (mat4[0][0]) * no + imag (mat4[0][1]) *no*nt - imag (mat4[1][0]) -imag (mat4[1][1]) * nt)

aux[0][0]=(real (mat4[0][0])* no + real (mat4[0][1]) *no*nt +real (mat4[1][0]) +real (mat4[1][1]) * nt)

aux[1][1]=(imag (mat4[0][0]) * no + imag (mat4[0][1]) *no*nt + imag (mat4[1][0]) +imag (mat4[1][1]) * nt)

aux[0][2]=(aux[1][0] * aux[0][0]+ aux[0][1] * aux[1][1])

aux[1][2]= ( aux[0][1] * aux[0][0] - aux[1][0] * aux[1][1] )

aux[1][3]=(((aux[0][0])^2)+(aux[1][1]^2))

xRTvalues[i][1]= ((aux[0][2]/aux[1][3])^2) + ((aux[1][2]/aux[1][3])^2) reflectance

xRTvalues[i][2]=((2*no*aux[0][0]/aux[1][3])^2) +((2*no*aux[1][1]/aux[1][3])^2) transmitance

i +=1

while(i<(dimsize(xRTvalues,0)))

mm=0

Do

xRTvalues[mm][3]= 1240/xRTvalues[p][0]

mm+=1

while(mm<(dimsize(xRTvalues,0)))


display/k=1 xRTvalues[][1]

End
```

C.2 Rate equations

The following code was used to calculate the populations of polariton modes in a pillar, where non ground state condensation was observed (Chapter 8.2.3). It requires solving

4 coupled rate equations between the exciton reservoir of population N_0, and three polariton modes of populations N_1, N_2 and N_3, with nymbering beginning from the lowest energy state.

```
Function PopDynamics5(w, tt, y, dydt)
Wave w pw[0] = k1, pw[1] = k2, pw[2] = k3
Variable tt time value at which to calculate derivatives
Wave y
Wave dydt wave to receive dNx/dt, dNs/dt etc. (output)
Variable E1=1.5735
Variable E2=1.5755
Variable E3=1.5791
Variable Ex=1.5892
Variable Kb=0.000861734
Variable p=(w[7]*exp(-((tt-w[10])/0.150)^2/2) pump

Variable B1=exp(-(Ex-E3)/ Kb)+1
Variable B2=exp(-(Ex-E2)/ Kb)+1
Variable B3=exp(-(Ex-E1)/ Kb)+1
Variable B4=exp(-(E2-E1)/ Kb)+1
Variable B5=exp(-(E3-E1)/ Kb)+1
Variable B6=exp(-(E3-E2)/ Kb)+1

Variable X=0.1622
Variable Q=0.238733
Variable Z=0.3497

dydt[0]=(-w[0]*w[9]*y[0]-w[4]*(w[9]*y[0])^2*(w[9]*X*y[1]+1)-
-w[5]*(w[9]*y[0])^2*(w[9]*Q*y[2]+1)-w[6]*(w[9]*y[0])^2*(w[9]*Z*y[3]+1)+
+p+w[11]*((w[9]*Z*y[3])^2*(w[9]*y[0]/w[12]+1)*(w[9]*X*y[1]+1)-
-w[9]^2*X*y[1]*y[0]/w[12]*(w[9]*Z*y[3]+1)^2))/w[9]

dydt[3] = (-w[3]*w[9]*y[3]+ w[6]*(w[9]*y[0])^2*(w[9]*Z*y[3]+1)-
-2*w[11]*((w[9]*Z*y[3])^2*(w[9]*y[0]/w[12]+1)*(w[9]*X*y[1]+1)-
-w[9]^2*X*y[1]*y[0]/w[12]*(w[9]*Z*y[3]+1)^2))/w[9]

dydt[2] = (-w[2]*w[9]*y[2]+ w[5]*(w[9]*y[0])^2*(w[9]*Q*y[2]+1))/w[9]
```

```
dydt[1] = (-w[1]*w[9]*y[1]+ w[4]*(w[9]*y[0])^2*(w[9]*X*y[1]+1)+
+w[11]*((w[9]*Z*y[3])^2*(w[9]*y[0]/w[12]+1)*(w[9]*X*y[1]+1)-
-w[9]^2*X*y[1]*y[0]/w[12]*(w[9]*Z*y[3]+1)^2))/w[9]
End

Function RunPopDynamics5()
Make/D/O/N=(1800,4) PopDyn
Make /O errScale={1e-10,1e-10,1e-10,1e-10}
SetScale/P x 0,1,PopDyn calculate concentrations every 10 fs (times are in ps)
SetDimLabel 1,0,Nx,PopDyn
SetDimLabel 1,1,Ns1,PopDyn
SetDimLabel 1,2,Ns2,PopDyn
SetDimLabel 1,3,Ns3,PopDyn
PopDyn[0][%Nx] = 0 initial conditions: population of exciton reservoir
PopDyn[0][%Ns1] = 0
PopDyn[0][%Ns2] = 0
PopDyn[0][%Ns3] = 0
Make/D/O/N=18 KK rate constants
variable i=1

Do

KK[0]=0.001 inverse of exciton lifetime in ps (1 ns)
KK[1]=0.032 inverse of Ns1 lifetime in ps (22.7 ps)
KK[2]=0.031 inverse of Ns2 lifetime in ps (23 ps)
KK[3]=0.0305 inverse of Ns3 lifetime in ps (24 ps)
KK[4]=0.0000004 Coupling of X to Ns1 (Xh=0.162198)
KK[5]=0.0000004 Coupling of X to Ns2 (Xh=0.238733)
KK[6]=0.0000004 Coupling of X to Ns3 (Xh=0.3497)
KK[7]=0+500*i pulse intensity
KK[8]=0.0000000051 acoustic scattering between all polariton states
KK[9]=13 Constant for population -> streak intensity
KK[10]=50 t0
KK[11]=0.0000071 pair scattering constant
KK[12]=25 Exciton ratio to participate in the pair scattering
```

```
IntegrateODE /M=0/E =1e-10 /S=errScale /F=(1+2+4+8) /U=1e+2 PopDynamics5, KK, PopDyn

print kk[7]

i=i+1

while (i＜10000)

End
```

Bibliography

[1] R. N. Hall, G. E. Fenner, J. D. Kingsley, T. J. Soltys, and R. O. Carlson. Coherent light emission from GaAs junctions. *Phys. Rev. Lett.*, 9(9):366–368, 1962.

[2] H. Soda, K. Iga, C. Kitahara, and Y. Suematsu. GaInAsP/InP surface emitting injection lasers. *Japanese Journal of Applied Physics*, 18(12):2329–2330, 1979.

[3] H. F. Hess, E. Betzig, T. D. Harris, L. N. Pfeiffer, and K. W. West. Near-Field Spectroscopy of the Quantum Constituents of a Luminescent System. *Science*, 264 (5166):1740–1745, 1994. doi: 10.1126/science.264.5166.1740.

[4] D. Bimberg, M. Grundmann, and N. N. Ledentsov. Quantum dot heterostructures. *Wiley*, 1999.

[5] C. Weisbuch, M. Nishioka, A. Ishikawa, and Y. Arakawa. Observation of the coupled exciton-photon mode splitting in a semiconductor quantum microcavity. *Physical Review Letters*, 69(23):3314, 1992.

[6] J. J. Hopfield. Theory of the contribution of excitons to the complex dielectric constant of crystals. *Phys. Rev.*, 112(5):1555–1567, 1958.

[7] A. Imamoglu, R. J. Ram, S. Pau, and Y. Yamamoto. Nonequilibrium condensates and lasers without inversion: Exciton-polariton lasers. *Physical Review A*, 53(6): 4250, 1996.

[8] P. G. Savvidis, J. J. Baumberg, R. M. Stevenson, M. S. Skolnick, D. M. Whittaker, and J. S. Roberts. Angle-resonant stimulated polariton amplifier. *Physical Review Letters*, 84(7):1547, 2000.

[9] D. Porras and C. Tejedor. Linewidth of a polariton laser: Theoretical analysis of self-interaction effects. *Physical Review B*, 67(16):161310, 2003.

[10] G. Malpuech, A. Kavokin, A. Di Carlo, and J. J. Baumberg. Polariton lasing by exciton-electron scattering in semiconductor microcavities. *Phys. Rev. B*, 65(15): 153310, 2002.

[11] S. N. Bose. *Z. Phys.*, 26(178), 1924.

[12] A. Einstein. *Sitzungberichte, Pressische Akademie der Wissenshaften*, 1:3, 1925.

[13] E. A. Cornell and C. E. Wieman. Nobel lecture: Bose-Einstein condensation in a dilute gas, the first 70 years and some recent experiments. *Rev. Mod. Phys.*, 74(3): 875–893, 2002.

[14] M. H. Anderson, J. R. Ensher, M. R. Matthews, C. E. Wieman, and E. A. Cornell. Observation of Bose-Einstein Condensation in a Dilute Atomic Vapor. *Science*, 269(5221):198–201, 1995.

[15] J. M. Blatt, K. W. Böer, and W. Brandt. Bose-Einstein condensation of excitons. *Phys. Rev.*, 126(5):1691–1692, 1962.

[16] S. A. Moskalenko. Reversible optico-hydrodynamic phenomena in a non ideal exciton gas. *Soviet Physics Solid State*, 4:199.

[17] R. Houdré, J. L. Gibernon, P. Pellandini, R. P. Stanley, U. Oesterle, C. Weisbuch, J. O'Gorman, B. Roycroft, and M. Ilegems. Saturation of the strong-coupling regime in a semiconductor microcavity: Free-carrier bleaching of cavity polaritons. *Phys. Rev. B*, 52(11):7810–7813, 1995.

[18] M. S. Skolnick, R. M. Stevenson, A. I. Tartakovskii, R. ButtÃľ, M. Emam-Ismail, D. M. Whittaker, P. G. Savvidis, J. J. Baumberg, A. Lemaître, V. N. Astratov, and J. S. Roberts. Polariton-polariton interactions and stimulated scattering in semiconductor microcavities. *Materials Science and Engineering: C*, 19(1-2):407 – 416, 2002.

[19] P. Senellart, J. Bloch, B. Sermage, and J. Y. Marzin. Microcavity polariton depopulation as evidence for stimulated scattering. *Physical Review B*, 62(24):R16263, 2000.

[20] A. I. Tartakovskii, M. Emam-Ismail, R. M. Stevenson, M. S. Skolnick, V. N. Astratov, D. M. Whittaker, J. J. Baumberg, and J. S. Roberts. Relaxation bottleneck

and its suppression in semiconductor microcavities. *Physical Review B*, 62(4): R2283, 2000.

[21] J. Kasprzak, M. Richard, S. Kundermann, A. Baas, P. Jeambrun, J. M. J. Keeling, F. M. Marchetti, M. H. Szymanska, R. André, J. L. Staehli, V. Savona, P. B. Littlewood, B. Deveaud, and Le Si Dang. Bose-Einstein condensation of exciton polaritons. *Nature*, 443(7110):409–414, 2006.

[22] S. Christopoulos, G. Baldassarri Hoger von Hogersthal, A. J. D. Grundy, P. G. Lagoudakis, A. V. Kavokin, J. J. Baumberg, G. Christmann, R. Butte, E. Feltin, J. F. Carlin, and N. Grandjean. Room-temperature polariton lasing in semiconductor microcavities. *Physical Review Letters*, 98(12):126405–4, 2007.

[23] D. Sanvitto, D. N. Krizhanovskii, D. M. Whittaker, S. Ceccarelli, M. S. Skolnick, and J. S. Roberts. Spatial structure and stability of the macroscopically occupied polariton state in the microcavity optical parametric oscillator. *Physical Review B (Condensed Matter and Materials Physics)*, 73(24):241308–4, 2006.

[24] M. Richard, J. Kasprzak, R. Romestain, R. André, and Le Si Dang. Spontaneous coherent phase transition of polaritons in CdTe microcavities. *Physical Review Letters*, 94(18):187401, 2005.

[25] R. Balili, V. Hartwell, D. Snoke, L. Pfeiffer, and K. West. Bose-Einstein condensation of microcavity polaritons in a trap. *Science*, 316(5827):1007–1010, 2007.

[26] S. Utsunomiya, L. Tian, G. Roumpos, C. W. Lai, N. Kumada, T. Fujisawa, M. Kuwata-Gonokami, A. Loffler, S. Hofling, A. Forchel, and Y. Yamamoto. Observation of Bogoliubov excitations in exciton-polariton condensates. *Nat Phys*, 4 (9):700–705, 2008.

[27] D. Bajoni, P. Senellart, E. Wertz, I. Sagnes, A. Miard, A. Lemaître, and J. Bloch. Polariton laser using single micropillar GaAs-GaAlAs semiconductor cavities. *Physical Review Letters*, 100(4):047401–4, 2008.

[28] G. Dasbach, M. Schwab, M. Bayer, and A. Forchel. Parametric polariton scattering in microresonators with three-dimensional optical confinement. *Physical Review B*, 64(20):201309, 2001.

[29] T. K. Paraiso, D. Sarchi, G. Nardin, R. Cerna, Y. Leger, B. Pietka, M. Richard, O. El Daif, F. Morier-Genoud, V. Savona, and B. Deveaud-Pledran. Enhancement of microcavity polariton relaxation under confinement. *Physical Review B (Condensed Matter and Materials Physics)*, 79(4):045319–9, 2009.

[30] C. Leyder, M. Romanelli, J. Ph Karr, E. Giacobino, T. C. H. Liew, M. M. Glazov, A. V. Kavokin, G. Malpuech, and A. Bramati. Observation of the optical spin Hall effect. *Nat Phys*, 3(9):628–631, 2007.

[31] A. Amo, D. Sanvitto, F. P. Laussy, D. Ballarini, E. DEL Valle, M. D. Martin, A. Lemaitre, J. Bloch, D. N Krizhanovskii, M. S. Skolnick, C. Tejedor, and L. Vina. Collective fluid dynamics of a polariton condensate in a semiconductor microcavity. *Nature*, 457(7227):291–295.

[32] A. Amo, J. Lefrere, S. Pigeon, C. Adrados, C. Ciuti, R. Houdre, E. Giacobino, and A. Bramati. Superfluidity of polaritons in semiconductor microcavities. *Nat Phys*, 5:805–810, 2009.

[33] K. G. Lagoudakis, T. Ostatnicky, A. V. Kavokin, Y. G. Rubo, R. Andre, and B. Deveaud-Pledran. Observation of Half-Quantum Vortices in an Exciton-Polariton Condensate. *Science*, 326(5955):974–976, 2009.

[34] D. Sanvitto, F. M. Marchetti, M. H. Szymanska, G. Tosi, M. Baudisch, F. P. Laussy, D. N. Krizhanovskii, M. S. Skolnick, L. Marrucci, A. Lemaître, J. Bloch, C. Tejedor, and L. Viña. Persistent currents and quantized vortices in a polariton superfluid. *Nat Phys*, 6:527 – 533, 2010.

[35] P. Y. Yu and M. Cardona. Fundamentals of semiconductors: Physics and materials properties. *Springer-Verlag Berlin Heidelberg*, 1996.

[36] M. L. Cohen and J. R. Chelikowsky. Electronic structure and optical properties of semiconductors. *Springer*, 1988.

[37] S. M. Sze and K. K. Ng. Physics of Semiconductor Devices. *Wiley-Interscience*, 2006.

[38] N. Bohr. On the constitution of atoms and molecules, part I. *Philosophical Magazine*, 26:1–24, 1913.

[39] G. H. Wannier. The structure of electronic excitation levels in insulating crystals. *Phys. Rev.*, 52(3):191–197, 1937.

[40] J. Frenkel. On the transformation of light into heat in solids. II. *Phys. Rev.*, 37 (10):1276–1294, 1931.

[41] G. Bastard, E. E. Mendez, L. L. Chang, and L. Esaki. Exciton binding energy in quantum wells. *Phys. Rev. B*, 26(4):1974–1979, 1982.

[42] A. V. Kavokin, J. J. Baumberg, G. Malpuech, and F. P. Laussy. Microcavities. *Oxford University Press*, 2004.

[43] M. S. Skolnick, T. A. Fisher, and D. M. Whittaker. Strong coupling phenomena in quantum microcavity structures. *Semiconductor Science and Technology*, 13(7): 645–669, 1998.

[44] L. C. Andreani, V. Savona, P. Schwendimann, and A. Quattropani. Polaritons in high reflectivity microcavities: semiclassical and full quantum treatment of optical properties. *Superlattices and Microstructures*, 15(4):453–453, 1994.

[45] S. Pau, G. Björk, J. Jacobson, H. Cao, and Y. Yamamoto. Microcavity exciton-polariton splitting in the linear regime. *Physical Review B*, 51(20):14437, 1995.

[46] B. E. A. Saleh and M. C. Teich. Fundamentals of photonics. *Wiley-Intersience*, 1991.

[47] D. M. Whittaker, P. Kinsler, T. A. Fisher, M. S. Skolnick, A. Armitage, A. M. Afshar, M. D. Sturge, and J. S. Roberts. Motional narrowing in semiconductor microcavities. *Physical Review Letters*, 77(23):4792, 1996.

[48] V. M. Agranovich. *Soviet Physics - JETP*, 10(307), 1960.

[49] J. Keeling, P. R. Eastham, M. H. Szymanska, and P. B. Littlewood. Polariton condensation with localized excitons and propagating photons. *Physical Review Letters*, 93(22):226403, 2004.

[50] E. M. Purcell. Spontaneous emission probabilities at radio frequencies. *Phys. Rev.*, 69(11-12):674, 1946.

[51] A. V. Savona, A. C. Piermarocchi, A. A. Quattropani, and A. P. A Schwendimann. Optical properties of microcavity polaritons. *J Phase Transitions: A Multinational Journal*, 68(1):169 – 279, 1999.

[52] V. Savona, L. C. Andreani, P. Schwendimann, and A. Quattropani. Quantum well excitons in semiconductor microcavities: Unified treatment of weak and strong coupling regimes. *Solid State Communications*, 93(9):733–739, 1995.

[53] M. Müller, J. Bleuse, and R. Andrè. Dynamics of the cavity polariton in CdTe-based semiconductor microcavities: Evidence for a relaxation edge. *Physical Review B*, 62(24):16886, 2000.

[54] F. Tassone and Y. Yamamoto. Exciton-exciton scattering dynamics in a semiconductor microcavity and stimulated scattering into polaritons. *Physical Review B*, 59(16):10830, 1999.

[55] P. G. Lagoudakis, M. D. Martin, J. J. Baumberg, A. Qarry, E. Cohen, and L. N. Pfeiffer. Electron-polariton scattering in semiconductor microcavities. *Physical Review Letters*, 90(20):206401, 2003.

[56] M. Perrin, P. Senellart, A. Lemaître, and J. Bloch. Polariton relaxation in semiconductor microcavities: Efficiency of electron-polariton scattering. *Phys. Rev. B*, 72(7):075340, 2005.

[57] C. Patel, T. J. Parker, H. Jamshidi, and W. F. Sherman. Phonon frequencies in GaAs. *physica status solidi (b)*, 122(2):461–467, 1984.

[58] F. Tassone, C. Piermarocchi, V. Savona, A. Quattropani, and P. Schwendimann. Bottleneck effects in the relaxation and photoluminescence of microcavity polaritons. *Physical Review B*, 56(12):7554, 1997.

[59] C. Piermarocchi, F. Tassone, V. Savona, A. Quattropani, and P. Schwendimann. Exciton formation rates in GaAs/$Al_xGa_{1-x}As$ quantum wells. *Physical Review B*, 55(3):1333, 1997.

[60] I A Shelykh, A. V. Kavokin, Y. G. Rubo, T. C. H. Liew, and G. Malpuech. Polariton polarization-sensitive phenomena in planar semiconductor microcavities. *Semiconductor Science and Technology*, 25(1):013001, 2010.

[61] R. P. Feynman, F. L. Jr Vernon, and R. W. Hellwarth. Geometrical representation of the Schr[o-umlaut]dinger equation for solving maser problems. *Journal of Applied Physics*, 28(1):49–52, 1957.

[62] A. V. Kavokin, P. G. Lagoudakis, G. Malpuech, and J. J. Baumberg. Polarization rotation in parametric scattering of polaritons in semiconductor microcavities. *Phys. Rev. B*, 67(19):195321, 2003.

[63] K. V. Kavokin, I. A. Shelykh, A. V. Kavokin, G. Malpuech, and P. Bigenwald. Quantum theory of spin dynamics of exciton-polaritons in microcavities. *Phys. Rev. Lett.*, 92(1):017401, 2004.

[64] H.-J. Miesner, D. M. Stamper-Kurn, M. R. Andrews, D. S. Durfee, S. Inouye, and W. Ketterle. Bosonic Stimulation in the Formation of a Bose-Einstein Condensate. *Science*, 279(5353):1005–1007, 1998.

[65] L. Pitaevskii and S. Stringari. Bose-Einstein Condensation. *Clarendon Press, Oxford*, 2003.

[66] V. Savona and S. Sarchi. Bose-Einstein condensation of microcavity polaritons. *physica status solidi (b)*, 242(2290), 2005.

[67] A. Griffin, D. W. Snoke, and S. Stringari. Bose-Einstein Condensation. *Cambridge University Press*, 1995.

[68] A. J. Leggett. Bose-Einstein condensation in the alkali gases: Some fundamental concepts. *Rev. Mod. Phys.*, 73(2):307–356, 2001.

[69] N. N. Bogoliubov. On the theory of superfluidity. *J. Phys. USSR*, 11:23–32, 1947.

[70] F. Dalfovo, S. Giorgini, Lev P. Pitaevskii, and S. Stringari. Theory of Bose-Einstein condensation in trapped gases. *Rev. Mod. Phys.*, 71(3):463–512, 1999.

[71] J. M. Kosterlitz and D. J. Thouless. Long range order and metastability in two dimensional solids and superfluids. (Application of dislocation theory). *Journal of Physics C: Solid State Physics*, 5(11):L124.

[72] J. M. Kosterlitz and D. J. Thouless. Ordering, metastability and phase transitions in two-dimensional systems. *Journal of Physics C: Solid State Physics*, 6(7):1181, 1973.

[73] I. M. Khalatnikov. An Introduction to the Theory of Superfluidity. *Benjamin, New York*, 1965.

[74] W. Ketterle and N. J. van Druten. Bose-Einstein condensation of a finite number of particles trapped in one or three dimensions. *Phys. Rev. A*, 54(1):656–660, 1996.

[75] M. Richard, J. Kasprzak, R. André, R. Romestain, Le Si Dang, G. Malpuech, and A. Kavokin. Experimental evidence for nonequilibrium Bose condensation of exciton polaritons. *Physical Review B*, 72(20):201301, 2005.

[76] C. W. Lai, N. Y. Kim, S. Utsunomiya, G. Roumpos, H. Deng, M. D. Fraser, T. Byrnes, P. Recher, N. Kumada, T. Fujisawa, and Y. Yamamoto. Theory of Bose-Einstein condensation in trapped gases. *Nature*, 450(7169):529–532, 2007.

[77] D. Bajoni, P. Senellart, A. Lemaître, and J. Bloch. Photon lasing in GaAs microcavity: Similarities with a polariton condensate. *Physical Review B (Condensed Matter and Materials Physics)*, 76(20):201305–4, 2007.

[78] F. P. Laussy, G. Malpuech, A. Kavokin, and P. Bigenwald. Publisher's note: Spontaneous coherence buildup in a polariton laser [phys. rev. lett. 93, 016402 (2004)]. *Phys. Rev. Lett.*, 93(3):039902, 2004.

[79] I. A. Shelykh, Y. G. Rubo, G. Malpuech, D. D. Solnyshkov, and A. Kavokin. Polarization and propagation of polariton condensates. *Phys. Rev. Lett.*, 97(6): 066402, 2006.

[80] J. Keeling and N. G. Berloff. Spontaneous rotating vortex lattices in a pumped decaying condensate. *Phys. Rev. Lett.*, 100(25):250401, 2008.

[81] D. Read, T. C. H. Liew, Yuri G. Rubo, and A. V. Kavokin. Stochastic polarization formation in exciton-polariton Bose-Einstein condensates. *Phys. Rev. B*, 80(19): 195309, 2009.

[82] J. Kasprzak, D. D. Solnyshkov, R. André, Le Si Dang, and G. Malpuech. Formation of an exciton polariton condensate: Thermodynamic versus kinetic regimes. *Physical Review Letters*, 101(14):146404–4, 2008.

[83] J. J. Baumberg, A. V. Kavokin, S. Christopoulos, A. J. D. Grundy, R. Butte, G. Christmann, D. D. Solnyshkov, G. Malpuech, G. Baldassarri Hoger von Hogersthal, E. Feltin, J. F. Carlin, and N. Grandjean. Spontaneous polarization buildup

in a room-temperature polariton laser. *Physical Review Letters*, 101(13):136409–4, 2008.

[84] A. Kavokin, G. Malpuech, and F. P. Laussy. Polariton laser and polariton superfluidity in microcavities. *Physics Letters A*, 306(4):187 – 199, 2003.

[85] I. Carusotto and C. Ciuti. Probing microcavity polariton superfluidity through resonant Rayleigh scattering. *Phys. Rev. Lett.*, 93(16):166401, 2004.

[86] I. Carusotto, S. X. Hu, L. A. Collins, and A. Smerzi. Bogoliubov-Čerenkov radiation in a Bose-Einstein condensate flowing against an obstacle. *Phys. Rev. Lett.*, 97(26):260403, 2006.

[87] M. D. Fraser, Roumpos G., and Yamamoto Y. Vortex-antivortex pair dynamics in an excitonâĂŞpolariton condensate. *New Journal of Physics*, 11(11):113048, 2009.

[88] W. F. Vinen. The detection of single quanta of circulation in liquid helium II. *Proc. Roy. Soc., A*, 260(218), 1961.

[89] C. Ryu, M. F. Andersen, P. Cladé, V. Natarajan, K. Helmerson, and W. D. Phillips. Observation of persistent flow of a Bose-Einstein condensate in a toroidal trap. *Phys. Rev. Lett.*, 99(26):260401, 2007.

[90] S. I. Tsintzos, N. T. Pelekanos, G. Konstantinidis, Z. Hatzopoulos, and P. G. Savvidis. A GaAs polariton light-emitting diode operating near room temperature. *Nature*, 453(7193):372–375, 2008.

[91] D. Bajoni, E. Semenova, A. Lemaître, S. Bouchoule, E. Wertz, P. Senellart, and J Bloch. Polariton light-emitting diode in a GaAs-based microcavity. *Physical Review B (Condensed Matter and Materials Physics)*, 77(11):113303–4, 2008.

[92] A. A. Khalifa, A. P. D. Love, D. N. Krizhanovskii, M. S. Skolnick, and J. S. Roberts. Electroluminescence emission from polariton states in GaAs-based semiconductor microcavities. *Applied Physics Letters*, 92(6):061107–3, 2008.

[93] E. Wertz, L. Ferrier, D. D. Solnyshkov, P. Senellart, D. Bajoni, A. Miard, A. Lemaître, G. Malpuech, and J. Bloch. Spontaneous formation of a polariton condensate in a planar GaAs microcavity. *Applied Physics Letters*, 95(5):051108, 2009.

[94] J. Bloch, T. Freixanet, J. Y. Marzin, V. Thierry-Mieg, and R. Planel. Giant Rabi splitting in a microcavity containing distributed quantum wells. *Applied Physics Letters*, 73(12):1694–1696, 1998.

[95] D. Bajoni, E. Wertz, P. Senellart, A. Lemaître, S. Bouchoule, and J. Bloch. Polariton parametric luminescence in a single micropillar. *Acta Physica Polonica A*, 114(933), 2008.

[96] J. Bloch, R. Planel, V. Thierry-Mieg, J. M. Gérard, D. Barrier, J. Y. Marzin, and E. Costard. Strong-coupling regime in pillar semiconductor microcavities. *Superlattices and Microstructures*, 22(3):371–374, 1997.

[97] M. Obert, J. Renner, A. Forchel, G. Bacher, R. André, and D. Le Si Dang. Nonlinear emission in II-VI pillar microcavities: Strong versus weak coupling. *Applied Physics Letters*, 84(9):1435–1437, 2004.

[98] J. M. Gerard, D. Barrier, J. Y. Marzin, R. Kuszelewicz, L. Manin, E. Costard, V. Thierry-Mieg, and T. Rivera. Quantum boxes as active probes for photonic microstructures: The pillar microcavity case. *Applied Physics Letters*, 69(4):449–451, 1996.

[99] G. Panzarini and L. C. Andreani. Quantum theory of exciton polaritons in cylindrical semiconductor microcavities. *Physical Review B*, 60(24):16799, 1999.

[100] R. Butté, G. Delalleau, A. I. Tartakovskii, M. S. Skolnick, V. N. Astratov, J. J. Baumberg, G. Malpuech, A. Di Carlo, A. V. Kavokin, and J. S. Roberts. Transition from strong to weak coupling and the onset of lasing in semiconductor microcavities. *Physical Review B*, 65(20):205310, 2002.

[101] D. Bajoni, E. Peter, P. Senellart, J. L. Smirr, I. Sagnes, A. Lemaître, and J. Bloch. Polariton parametric luminescence in a single micropillar. *Applied Physics Letters*, 90(5):051107, 2007.

[102] M. I. Dyakonov and V. I. Perel. Current-induced spin orientation of electrons in semiconductors. *Physics Letters A*, 35(6):459–460, 1971.

[103] E. Hall. On a new action of the magnet on electric currents. *American Journal of Mathematics*, 2(3):287–292, 1879.

[104] J. E. Hirsch. Spin Hall effect. *Phys. Rev. Lett.*, 83(9):1834–1837, 1999.

[105] J. Sinova, D. Culcer, Q. Niu, N. A. Sinitsyn, T. Jungwirth, and A. H. MacDonald. Universal intrinsic spin hall effect. *Phys. Rev. Lett.*, 92(12):126603, 2004.

[106] Y. K. Kato, R. C. Myers, A. C. Gossard, and D. D. Awschalom. Observation of the spin Hall effect in semiconductors. *Science*, 306(5703):1910–1913, 2004.

[107] J. Wunderlich, B. Kaestner, J. Sinova, and T. Jungwirth. Experimental observation of the spin Hall effect in a two-dimensional spin-orbit coupled semiconductor system. *Phys. Rev. Lett.*, 94(4):047204, 2005.

[108] H. Zhao, E. J. Loren, H. M. van Driel, and A. L. Smirl. Coherence control of Hall charge and spin currents. *Phys. Rev. Lett.*, 96(24):246601, 2006.

[109] A. Amo, T. C. H. Liew, C. Adrados, E. Giacobino, A. V. Kavokin, and A. Bramati. Anisotropic optical spin Hall effect in semiconductor microcavities. *Phys. Rev. B*, 80(16):165325, 2009.

[110] T. C. H. Liew, C. Leyder, A. V. Kavokin, A. Amo, J. Lefrère, E. Giacobino, and A. Bramati. Interplay between weak localization of exciton-polaritons and the optical spin Hall effect. *Phys. Rev. B*, 79(12):125314, 2009.

[111] G. Panzarini, L. C. Andreani, A. Armitage, D. Baxter, M. S. Skolnick, V. N. Astratov, J. S. Roberts, Alexey V. Kavokin, M. R. Vladimirova, and M. A. Kaliteevski. Exciton-light coupling in single and coupled semiconductor microcavities: Polariton dispersion and polarization splitting. *Phys. Rev. B*, 59(7):5082–5089, 1999.

[112] M. Z. Maialle, E. A. de Andrada e Silva, and L. J. Sham. Exciton spin dynamics in quantum wells. *Phys. Rev. B*, 47(23):15776–15788, 1993.

[113] A.V. Kavokin, G. Malpuech, and M. Glazov. Optical spin hall effect. *Phys. Rev. Lett.*, 95(13):136601, 2005.

[114] W. Langbein, I. Shelykh, D. Solnyshkov, G. Malpuech, Yu. Rubo, and A. Kavokin. Polarization beats in ballistic propagation of exciton-polaritons in microcavities. *Phys. Rev. B*, 75(7):075323, 2007.

[115] C. Ciuti, P. Schwendimann, B. Deveaud, and A. Quattropani. Theory of the angle-resonant polariton amplifier. *Physical Review B*, 62(8):R4825, 2000.

[116] Le Si Dang, D. Heger, R. André, F. Bœuf, and R. Romestain. Stimulation of polariton photoluminescence in semiconductor microcavity. *Phys. Rev. Lett.*, 81 (18):3920–3923, 1998.

[117] M. Müller, R. André, J. Bleuse, R. Romestain, Le Si Dang, A. Huynh, J. Tignon, Ph Roussignol, and C. Delalande. Non-linear polariton dynamics in II and VI microcavities. *Semiconductor Science and Technology*, 18(10):S319–S324, 2003.

[118] J. P. Löwenau, S. Schmitt-Rink, and H. Haug. Many-body theory of optical bistability in semiconductors. *Physical Review Letters*, 49(20):1511, 1982.

[119] M. Wouters, I. Carusotto, and C. Ciuti. Spatial and spectral shape of inhomogeneous nonequilibrium exciton-polariton condensates. *Phys. Rev. B*, 77(11):115340, 2008.

[120] C. Ciuti, V. Savona, C. Piermarocchi, A. Quattropani, and P. Schwendimann. Role of the exchange of carriers in elastic exciton-exciton scattering in quantum wells. *Phys. Rev. B*, 58(12):7926–7933, 1998.

[121] D. N. Krizhanovskii, K. G. Lagoudakis, M. Wouters, B. Pietka, R. A. Bradley, K. Guda, D. M. Whittaker, M. S. Skolnick, B. Deveaud-Plédran, M. Richard, R. André, and Le Si Dang. Coexisting nonequilibrium condensates with long-range spatial coherence in semiconductor microcavities. *Phys. Rev. B*, 80(4):045317, 2009.

[122] M. Wouters and I. Carusotto. Excitations in a nonequilibrium Bose-Einstein condensate of exciton polaritons. *Phys. Rev. Lett.*, 99(14):140402, 2007.

[123] E. del Valle, D. Sanvitto, A. Amo, F. P. Laussy, R. André, C. Tejedor, and L. Viña. Dynamics of the formation and decay of coherence in a polariton condensate. *Phys. Rev. Lett.*, 103(9):096404, 2009.

[124] C. Kittel. Introduction to solid state physics. *John Wiley & Sons; 8th Edition, International Edition edition*, 2004.

[125] S. Pau, G. Björk, H. Cao, F. Tassone, R. Huang, Y. Yamamoto, and R. P. Stanley. LO-phonon-enhanced microcavity polariton emission. *Physical Review B*, 55(4): R1942, 1997.

[126] B. Hönerlage, R. Lévy, J. B. Grun, C. Klingshirn, and K. Bohnert. The dispersion of excitons, polaritons and biexcitons in direct-gap semiconductors. *Physics Reports*, 124(3):161 – 253, 1985.

[127] M. D. Martìn, D. Ballarini, A. Amo, L. Viña, and R. André. Dynamics of polaritons resonantly created at the upper polariton branch. *Superlattices and Microstructures*, 41(5-6):328–332, 2007.

[128] N. Peyghambarian, H. M. Gibbs, J. L. Jewell, A. Antonetti, A. Migus, D. Hulin, and A. Mysyrowicz. Blue shift of the exciton resonance due to exciton-exciton interactions in a multiple-quantum-well structure. *Physical Review Letters*, 53(25): 2433, 1984.

[129] S. Schmitt-Rink, C. Ell, and H. Haug. Many-body effects in the absorption, gain, and luminescence spectra of semiconductor quantum-well structures. *Physical Review B*, 33(2):1183, 1986.

[130] V. I. Yukalov, E. P. Yukalova, and V. S. Bagnato. Non-ground-state Bose-Einstein condensates of trapped atoms. *Physical Review A*, 56(6):4845, 1997.

[131] P. Renucci, T. Amand, X. Marie, P. Senellart, J. Bloch, B. Sermage, and K. V. Kavokin. Microcavity polariton spin quantum beats without a magnetic field: A manifestation of coulomb exchange in dense and polarized polariton systems. *Phys. Rev. B*, 72(7):075317, 2005.

[132] M. Vladimirova, S. Cronenberger, D. Scalbert, K. V. Kavokin, A. Miard, A. Lemaître, J. Bloch, D. Solnyshkov, G. Malpuech, and A. V. Kavokin. Polariton-polariton interaction constants in microcavities. *Phys. Rev. B*, 82(7):075301, 2010.

[133] J. Kasprzak, R. André, Le Si Dang, I. A. Shelykh, A. V. Kavokin, Yuri G. Rubo, K. V. Kavokin, and G. Malpuech. Build up and pinning of linear polarization in the Bose condensates of exciton polaritons. *Phys. Rev. B*, 75(4):045326, 2007.

[134] D. J. Griffiths. Introduction to Quantum Mechanics. *Prentice Hall*, 1994.

[135] L. I. Schiff. Quantum Mechanics. *McGraw Hill*, 1955.